Competitive Nucleation in Nanoclusters

A Thesis Submitted to the
College of Graduate Studies and Research
in Partial Fulfillment of the Requirements
for the degree of Doctor of Philosophy
in the Department of Chemistry
University of Saskatchewan
Saskatoon

By
Cletus C. Asuquo

Permission to Use

In presenting this thesis in partial fulfilment of the requirements for a Postgraduate degree from the University of Saskatchewan, I agree that the Libraries of this University may make it freely available for inspection. I further agree that permission for copying of this thesis in any manner, in whole or in part, for scholarly purposes may be granted by the professor or professors who supervised my thesis work or, in their absence, by the Head of the Department or the Dean of the College in which my thesis work was done. It is understood that any copying or publication or use of this thesis or parts thereof for financial gain shall not be allowed without my written permission. It is also understood that due recognition shall be given to me and to the University of Saskatchewan in any scholarly use which may be made of any material in my thesis.

Requests for permission to copy or to make other use of material in this thesis in whole or part should be addressed to:

Head of the Department of Chemistry
165 Thorvaldson Building
110 Science Place
University of Saskatchewan
Saskatoon, Saskatchewan
Canada
S7N 5C9

Abstract

Nucleation is the primary mechanism by which systems change phase and it plays a major role in the formation of new materials in nature and industrially. In particular, experiments and molecular dynamic simulations have shown that nanoclusters, at the same initial conditions, freeze to different structures through a competitive process. Understanding the mechanism of nucleation requires a knowledge of the reaction coordinate, which consists of a set of variables that accurately describe the formation of the critical nucleus. In classical nucleation theory (CNT), the embryo size is solely used as the reaction coordinate, but this does not capture the formation of different structures in a competitive nucleation event.

Competitive nucleation is modeled using a two dimensional Potts model undergoing heterogeneous nucleation on to a nanoscale impurity. The rates of formation of the different stable phases are calculated using transition state theory and compared with the rates obtained from the mean first passage time and survival probability methods. Transition state theory is shown to predict the rates to the different structures under various condition when the nucleation barrier is correctly normalized relative to the metastable state. A multiple paths maximum likelihood analysis, (MPMLA), is developed to extract accurate reaction coordinates to the different phases. The results show that the linear combination of size and surface area of a given component is the accurate variable that describes the transition to the phase.

Molecular dynamics simulations are used to study the competitive freezing of gold nanoclusters for a range of cluster sizes and temperatures. Measuring the probability of observing each cluster type in an ensemble of freezing events, along with the overall rate at which liquid drops freeze to any structure, allows the rate of formation for each structure to be calculated. The rate of formation of icosahedral structures is about an order of magnitude higher than the rates for other structures. Also, as the size of the cluster increased, the rate of formation of icosahedral structure decreased while that of decahedral and FCC structures increases. The MPMLA is applied to the transition path ensembles to obtain the best reaction coordinate for the different transitions. Order parameters such as size, the Steinhardt bond orientational parameters, local order parameters such as Q_e, ratio of local atom type in the largest embryo, and structural order parameters are tested as reaction coordinates. A linear combination of

size, the $fcc - fcc$ correlation parameter, and the Q_e provided the maximum estimate for the liquid-icosahedral transition, making it the best reaction coordinate. The critical embryo for this transition consists of bulk fcc-type atoms arranged in a small group, and capped by surface 111 atoms to form a tetrahedron. There is at least one 5-fold symmetric cap for this critical embryo. For the liquid-decahedral transition, the linear combination of size, Q_e and the $Ih_{edge} - < 111 >$ correlation parameter is the best reaction coordinate. Analysis of the critical embryo shows the formation of blocks of bulk fcc atoms. The number of fcc-type atoms in these blocks is greater than those observed in the case of the icosahedral transition, hence, the Q_e parameter has a stronger effect. There is also the presence of $< 111 >$ and the Ih_{edge} atoms positioned to form the 5-fold cap. The formation of the FCC structures follows the growth of the bulk fcc atoms with a corresponding elimination of the 5-fold facets. Hence, the linear combination of Q_e, the $Ih - Hcp$ and $Ih_{edge} - < 111 >$ correlation parameters, is the best reaction coordinate that describes the formation of FCC clusters.

Acknowledgements

First and foremost, I give thanks to God for His grace upon my life; for being the author and finisher of all I am and hope to become.

I would like to express my sincere gratitude to Prof. Richard K. Bowles for being my supervisor and more so, my mentor and teacher through the course of my graduate studies. It is through his support and constant encouragement that made this thesis a reality.

Special thanks to members of my academic advisory committee, Prof. Ian Burgess, Prof. Matthew Paige and Prof. Aaron Phoenix, for their support, guidance and suggestions.

I am thankful to the Department of Chemistry of the University of Saskatchewan, for giving me an opportunity to study and do research at this great institution. I also thank Akwa Ibom state government of Nigeria, for my initial scholarship through the Akwa Ibom State University staff training programme.

I am grateful to my wonderful wife, Caroline, for her continued love, patience and support; my son, Inibehe, for arriving just on time to make the completion of this thesis more fun. The laughter you give me everyday gives me joy to carry through this work. To my mom, there is no words to describe how grateful I am to have the love and support you have provided me through my academic endeavors. The foundation you laid, and encouragement have led me this far. To my brother, Bruno, thank you for being there for me always. To my sisters, thank you for all the love and supports.

To all my friends, please do not take this lightly, but I really appreciate all that you do for me and I say thank you for being a part of my life. Finally, I would like to thank past and present members of Richard Bowles' research group; Aswin, Eduardo, Levent, Nalantha, Mahdi, Weikai, Danielle, Sheida and Ebenezer, for fruitful discussions.

This thesis is dedicated to the memory of my late dad, Christopher Asuquo, who passed on while expecting the completion and a layman interpretation of this work.

Contents

Permission to Use i

Abstract ii

Acknowledgements iv

Contents vi

List of Tables vii

List of Figures viii

List of Abbreviations ix

List of Symbols x

1 Introduction 1
- 1.1 Nucleation in Phase Transitions . . . 3
- 1.2 Competitive Nucleation and Polymorphism in Materials . . . 11
- 1.3 Transition Path Sampling . . . 14
  - 1.3.1 Aimless Shooting Method . . . 16
- 1.4 Maximum Likelihood Analysis . . . 18
- 1.5 Scope of the Thesis . . . 21

2 Competitive Rates of Heterogeneous Nucleation in a Potts Model 23
- 2.1 Introduction . . . 23
- 2.2 Model and Methods . . . 25
  - 2.2.1 Model . . . 25
  - 2.2.2 The Nucleation Free Energy Surface . . . 26
  - 2.2.3 Competitive Rates of Nucleation . . . 29
- 2.3 Results . . . 34
  - 2.3.1 Free Energy Surfaces . . . 34
  - 2.3.2 Transition State Theory . . . 40
  - 2.3.3 Survival Probability . . . 42
  - 2.3.4 Mean First Passage Time . . . 44
- 2.4 Discussions . . . 46
- 2.5 Conclusions . . . 48

3 Reaction Coordinates for Competitive Phase Transition 50
- 3.1 Introduction . . . 50
- 3.2 Theoretical Overview . . . 51
  - 3.2.1 Transition Path Sampling . . . 51
  - 3.2.2 Multiple States Transition Path Sampling . . . 51
  - 3.2.3 Multiple Paths Maximum Likelihood Analysis . . . 53
- 3.3 Simulation Details . . . 55

3.3.1 Aimless Shooting . . . 55
3.4 Results and Discussions . . . 57
3.5 Conclusions . . . 69

4 Competitive Rates of Freezing in Gold Nanoclusters 71
4.1 Introduction . . . 71
4.2 Simulation Methods . . . 72
4.2.1 Simulation Details . . . 72
4.2.2 Structural Analysis . . . 73
4.3 Results and Discussions . . . 77
4.3.1 Structural Identifications . . . 77
4.4 Nucleation Rates . . . 85
4.5 Conclusions . . . 90

5 Effective Reaction Coordinates in the Nucleation of Gold Nanoclusters 91
5.1 Introduction . . . 91
5.2 Simulation Details . . . 92
5.2.1 Aimless Shooting . . . 92
5.2.2 Structural Basin Identification . . . 93
5.2.3 Test Order Parameters . . . 96
5.3 Results and Discussions . . . 100
5.3.1 Icosahedral Structure . . . 105
5.3.2 Decahedral Structure . . . 113
5.3.3 FCC Structure . . . 118
5.3.4 Icosahedral - Decahedral Transition . . . 120
5.3.5 Discussion . . . 121
5.4 Conclusions . . . 124

6 Discussions and Conclusions 125
6.1 Discussions . . . 125
6.2 Conclusions . . . 130

References 132

List of Tables

2.1 Summary of conditions and parameters used to calculate the free energy surfaces and the rates. The free energy surfaces were calculated for cases **1-3**. 29
2.2 Summary of critical sizes and free energy barriers for different conditions at which the simulation was performed. 35
2.3 Summary of the different factors and free energy barriers used to calculate the rates for the different conditions. 40
2.4 The probabilities of seeing different phases, the overall rates obtained from the slopes in fig. 2.11 and the individual rates for the different conditions. 44
2.5 Fit parameters from fitting eq. 2.3.4, the overall nucleation rates and the individual rates for the different conditions using the MFPT method. 46

3.1 Different order parameters tested for $A \rightarrow B$ transitions in the Potts model with equal fields. $BIC = (1/2)\ln N_R = 4.36$ 63
3.2 Different order parameters tested for $A \rightarrow C$ transitions in the Potts model. $BIC = (1/2)\ln N_R = 4.65$ 64
3.3 Different order parameters tested for $A \rightarrow B$ transitions in the Potts model with unequal fields. $BIC = (1/2)\ln N_R = 4.36$ 65
3.4 Different order parameters tested for $A \rightarrow C$ transitions in the Potts model with unequal fields. $BIC = (1/2)\ln N_R = 4.65$ 66
3.5 Different order parameters tested for $A \rightarrow B$ transitions in the Potts model with $H_C = 0.17, H_B = 0.12$ and 20% mixing. $BIC = (1/2)\ln N_R = 4.36$ 66
3.6 Different order parameters tested for $A \rightarrow C$ transitions in the Potts model with $H_C = 0.17, H_B = 0.12$ and 20% mixing. $BIC = (1/2)\ln N_R = 4.36$ 67

5.1 Mean values of Steinhardt order parameters and semi-principal axes used to identify the product basins. 94
5.2 Mean values of order parameters from CNA and their corresponding semi-principal axes used to identify the product basins. 96
5.3 Average bond order parameters for liquid, Ih and FCC structures. 99
5.4 Test order parameters and their performance as reaction coordinate for liquid→solid transition in gold nanoclusters. $BIC = (1/2)lnN_R = 5.499$. 101
5.5 Different single order parameters tested for liquid→Ih transitions in gold nanocluster. $BIC = (1/2)\ln N_R = 4.942$ 107
5.6 Different single order parameters tested for $liquid \rightarrow Ih$ transitions in gold nanocluster. $BIC = (1/2)lnN_R = 4.942$ 110
5.7 Different single order parameters tested for $liquid \rightarrow Dh$ transitions in gold nanoclusters. $BIC = (1/2)\ln N_R = 3.837$ 114
5.8 Linear combination of order parameters tested for liquid→Dh transitions in gold nanoclusters. $BIC = (1/2)\ln N_R = 3.837$ 116
5.9 Different single order parameters tested for $liq \rightarrow FCC$ transitions in gold nanoclusters. $BIC = (1/2)\ln N_R = 3.858$ 119
5.10 Coefficients of the different order parameters for the different structures formed from the metastable liquid. 123

List of Figures

1.1 A diagram showing the different surface and volume contributions to the Gibbs free energy. σ is the surface energy per unit area, while $\Delta\mu$ is the differences in chemical poetical between the metastable and stable phases. 4
1.2 A diagram showing TPS with regions **A** and **B** in phase space corresponding to locally stable phases. 15
1.3 A diagram showing the generation of a new transition pathway from an old transition path in an Aimless shooting method. 16
1.4 The $p(TP|r)$ and p_B functions for a system with diffusive barrier crossing. . . 19

2.1 Transition graphs depicting Ising and Potts models. 24
2.2 Example of configuration of Potts model with $\mathbf{J}_{B,C} = -1.0$, $H_B = H_C = 0.12$. The light grey and dark grey lattices are the stable phases, the black lattices represent the impurity. The white background represents the metastable phase. 27
2.3 Plots of the size of component B in the largest cluster as a function of time (mcs) for twenty different trajectories. The dashed line $n_B = 150$ or $n_C = 150$ is used to determine the nucleation time. The trajectories with small sizes of component B have high C component where such trajectories stop. 33
2.4 Free energy surface, $\Delta G(n_B, n_C)$ for nucleation of phases B and C from a metastable phase on an heterogeneity of length $l = 7$ for the case where $\beta H_B = \beta H_C = 0.12$. The region below the red dots indicates the metastable region. . 36
2.5 Free energy surface, $\Delta G(n_B, n_C)$ for nucleation of phases B and C from a metastable phase on an heterogeneity of length $l = 7$ for *case* **2** where $\beta H_B = 0.12$ and $\beta H_C = 0.17$. The region below the red dots indicates the metastable region. 37
2.6 Free energy surface, $\Delta G(n_B, n_C)$ for nucleation of phases B and C from a metastable phase on an heterogeneity of length $l = 7$ for *case* **3** where $\beta H_B = 0.12$ and $\beta H_C = 0.17$ and $J_{B,C} = -0.8$. The region below the red dots indicates the metastable region. 38
2.7 Probabilities of N-sized cluster on the heterogeneity for Potts model with $q = 3$ and $q = 2$ (Ising model). For the case when $q = 3$, $N = n_B + n_C$. 39
2.8 The fluctuation of size, $< \Delta n_B^2(t) >$, for component **B** as a function of time. . 41
2.9 Plots of ΔG_B^* at $n_C = 5, 6, 7$ and the quadratic fits to them, which are used to obtain the curvature of the free energy surface, η_B. 41
2.10 Plots of the rates $J_{B_{TST}}$ and $J_{C_{TST}}$ compared to the overall rates, J_{TST}, at conditions defined for the free energy calculations. 42
2.11 Plots of $ln\ R(t)$ versus MC steps with the slope representing $-JV$ for different cases listed in Table 3.1 showing the linear fits to the simulation data. 43
2.12 Plots of the rates $J_{B_{SP}}$ and $J_{C_{SP}}$ compared to the overall rates at conditions defined for the free energy calculations. 44
2.13 MFPT from simulations for the different cases studied. 45
2.14 Comparison of the rates of exiting the metastable phase, $J_{TST}, J_{SP}, J_{MFPT}$ for different conditions. 47

3.1 Schematic diagram showing possible transitions. (a) Transition only from the metastable phase to the phases B and C. (b) Possible transition between phases B and C in addition to $A \rightarrow B$ and $A \rightarrow C$ transitions. 52
3.2 Plot of transition path probabilities as a function the reaction coordinate, r. 54
3.3 Free energy surface, $\Delta G(n_B, n_C)$, for nucleation of phases B and C showing the initial shooting points for the aimless shooting. 56
3.4 The committor probabilities, $p_A(n_B), p_B(n_B)$ and $p_C(n_B)$ as a function of the size of component B at equal fields($i.e\ H_B = H_C = 0.12$). 58
3.5 The committor probabilities, $p_A(n_B)$,$p_B(n_B)$ and $p_C(n_B)$ unequal fields($i.e\ H_B = 0.12, H_C = 0.17$). 59
3.6 The committor probabilities, $p_B(n_B)$ and $p_C(n_C)$ unequal fields($i.e\ H_B = 0.12, H_C = 0.17$) and $J_{B,C} = -0.8$. 60
3.7 Free energy surface, $\Delta G(n_B, n_C)$, for nucleation of phases B and C when mixing is allowed, showing the initial shooting points deviating away from basins B and C 60
3.8 Free energy surface, $\Delta G(n_B, n_C)$ for nucleation of phases B and C from a metastable phase on an heterogeneity of length $l = 7$. 62
3.9 Shooting points showing the collective variables (q_{s_B}, q_{n_B}) for the $A \rightarrow B$ TPE. The red line shows the critical condition, while the green line is a least squares fit , $q_{s_B} = 1.50 q_{n_B}$. 64
3.10 Comparison of the critical sizes obtained from free energy surfaces and those from the MPMLA for the different cases. 68
3.11 A committor probability distributions for two reaction coordinates obtained from the maximum likelihood analysis. 70

4.1 The energy of the cluster per atom as a function of simulation time for six trajectories ($N = 561$). The red solid line, $U = -3.63eV$, identifies the energy used to determine when a cluster has nucleated. 74
4.2 A diagram showing how surface and bulk atoms are identified using the cone having azimuthal angle, θ_c, and side length, l_c. The upper cone identifies a surface atom while the lower cone shows a bulk atom. 75
4.3 Diagrams showing how the classification of local structures defined in CNA are constructed. Reproduced with permission from ref. [135] 77
4.4 Different structural types observed for the $N = 923$ cluster. For the structures shown, red indicates amorphous, pink indicates bulk *Ih*, blue indicates surface *Ih*-edge, purple indicates surface *Ih*-vertex, brown indicates bulk *Hcp* and green indicates bulk *fcc*. The remaining atoms are represented as points for clarity . 78
4.5 The fraction of surface (top) or bulk (bottom) atoms of a given CNA type as a function of temperature for liquid particles. Fraction of amorphous atoms not shown. 80
4.6 $N_{b(Ih)}$ as a function of Q_6 for the initial liquid configuration (triangles) and the final configurations (circles) of the $N = 561$ clusters. 81
4.7 $N_{b(Ih)}$ as a function of Q_6 for the final configurations of the $N = 923$ clusters. 82
4.8 Q_s as a function of Q_b for the initial liquid configuration (triangles) and the final configurations (circles) of the $N = 561$ clusters. 83
4.9 Q_s as a function of Q_b for final configurations of the $N = 923$ clusters. 84
4.10 T versus P_{Ih} for cluster sizes $N = 309 - 923$ 86

4.11 T versus P_i for i=Dh (top) and i=FCC (bottom) for cluster sizes $N = 309 - 923$ 87
4.12 Determination of nulceation rate, J, from $R(t_n)$ for $N = 923$ at three different temperatures. 88
4.13 (Left) J/N as a function of T for different cluster sizes. (Right) J_i/N, for $i = Ih, Dh, Dh_2, Th, FCC$ as a function of N at $T = 700$K. 89

5.1 A diagram showing cluster size,n, along different trajectories used in picking initial shooting points. The arrows point to points where the initial shooting configurations were picked from. 93
5.2 Identification of the different structural basins with ellipsoids constructed using data from Table 5.1. Red ellipsoid represent the metastable liquid, light green is for Ih, blue is for Dh while pink and cyan are for Dh_2 and FCC, respectively. The points are the end configurations from different freezing trajectories. . . 95
5.3 A diagram showing how $S(i)$ is constructed using the local environment of the nearest neighbors of particle i. All the atoms within the orange circle are the nearest neighbors. All the green atoms have the same local environment as identified using CNA, while the red atoms are in a different environment from the green ones. 100
5.4 Aimless shooting data for liquid → solid transitions compared to (a) $P_{sol}(r(n))$ and (a) $P(TP|r(n))$. 102
5.5 Aimless shooting data for liquid → solid transitions compared to (a) $P_{sol}(r)$ and (b) $P(TP|r)$, where $r = n \times Q_e$ 103
5.6 Committor probability distributions for two reaction coordinates obtained from the maximum likelihood analysis. 104
5.7 The transition path probabilities for (a) liquid - solid and (b) solid-solid transitions. In the plots, A=Liquid, B=Icosahedral,C=Decahedral,D=Off-centered Decahedral, E=FCC. 106
5.8 The committor probabilities to the different phases as a function (a) Q_e, (b) $\hat{S}_{fcc-fcc}$. 106
5.9 The transition path probabilities for $liquid \rightarrow Ih$ transition as a function of (a) $\hat{S}_{fcc-fcc}$, (b) $\hat{S}_{Ih}$ and S_{Ih-hcp}, with their respective models 108
5.10 A Plot showing $\hat{S}_{Ih-hcp}$, $\hat{S}_{fcc-fcc}$ and $\hat{S}_{edge-<111>}$ for Ih trajectory. 109
5.11 Shooting points that lie on the $liquid \rightarrow Ih$ transition path plotted with $n, \hat{S}_{fcc-fcc}$ and Q_e. The red points are points for a typical trajectory leading to Ih structure. 111
5.12 Shooting points that lie on the $liquid \rightarrow Ih$ transition path projected into order parameters, n and $\hat{S}_{fcc-fcc}$. The purple and pink lines are critical lines for $Q_e = 0.18$ and $Q_e = 0.31$ 111
5.13 A 2D visualization of a configuration on the transition state leading to the icosahedral structure.(a)The black circles enclosed within the green boxes are the bulk Fcc atoms arranged to form tetrahedra structures. (b) The black triangles enclosed within magenta boxes are the surface $< 111 >$ facets while the red squares within the blue circles are the atoms forming the five fold cap. 112
5.14 A p_{Ih} distribution histogram for the critical condition, $\hat{S}^*_{fcc-fcc} = 13.0617 - 0.03893n - 13.9735Q_e$. 113
5.15 A Plot showing $\hat{S}_{Ih-hcp}$, $\hat{S}_{fcc-fcc}$ and $\hat{S}_{edge-<111>}$ for Dh trajectory. 115

5.16 Shooting points that on the *liquid* $\rightarrow$ *Dh* transition path plotted with order parameters making the reaction coordinate (n, Q_e and $\hat{S}_{edge-<111>}$). The red points are on a typical trajectory leading to *Dh* structure. 117
5.17 Shooting points that are on the *liq* $\rightarrow$ *Dh* transition path projected into order parameters, n and Q_e. 118
5.18 A 2D visualization of the critical embryo leading to the *Dh* structure. Black circles with green boxes are the bulk *fcc* atoms, black triangles within magenta boxes are the surface $< 111 >$, while red squares in blue dashed circle indicate the five-fold cap. 119
5.19 Plot of the transition path probabilities for Liq $\rightarrow$ *FCC* transition as a function of $\hat{S}_{fcc}$ and $\hat{S}_{Ih-hcp}$. 120
5.20 A p_{FCC} distribution histogram for the critical condition, $Q_e^* = 0.2866+0.0358\hat{S}_{Ih-hcp}+ 0.0584013\hat{S}_{edge-<111>}$. 121
5.21 Shooting points that on the *Ih* $\rightarrow$ *Dh* transition path projected into order parameters, n and Q_e, showing trajectories ending in *Ih* and *Dh* 122
5.22 A 2D visualization of the critical embryo leading to the decahedral structure from the icosahedral structure. Black circles within green boxes show the position of the bulk *fcc* atom. 122

List of Abbreviations

CNT	Classical Nucleation Theory
TPS	Transition Path Sampling
TPE	Transition Path Ensemble
TIS	Transition Interface Sampling
MD	Molecular Dynamics
MC	Monte Carlo
MLA	Maximum Likelihood Analysis
DNT	Dynamic Nucleation Theory
EMLD	Extended Modified Liquid Drop
MPTPS	Multiple Paths Transition Path Sampling
MPMLA	Multiple Paths Maximum Likelihood Analysis
FCC	Face Centered Cubic
HCP	Hexagonal Closed Pack
MFPT	Mean First Passage Time
TST	Transition State Theory
BIC	Bayesian Information Criterion
CNA	Common Neighbor Analysis

List of Symbols

Q_l	Bond orientational order
Ih	Icosahedral
Dh	Decahedral
$t-Dh$	Truncated decahedral
ΔG^*	Height of free energy barrier
$\Delta\mu$	Change in chemical potential
σ	Surface energy per unit area
Q_e	Bond orientational order of the embryo
n^*	Critical embryo size
J	Rate of nucleation
k_B	Boltzmann's constant
$f(n,t)$	Number density of n-sized embryo at time, t
f_{eq}	Equilibrium embryo size distribution
$P_{AB}(TP\|r)$	Transition path probability on AB transition
h_i	Characteristic function defining phase i
Δ_t	Time step
$q_A(\mathbf{x})$	Test order parameter for configuration $\mathbf{x}$
p_BS	Committor probability to phase B
$\mathbf{V}_{t0}$	Initial velocities
$L(\alpha)$	Likelihood function
N_R	Number of realizations in the likelihood function
E	Energy of the system
H_{α_i}	External field strength
$\mathbf{J}_{\alpha_i,\alpha_j}$	Interaction parameter
M_{α_i}	Magnetization
l	Length of impurity spins
Z	Partition function
Z_m	Partition function of the metastable region
f^+	Rate of attachment to the critical embryo
n_B	Size of component B in the largest embryo
n_C	Size of component C in the largest embryo
U_B	Biasing potential
κ_B, κ_C	Umbrella constants
n_{0B}, n_{0C}	Umbrella centers
$\Delta n_B, \Delta n_C$	Fluctuation of size components
z_B, z_C	Zeldovich factors
η	Curvature of the free energy barrier
N_T	Total number of trajectories
N_B	Number of trajectories ending in phase B
N_C	Number of trajectories ending in phase C
k_b, k_c	Rate constants
τ	Nucleation time
P_i	Probability of a given phase i

J_i	Rate of nucleation for a given phase i
$R(t)$	Ratio of unnucleated trajectories at a given time
J_{TST}	Overall rate of nucleation from transition state theory
J_{SP}	Overall rate of nucleation from survival probability
J_{MFPT}	Overall rate of nucleation from mean first passage time
L_{ij}	Likelihood function for $i \rightarrow j$ transition
LE_{max}	Maximum likelihood estimate
$r(\mathbf{q})$	Reaction coordinate as a function of a set of order parameters
r^*	Critical value of the reaction coordinate
χ_i	Mole fraction for component i
N	Total number of atoms in a cluster
$q_{lm}(i)$	Bond orientational order for atom i
θ_c	Azimuthal angle
l_c	Side length of a cone
Q_s	Bond orientational order for all surface atoms
Q_b	Bond orientational order for all bulk atoms
fcc	Atom in a face centered cubic local environment
$N_{b(Ih)}$	Number of bulk icosahedral atoms
Th	Tetrahedral stucture
Dh_2	Off centered decahedral
S_{a-b}	Structural correlational order between local environments a and b

Chapter 1

Introduction

Nucleation is a major step in the formation of new materials, both in nature and industrially, and, nucleation in nanosystems is gaining enormous attention due to the scientific and technological potentials of nano-sized materials. Despite its importance, a molecular level understanding of nucleation is still lacking. In particular, molecular dynamic simulations have shown that nanoclusters at the same initial conditions freeze to different structures through a competitive process[1, 2, 3]. Understanding the dynamics of competitive nucleation is essential in the production of materials whose desired properties are structure dependent, and in the understanding of certain disease conditions caused by misfolded proteins[4]. The knowledge of these dynamics would aid the controlled formation of different materials with considerable technical and financial implications especially in areas such as pharmaceuticals[5], genetic diseases and energy storage[6], where crystalline structures can play significant roles. The probabilities of having a given structure and its rates of formation are said to be determined by the nucleation barrier and the growth kinetics[3, 7].

The rate of any nucleation event is dramatically increased by the presence of a heterogeneous surface due to the lowering of the free energy barrier to processes such as vapor condensation and crystallization[8]. Hence, heterogeneous nucleation is more abundant in nature than homogeneous nucleation and is responsible for important atmospheric physics[9] as well as protein crystallization[10].

Understanding the mechanism of nucleation requires a knowledge of the reaction coordinate, which consists of a reduced set of variables describing the formation of the critical nucleus. In many processes, the reaction coordinates are difficult to obtain and sometimes involve several quantities that are not easily defined. In classical nucleation theory (CNT), the embryo size is solely used as the reaction coordinate. Though size is an important variable in nucleation [8], it contains little information about the embryo geometry and the

role of variables such as embryo surface area and structural internal order, which maybe important, are not well accounted for [11, 12]. To understand the effects of surface areas and structural order, the different structures should be rigorously identified. To do this, many approaches have been suggested. Polak and Partykiejew [13] used a combination of visual inspection, the structural order parameter, Q_l, introduced by Steinhardt [14] and the method of Voronoi polyhedra to observe the structural distribution of face-centered cubic, (FCC), hexagonal close packed, (HCP), icosahedral, (Ih) and truncated decahedral, $(t-Dh)$ structures has been used to study Lennard-Jones clusters as a function of temperature. The authors pointed out that their structures may not be a true representation of the equilibrium distribution of these motifs since the global stability of these structures could not be guaranteed based on their method. Wang *et al.* [15] used a series of linear combinations of Q_l's (where $l = 4, 6, 8$) to identify the local structures within the atomic clusters of different sizes. The structural unit which they considered is the first coordination shell around an atom and studies show that for Lennard-Jones and C_{60} clusters, the FCC, HCP Ih and Dh motifs provide a complete set of coordination number, which is 12 for these geometries. The geometries of the Lennard-Jonnes clusters show a marked dependence on the cluster size based on the number of complete shells of the Mackay Ih or Marks Dh. However, these studies focused on identifying the nature of the global structure of the cluster, rather than identifying the structure of the nucleation embryo.

Recently, there have been efforts to understand the role of structure and surface area in the nucleation of new phases from the metastable liquid using the transition path sampling method (TPS) [11, 12, 16, 17]. In TPS, the configurations obtained along the transition path are subjected to a maximum likelihood analyses [12, 18] or genetic neural network analyses [19], in order to identify the most accurate order parameter, or their combination, that represents the reaction coordinate. Lechner *et al.* [20] harvested a reweighted path ensemble from a 2D z-potential, which they analyzed using the maximum likelihood analysis and string method to show that reaction coordinates can be non-linear. For the homogeneous nucleation of nanoparticles, a combination of the embryo size and its structural order has been shown to explain the nature of the critical nuclei [16, 17]. Using the Ising model to study homogeneous nucleation in liquids [11, 12], a combination of size and the surface area of the embryo provided the most accurate reaction coordinate.

Molecular dynamic simulations of freezing in nanoparticles show that under the same conditions, clusters will freeze to different structures[1, 2, 3]. This suggests that different structural parameters are needed to describe the transformation for the different structures. Rogal *et al.* [21] used transition interface sampling (TIS), a variant of TPS, to sample a complex system which exhibits intermediate stable states. They also used the transition path probability to calculate the rates to the different intermediates and to the final product.

The central theme of this thesis is to develop a molecular level understanding of competitive nucleation processes, with a particular interest in studying the freezing of gold nanoparticles. Its content is organized as follows: In Chapter 1, I will introduce and review the concept of competitive nucleation as a precursor for polymorphism in natural and industrial materials. The chapter starts with a general overview of nucleation with particular interest in models used to understand nucleation events. Section 1.2 reviews competitions in phase transitions, while Section 1.3 introduces aimless shooting, a method of transition path sampling used in this work. The maximum likelihood analysis, as it applies to obtaining reaction coordinates, is reviewed in Section 1.4. Finally, the scope of this thesis will be defined in Section 1.5. Chapter 2 examines the dynamics of competitive nucleation between different phases forming on a nanoscale heterogeneity using Potts model. In Chapter 3, the aimless shooting method of transition path sampling is extended to the study of competitive nucleation, where multiple transitions may occur. The multiple path maximum likelihood expression is developed and applied to competitive nucleation in Potts model. Molecular dynamics simulations are used to study rates of competitive nucleation phenomenon in gold nanoclusters of various sizes and at different temperatures in Chapter 4, while in Chapter 5 the multiple path maximum likelihood analysis is applied to competitive nucleation in gold nanocluster of size $N = 561$. In Chapter 6, the summary of the important findings in this thesis and their implications are presented.

1.1 Nucleation in Phase Transitions

Phase transitions occur everywhere in nature. Common examples are the condensation of water vapor into droplets forming rain, the formation of bubbles in the boiling of a liquid, or the crystallization of water during freezing. These three transitions, which have lots of practical interests, constitute a fundamental problem in many scientific areas. Any liquid

can be held at about 10 °C below its freezing temperature without freezing. Also, a gas sample can be compressed to several times its equilibrium condensation pressure before liquid droplets spontaneously appear. The supercooled liquid and the supersaturated gas are said to be metastable. This means they are stable to local fluctuations. Small fluctuations of the metastable phase always disappear while large fluctuations will grow to a new stable phase. The fundamental mechanism that describes the kinetic transformation of a metastable phase into a more stable phase is termed nucleation. During a fluctuation, the movement of materials into the more stable phase lowers the free energy of the system, but the creation of the new stable phase introduces an interface at a free energy cost. The competition between these volume and surface terms give rise to a free energy barrier. Fig. 1.1 shows the contributions of the surface and volume terms to the Gibbs free energy as a function of droplet size. ΔG^* is the height of the energy barrier, n^* is the critical size beyond which the embryo grows spontaneously.

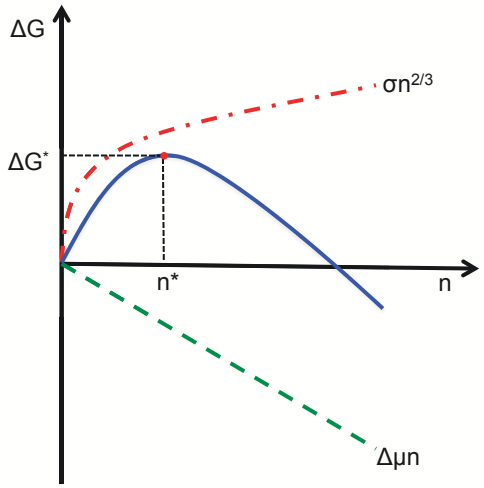

Figure 1.1: A diagram showing the different surface and volume contributions to the Gibbs free energy. σ is the surface energy per unit area, while $\Delta\mu$ is the differences in chemical poetical between the metastable and stable phases.

There are two main types of nucleation; homogeneous and heterogeneous nucleation. Homogeneous nucleation occurs in the bulk of a pure substance, while heterogenous nucleation takes place in the presence of impurities, surfaces, boundaries or pre-existing particles. The impurities, surfaces, boundaries and pre-existing particles provide preferential sites where the new stable phase is formed. Such preferential sites reduce the amount of new interface

that needs to be formed between the stable phase and the metastable phase, thereby reducing the resultant free energy barrier. Hence, heterogeneous nucleation is more common in nature than homogeneous nucleation, since the rate of any nucleation event is exponentially dependent on the free energy barrier.

Nucleation occurs in many forms. Condensation, crystallization, and cavitation in simple systems are all examples of phase transitions that start with nucleation. Condensation is the formation of liquid droplets from a supersaturated vapor caused by fluctuations in density. The nucleation of water droplets or ice crystals in the atmosphere is a major process in the water cycle and understanding this process constitutes one of the fundamentals of weather forecasting. Precipitation such as rain or snow can be forced to occur by inducing nucleation in the atmosphere and the formation of clouds in the presence of aerosols is one of the causes of global warming [22].

Crystallization, which is the formation of solid crystals from either a supersaturated homogeneous solution or a supercooled liquid, has many industrial and biological applications. The properties of advanced industrial materials such as polymers, ceramics and semi-conductors are controlled during crystallization. In the pharmaceutical industry, the appropriate choice of crystal structure of drugs, which is controlled at the nucleation stage, determines their delivery, bio-availability and effectiveness [23]. Avoiding or controlling ice nucleation is desirable in the area of cryogenics for the preservation of embryos and human tissue [24]. Water expands when it freezes, as such the preserved tissues can be damaged if ice is not avoided. The functionality of protein molecules is dependent on their structure. During protein folding, the shape or structure of the critical nucleus influences the formation of the secondary and tertiary structure of the protein and hence its functionality. Protein crystallization or aggregation is thought to be a major cause of certain health conditions or diseases such as sickle cell anemia,a cataract in the eye, and the formation of kidney stones(uric acid crystals) [25].

Several experiments [26, 27, 28, 29, 30, 31] and computational [32, 33, 1, 2] studies have aimed at the understanding of the nucleation phenomenon. The major theory used to explain nucleation is *Classical Nucleation Theory* (CNT). This theory has been developed by the independent contributions of Volmer and Weber [34], Becker and Doring [35], and Frenkel [36], among others. CNT is aimed at describing the evolution of the population of clusters of the new phase. Kinetically, the appearance of an embryo in a new phase can be described as

the addition of two monomers to form a dimer[8]. Continuous addition to and removal from this dimer results in fluctuations as the addition and removal of atoms causes the growth and shrinkage of the embryo, respectively. Therefore, the description of the change in the population of an embryo of a given size, n, at time, t may be written as

$$\frac{\partial f(n,t)}{\partial t} = \beta_{n-1} f(n-1,t) + \alpha_{n+1} f(n+1,t) - \beta_n f(n,t) - \alpha_n f(n,t), \tag{1.1}$$

where $f(n,t)$ is the number density of embryos having n-monomers at time t, while β_n and α_n are the rates at which $n - sized$ embryo gains or loses monomers respectively. This can be rewritten as

$$\frac{\partial f(n,t)}{\partial t} = J(n+1,t) - J(n,t), \tag{1.2}$$

where

$$J(n,t) = \beta_n f(n,t) - \alpha_{n+1} f(n+1,t), \tag{1.3}$$

represents the resultant rate at which embryos of size n become embryos of size $n+1$ at time t. The value of the constant β_n for the attachment of a monomer is often obtained through kinetic theory of gases, but the value of the rate constant for the detachment, α_n, is not easily obtained independently. By using the *constrained equilibrium hypothesis*, which states that the embryos evolving from the metastable phase cannot grow beyond a certain limiting size, and assuming microscopic reversibility at equilibrium, the net rate must be zero and hence independent of it, eqn. 1.3 now becomes

$$J(n) = \beta_n f_{eq}(n) - \alpha_{n+1} f_{eq}(n+1) = 0, \tag{1.4}$$

where the equilibrium distribution of $n - sized$ embryos, $f_{eq}(n)$, has replaced the non-equilibrium distribution. Solving for α_{n+1} in eqn. 1.4 gives

$$\alpha_{n+1} = \frac{f_{eq}(n)\beta_n}{f_{eq}(n+1)}. \tag{1.5}$$

Putting this back in eqn. 1.3 yields

$$J(n) = \beta_n f_{eq}(n) \left[\frac{f(n,t)}{f_{eq}(n)} - \frac{f(n+1,t)}{f_{eq}(n+1)} \right]. \tag{1.6}$$

CNT assumes steady state conditions, where the distribution of clusters of different sizes is independent of time. This results in $\partial f(n,t)/\partial t = 0$, and the flux is not dependent on the

cluster size, $i.e, J(n) = J$. Performing a recurrent summation over all embryo sizes present, the total steady state nucleation rate is

$$J = N_{tot} \left[\sum_{n_{min}}^{n_{max}} \frac{1}{\beta_n f_{eq}(n)} \right]^{-1}, \tag{1.7}$$

where N_{tot} is the total number density of embryos and the limits of the sum are taken from the smallest embryo size, n_{min} to the the largest embryo in the cluster, n_{max}, and are such that for $n \geq n_{min}$, $f(n) = f_{eq}(n)$ and for $n > n_{max}$, $f(n) = 0$. The equilibrium embryo size distribution, $f_{eq}(n)$, is obtained directly from the theory of thermodynamic fluctuation[8],

$$f_{eq}(n) = f_{eq}(0) \exp\left(\frac{-\Delta G(n)}{k_B T} \right), \tag{1.8}$$

where $G(n)$ is the free energy required to form an $n - sized$ embryo from monomers, k_B is the Boltzmann constant and T is the temperature. Replacing the summation in eqn. 1.7 by an integral and using eqn. 1.8 yields

$$J \simeq N_{tot} \left[\int_{n=n_{min}}^{n_{max}} \frac{1}{\beta_n f_{eq}(1)} \exp\left(\frac{\Delta G(n)}{k_B T} \right) dn \right]^{-1}. \tag{1.9}$$

When the free energy barrier is high, eqn. 1.9 may be approximated by the steepest descent approximation in which the major contribution to the integral comes from values centered around the location of the critical size of the embryo, n^*, which occurs at the maximum. Approximating the free energy around the location of the critical embryo, we obtain

$$\Delta G(n) \approx \Delta G(n^*) + \frac{1}{2} \frac{d^2 \Delta G(n)}{dn^2} \mid_{n^*} (n - n^*)^2. \tag{1.10}$$

The nucleation rate can now be written as,

$$J \approx \beta_{n*} f_{eq}(1) \exp\left(\frac{\Delta G(n^*)}{k_B T} \right) \left[\int_0^{\infty} \exp\left(\frac{\frac{1}{2} \frac{d^2 \Delta G(n)}{dn^2} \mid_{n^*} (n - n^*)^2}{2 k_B T} \right) dn \right]^{-1}. \tag{1.11}$$

Evaluating the integral in eqn. 1.11 yields the Zeldovich factor[37],

$$Z = \sqrt{\frac{\frac{-\partial^2 \Delta G}{\partial n^2} \mid_{n^*}}{2\pi k_B T}}, \tag{1.12}$$

and this results in the final form of the nucleation rate being given as

$$J_{CNT} = \beta_{n^*} Z N_{tot} \exp\left(-\frac{\Delta G(n^*)}{k_B T} \right), \tag{1.13}$$

where $\exp\left(-\frac{\Delta G(n^*)}{k_B T}\right)$ is related to the probability of seeing a cluster of the new phase containing n^* monomers, while $\Delta G(n)$ is the work of formation of an $n-sized$ cluster. Hence, the rate calculation can be formulated in terms of the work of formation of the new phase.

CNT calculates the free energy of formation by invoking the capillarity approximation, in which portions of the new phase are assumed to posses the properties of the bulk phase. The new phase is thermodynamically more stable than the metastable phase, therefore its free energy per unit volume is lower than that of the metastable phase. On the other hand, the creation of an interface increases the free energy by an amount that is proportional to the area of the surface created. The shape of the nucleus that minimizes this surface energy for a fixed volume is a sphere. Therefore, the free energy, $\Delta G(n)$, can be expressed as the sum of the volume and interfacial energy contributions,

$$\Delta G(n) = -\Delta\mu n + \sigma A(n), \tag{1.14}$$

where $\Delta\mu$ is the change in the free energy per unit volume between the metastable and stable phases, and σ is the surface energy per unit area. For undercooled vapors, and assuming ideal gas behavior, $\Delta\mu$ is given as,

$$\Delta\mu = k_B T \ln S, \tag{1.15}$$

where $S = p/p_{eq}$ is the supersaturation. Assuming a spherical shape for the cluster, $\Delta G(n)$ becomes,

$$\Delta G(n) = -nk_B T \ln S + \sigma s_1 n^{2/3}. \tag{1.16}$$

The value of n when $\frac{\partial \Delta G(n)}{\partial n}|_{n^*}=0$, is the *critical size*,

$$n^* = (\frac{2s_1\sigma}{3k_B T \ln S})^3. \tag{1.17}$$

The maximum in the free energy,

$$\Delta G^*_{CNT} = \frac{4(\sigma s_1)^3}{27(k_B T \ln S)^2} = \frac{4(\sigma s_1)^3}{27(\Delta\mu)^2}, \tag{1.18}$$

is the nucleation barrier [8, 38]. The height of the free energy barrier is dependent on temperature and pressure, and it diverges as the system approaches phase coexistence where $\Delta\mu$ goes to zero. In the solid nuclei, the shape is hardly spherical. Hence, the equilibrium shape of a solid embryo can be approximated using Wulffs construction[39]. This approach minimizes the free energy by changing the shape of the embryo and replacing the surfaces

associated with high energy facets with low energy facets. In such a case, the surface area used is the sum of all the areas of the different facets which gives the lowest free energy. The free energy of formation of an n-sized crystal is expressed as,

$$\Delta G(n) = \Delta\mu n + \sum \sigma_i A_i, \tag{1.19}$$

where the summation accounts for the different surfaces that the crystal may have, σ_i is the interface tension of surface i with surface area A_i.

CNT has been at the center of understanding nucleation for the last few decades. Its popularity and apparent success lies in its simplicity and the reasonable agreement of experimental results with theoretical predictions regarding the limits of stability for most substances[40]. But the major failing of CNT is its inability to predict the rates of homogeneous nucleation accurately. The assumptions of CNT that materials at the center of the embryo have the same properties as the bulk phase, and that the surface energy of a small spherical cluster is the same as that of an infinite planar surface become questionable when the nuclei contains few hundreds of molecules. Theoretical [1, 2, 3, 20] and experimental [31] evidence show that for liquid - solid nucleation, the nuclei are not necessarily spherical. The different surface facets have different surface energies [41], that are not equal to the surface energies of the bulk phase. This difference in surface energies will affect eqn 1.14, and hence, the rates obtained using eqn 1.13. Another major challenge in invoking CNT is the assumption that the interface between the stable and metastable phases is sharp. This assumption is not true at a molecular level. Also, CNT assumes that nucleation is a steady state process, in which clusters sizes, independent of time, are rapidly attained. The implication of this is that nucleation rate is constant. Though true in most cases, this assumption becomes questionable in cases where a finite time is required for the concentration of clusters to attain their steady values[42, 43]. Using CNT to describe crystallization presents some challenges, primary among them is the absence of independent measurements of the solid-liquid interfacial energy, σ, in the supercooled region. This quantity is mostly obtained by fitting the results of nucleation experiments to the CNT expression. Another challenge is the difficulties in identifying the solid embryo during crystallization. In this regard, Frenkel and coworkers[44] showed that the Steinhardt bond order parameters[14] can be used to identify the nuclei and calculate its size. This has been extended to identify solid nuclei[45, 1, 2, 3] and used as a major reaction coordinate in nucleation events. Size is an important parameter in nucleation,

but it does not contain enough information about the geometry of the nucleus or the different contributions of parameters such as surface area and internal order. These short comings of size call in to questioning its continuous use to characterize liquid-solid phase transition as proposed in CNT.

The limitations of CNT seen in experiments have caused an intense search for alternative theoretical models that can describe nucleation processes more accurately. One such model is the kinetic model. Its major characteristics is the direct calculation of the rate coefficients for evaporation and condensation without involving the constrained equilibrium hypothesis or the evaluation of the work of formation of the clusters. Using this model, Lovett [46] with the help of thermodynamics, estimated the critical radius and the height of the energy barrier for a monomer to leave the cluster surface. This model is applicable only to nucleation in gases and uses the macroscopic values of interfacial tension whose validity is questionable when applied to small clusters. Another kinetic approach by Bauer *et al* [47, 48] accounts for the interaction of the clusters with the carrier gas. This model requires two times the adjustable kinetic coefficients to fit to the experimental data. Also, the *Dynamic Nucleation Theory* (DNT) [49] is used to analyze nucleation in the gaseous phase. This approach evaluates the rate constants for cluster evaporation and condensation using variational transition state theory. The downside of this approach is that it is only applicable for the vapor-liquid nucleation. Recently Reguera developed the non-equilibrium thermodynamics model[40, 50] which he applied to nucleation kinetics for mesoscopic systems. He derived a modified Fokker-Planck equation as a function of the bond order parameters and used it to study time dependent homogeneous nucleation.

Density functional theories (DFT), which are based on order parameter description of phase transition, allow for a more formal interpretation of nucleation which falls between CNT and microscopic simulation methods. Unlike CNT, DFT models allow for the possibility of the interface between the cluster and the metastable phase being diffuse. The basic assumption of DFT is that a spatially inhomogeneous density $\rho(\mathbf{r})$ underlies the thermodynamic treatment of a nucleation event. It was Cahn and Hilliard [51, 52] that first proposed the density functional formalism, but Evans [53] showed that there exists a free energy functional of the density $G[\rho(\mathbf{r})]$ whose minimum determines the thermodynamic states. For nucleation, evaluating $\delta G/\delta\rho(\mathbf{r}) = 0$ gives the density profile of the critical nucleus, and from here the free

energy barrier ΔG^* can be calculated. The functional proposed by Cahn and Hilliard [51, 52] depends on a square gradient term which accounts for non-local contributions to the free energy. This square gradient approximation does not produce satisfactory results for sharp interfaces. To avoid this challenge, Oxtoby *et al* [54, 55] introduced a density functional constructed directly from the interaction potentials between the molecules. This functional has been used to study nucleation in different systems using different potentials [56, 57] including liquid - solid crystallization [58]. The formalism described above only described the evaluation of the nucleation barrier, with no insight into the kinetics of the nucleation process. Langer [59] developed a method to incorporate the kinetic component of nucleation into DFT models.

Different phenomenological models [60, 61, 62, 63] have been formulated to improve the expression for the work of formation of a cluster with the aim of reconciling experimental and theoretical measurements. Reiss *et al* [60, 61] proposed a two dimensional characterization of the embryo by including the volume, in addition to size, while calculating the free energy. Based on this, Weakliem and Reiss [64] derived the *Modified Liquid Drop model* which they used to perform numerous computer simulations to calculate the work of formation of the cluster. Reguera and co-workers [62] extended the modified drop model into the *Extended Modified Liquid Drop model* (EMLD), taking into consideration translational, vibrational and rotational fluctuations. Also, the capillarity approximation does not consider the contributions of translational, rotational, and vibrational degrees of freedom to the free energy of the cluster. The initial work of Lothe and Pound [65] introduced the need to include these contributions to correct the free energy of formation of the cluster. Reiss *et al* [66] solved the "translational-rotational" paradox while Reguera [40] explained its role in the nucleation of mesoscopic phase. Recently, Reguera and Reiss [63] combined the EMLD with *Dynamic Nucleation Theory* to form the *Extended Modified Liquid Drop-Dynamic Nucleation Theory* (EMLD-DNT). Other corrections to the CNT using the phenomenological models include the Self-Consistent theory [66, 67], Scaled Nucleation theories [68] and Diffuse Interface theory [69].

1.2 Competitive Nucleation and Polymorphism in Materials

Recently, nanomaterials have become important objects for broad research and development due to their potential of changing ways in which materials are created. They also hold high prospects in drug delivery [70]. Nano-sized materials have a wide range of functionalities which are not available in bulk materials. They have a high surface area to volume ratio that enhances chemical reactivity, increase mechanical strength and catalytic properties. At the nano scale, quantum effect sets in leading to novel electrical [71], magnetic [72] and optical properties. These properties in nanomaterials and the ability to use nanomaterials in drug delivery are sometimes structure dependent. The magnetic properties of Fe [73] and NdFeB [74] nanoparticles have been shown to be affected by the anisotropy of their surfaces. Also, nanocrystals with branched structures, including monopods, bipods, tripods and tetrapods are in high demand [75] due their high electrical conductivities. In the pharmaceutical sector, magnetite and maghemite nanopartcles are used in medical imaging [70], due to their enhanced magnetic properties which is a function of their structures. The surface morphologies of nanomaterials allow them to selectively discharge at pathological sites [70] when used in drug delivery. Also, different crystalline forms of the active ingredient in drugs have different solubilities and different bio-availabilities [5]

The different structures or polymorphs of the nanomaterials are formed due to competition during nucleation, growth or impingement [76](The competition during nucleation may be due to the competition between the thermodynamics and kinetics of the nucleation or between the different modes of nucleation [76]. Competition during growth arises from competition in thermal diffusion and short-range or long-range solute diffusion [76]. Nucleation can be regarded as both a thermodynamic and kinetic event simultaneously. Thermodynamically, only nuclei that overcome the maximum work of forming a new phase can go over the nucleation barrier. Kinetically, nucleation can be explained as a steady state growth and dissolving of the new phase till the maximum nucleus size is attained. The exact nature of the competition between thermodynamics and kinetics that determines the phase selection depends on the system and its inherent conditions.

Competitive nucleation occurs when a single metastable phase can nucleate to any of the possible stable structures or phases. This phenomenon is common in many physical processes,

such as nucleation in atomic clusters [1, 2, 3, 20, 31], crystallization of protein [77], where the presence of huge number of potential energy minima may prevent the system from reaching the global equilibrium [78]. The crystallization of *levo-* and *dextro-* sodium chlorate crystals from a single solution, thus making them optically active [79], can be explained in terms of competitive nucleation. J. A. D Wattis [80] applied the Becker and Döring systems of equation [35] to competitive nucleation for the first time. In his work, the author proposed a model where two different clusters can form from a single type of monomer having constant concentration. Also, the author allowed for one of the clusters to be non-crystalline, for example, amorphous or a gel.

The spin lattice model has often been used to explain nucleation and also to test new simulation algorithms and methodologies. The Ising model has two phases ($q = 2$) and has been used to study various nucleation processes[11, 12, 81, 82]. In particular, the simplicity of the spin model, and the ease with which it can be simulated means that it is an ideal model for testing new nucleation theories and for developing new methods for the study of rare events[11, 12]. For example, Shneidman *et al* [82] tested the applicability of CNT in the Ising model. They observed that at intermediate temperatures (up to 70% of the critical temperature), the distribution of large clusters is in qualitative agreement with CNT, but, their measurement of the nucleation rate differed by a constant factor. Scheifele *et al* [81] also used a 2-dimensional Ising model to study heterogeneous nucleation in the low-barrier regime. They redefined the free energy barrier using the metastable state containing the impurity as the reference state. Their results show that renormalization of the free energy barrier accurately predicts the nucleation rate and is consistent with the nucleation theorem.

Sanders *et al*[7] used the generalized Potts model[83, 84] to study homogeneous competitive nucleation with many metastable phases. Their results showed that the rate of nucleation to a given phase depends on the external field strength of such a phase. They also showed that in cases of competitive nucleation, a probabilistic approach is required in the calculation of the rates. Sear[85] studied competitive heterogeneous nucleation using the Potts model. He investigated the nature of the impurity that favors the nucleation of the phase that is not the equilibrium phase on an impurity. His results showed that though the equilibrium phase may have a favorable external field, the less stable phase with highest interaction with the impurity will nucleate on the impurity. In the works of Sanders *et al*[7] and Sear[85],

there was no explicit definition of order parameter(s) or reaction coordinate by which the transition dynamics can be understood. Knowing the reaction coordinate for any process is very important in understanding the progress of the process, as it can provide mechanistic insight to the nucleation and can help identify why one product is preferred over others.

1.3 Transition Path Sampling

Transition Path Sampling (TPS), developed by Chandler *et al.* [86, 87], is a computational methodology used to study rare transitions between known and well defined states based on the statistical mechanics of trajectories. Its major advantage is that it does not require *a priori* information on the mechanism [88]. Since nucleation is a rare event, the efficiency of TPS is increased by focusing mainly on the reactive trajectories [12]. The trajectories are said to be reactive when they connect the initial and the final states together, *i.e* when the forward trajectory ends in the product and backward trajectory ends in the reactant or *vice versa*. TPS, in its different versions, has been successfully used to study ice nucleation [89, 90], protein folding[91] and Grotthus proton transfer[92]. The idea behind TPS consists of assigning a probability or weight to every pathway, where this probability is a statistical description of all possible reactive trajectories known as the transition path ensemble (TPE) [12]. For a system with a single initial state (reactant A) and a single product, B, (see fig. 1.2), the TPE can be expressed mathematically [93] as it obeys probability,

$$P_{AB}[\mathbf{x}(L)] \equiv Z_{AB}^{-1} h_A(\mathbf{x}_0) P[\mathbf{x}(L)] h_B(\mathbf{x}_L) \tag{1.20}$$

where Z_{AB} is a normalization factor, while h_A and h_B are characteristic functions defining the states A and B, such that their values are unity if the configuration x is within the region, and zero otherwise,

$$h_A(\mathbf{x}) = \begin{cases} 1, & if\ \mathbf{x} \in \mathbf{A} \\ 0, & if\ \mathbf{x} \notin \mathbf{A}. \end{cases}$$

Similarly,

$$h_B(\mathbf{x}) = \begin{cases} 1, & if\ \mathbf{x} \in \mathbf{B} \\ 0, & if\ \mathbf{x} \notin \mathbf{B}. \end{cases}$$

$P[\mathbf{x}(L)]$ is the dynamical path probability for a path

$$\mathbf{x}(L) = \{\mathbf{x}_0, \mathbf{x}_{\Delta t}, ..., \mathbf{x}_{L\Delta t}\}, \tag{1.21}$$

where $\mathbf{x}_{\Delta t}$ denotes the complete microscopic state of the system at time interval Δt, L is the length of the transition path.

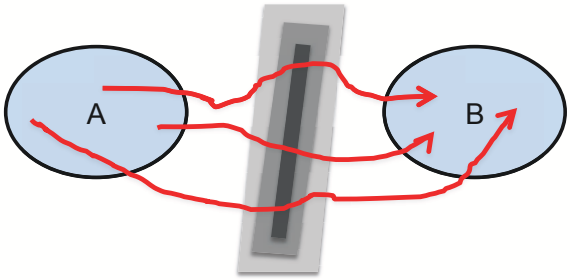

Figure 1.2: A diagram showing TPS with regions **A** and **B** in phase space corresponding to locally stable phases.

In TPS, the definition of the TPE requires that locally stable phases **A** and **B** be specified. To do this, one dimensional order parameters or collective variables, say, $q_A(\mathbf{x})$ and $q_B(\mathbf{x})$ are defined for each of the phases. It should be noted that these order parameters are sufficient to specify the stable states but may not necessarily be suitable to describe the complete transition. The term *reaction coordinate* is exclusively reserved for specific collective variables or their combinations that describes a transition's dynamical mechanism.

The analysis of these harvested pathways yields the required mechanistic information on the transition mechanism. To use TPS, the transition path has to be well defined in relation to the configuration landscape. The transition path probabilities, $p(TP|\mathbf{x})$, are the probabilities of trajectories initiated from a configuration, x, connect both reactant and product. A committor probability is defined as the fraction of trajectories initiated with a Boltzmann distributed momenta from a given configuration, x, that commit to the product basin[87]. Representing the committor probability as $pB(\mathbf{x})$, then the transition states are configurations for which $pB(\mathbf{x}) = 0.5$, for the reactant configurations, $pB(\mathbf{x}) < 0.5$, while product configurations have $pB(\mathbf{x}) > 0.5$. The evaluation of $pB(\mathrm{x})$ is computationally expensive and does not provide useful insight into the physical characteristics that distinguish reactants, products and transition states[12]. For complex systems, such as condensed phases, a simple approximation to $pB(\mathbf{x})$, as a function of collective variables, is more useful[12] and computationally feasible. Collective variable, $q(\mathbf{x})$, are functions of the configuration that compress several microscopic details into physically important variables. There are many methods for sampling the transition path ensemble which can be broadly divided into shooting and

shifting methods. The shooting method has gained much popularity and here the Aimless shooting method of transition path sampling is explained briefly.

1.3.1 Aimless Shooting Method

Aimless shooting [12] is a version of TPS where a point in configuration space $\mathbf{x}_t^o$ is selected from the old transition path, $\mathbf{x}_0$. The chosen state may be modified in a manner suitable for the propagation mechanism. For example, in a system with deterministic dynamics, the momenta are drawn from the Maxwell-Boltzmann distribution for each trial trajectory [94, 12]. The modified state is then propagated forward and backward in time using the appropriate dynamics until the new path connects the stable basins. Fig. 1.3 depicts this procedure, where the new pathway (dashed line) is generated from the old pathway (solid line). The new pathway is reactive if the forward trajectory (f) ends in **A** and backward trajectory (b) ends in **B** or *vice versa*. If the pathway is reactive, it is accepted into the transition path ensemble and rejected otherwise. The difference between the new point, $\mathbf{x}_t^o$ and the old point, $\mathbf{x}_0$, is Δt. Δt should be chosen to be very small compared to the duration of the reactive trajectory, t ($\Delta t << t$). The value of Δt affects the efficiency of the shooting algorithm, though a wider range of values may be acceptable. To achieve high efficiency, most shooting points must be chosen to be very close to unknown $p_B = 0.5$ surface.

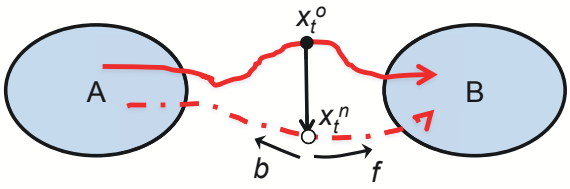

Figure 1.3: A diagram showing the generation of a new transition pathway from an old transition path in an Aimless shooting method.

Trajectories obtained by aimless shooting reflects the system's dynamics, therefore, the corresponding generation and acceptance probabilities also depend on the dynamics, and the algorithm is relatively simple to execute [94]. For deterministic dynamics with initial velocities, $\mathbf{V}_{t_0}$, the probability for generating a new trajectory $\{x^n_{\pm t/2}\}$ is

$$p_{gen}^{o\to n} = \frac{1}{9}\rho_{eq}(V_{t_0})p(\{x^n_{\pm t/2}\}|V_{t_0}, x^n_{t_0}, t_0). \tag{1.22}$$

ρ_{eq} is the Boltzmann distribution, while the probability $p(\{x^n_{\pm t/2}\}|V_{t_0}, x^n_{t_0}, t_0)$ depends on the equation of motion [12]. The new shooting point can be selected from $x^o_{-\Delta t}$, x^o_t, and $x^o_{\Delta t}$, hence the factor 1/9. The ratio of the generation probabilities is

$$\frac{p^{o\to n}_{gen}}{p^{n\to o}_{gen}} = \frac{\rho_{eq}(V^n_{t_0})p(\{x^n_{\pm t/2}\}|V^n_{t_0}, x^n_{t_0}, t^n_0)}{\rho_{eq}(V^o_{t_0})p(\{x^o_{\pm t/2}\}|V^o_{t_0}, x^n_{t_0}, t^o_0)}, \tag{1.23}$$

and maintains detailed balance [95] in the transition path ensemble which is achieved by accepting each new trajectory connecting states **A** and **B**. The forward and backward reactions are included in the TPE by accepting trajectories with a probability

$$TPE_{acc} = h_A[x^n_{-t/2}]h_B[x^n_{t/2}] + h_A[x^n_{t/2}]h_B[x^n_{-t/2}]. \tag{1.24}$$

The $\pm t/2$ in eqns. 1.22, 1.23, and 1.24 indicate that the forward and backward trajectories are half the length of a full trajectory.

Aimless shooting can be applied to both deterministic and stochastic dynamics and the moves described above are identical to moves applied for stochastic dynamic. For a deterministic simulation such as Molecular Dynamics, the backward segment is propagated with the direction of time inverted. This is done by integrating the equation of motion with a negative time step or first inverting the velocities and integrating forward in time [94]. In a stochastic dynamics such as Monte Carlo, it is not necessary to modify the shooting point before shooting. The random nature of the dynamics causes the new path to diverge from the old path. Here, the generation probability $p^{o\to n}_{gen}$ is symmetric and the acceptance probability becomes

$$TPE_{acc} = h_A[x^n_0]h_B[x^n_t], \tag{1.25}$$

which means any trajectory connecting **A** and **B** are accepted in the transition path ensemble.

Since its development by Chandler *et al* [86, 87], TPS has been applied to understanding the dynamics of phase transitions[11, 12, 16, 17] and other rare events[91, 92]. It has also been used to understand chemical and biological phenomena. Pan *et al* [11] used the aimless shooting method of TPS to study the nature of critical nuclei in homogeneous nucleation in a 3D Ising model. Their result shows that the critical nuclei is anisotropic and suggested that there maybe contributions from other order parameters to the reaction coordinate in addition to the size of the embryo. Another phase transition which has been studied with aimless shooting is the freezing of Lennard-Jonnes particles[17], where the authors observed that the

product of embryo size and the bond orientational order parameter of the embryo is the best reaction coordinate. Also, Beckham *et al*[96] used the aimless shooting method to understand the solid-solid transition of terephthalic acid. TPS has also been used to study phase separation and crystallization of sodium halides from their melts[97]. TPS has been used to study some chemical processes including proton transfer in the water trimer[92], hydrated proton transfer in water[98], and the isomerization and melting of water clusters[99]. In biological systems, TPS has been used to investigate the isomerization of alanine dipeptide[91, 19] and DNA repair process by polymerase[100].

1.4 Maximum Likelihood Analysis

To obtain a good reaction coordinate, r(x), the transition path probability, $p(TP|r(\mathbf{x}))$, must be a function of the reaction coordinate only. This is achieved by screening the collective variables for the function $p(TP|r(\mathbf{x}))$ that will suitably explain the realization of $p(TP|\mathbf{x})$ obtained from the aimless shooting. Likelihood maximization [101] determines the optimum reaction coordinate by screening a large set of collective variables and finding the combination of the collective variables that best fit the observed data. It has the advantage of not requiring the calculation of the committor probabilities, but rather uses the statistics about the accepted and rejected trajectories accumulated during the aimless shooting. The generated statistics will then be analyzed using the maximum likelihood estimation which is a statistical method that determines the parameters of a postulated underlying model from a given data set. The model function used for $p(TP|r)$ must be such that it peaks at the transition state value of r, and decays to zero on both sides of the peak. One commonly used function is,

$$p(TP|r) = p_0(1 - \tanh[r]^2) \tag{1.26}$$

where p_0 is an adjustable parameter. This function (eqn. 1.26) is symmetric with a peak at $r = 0$, such that the transition states are found at the isosurface $r(\mathbf{x}) = 0$. p_0 can be determined *a priori* for two limiting cases. For systems that obey transition state theory, the transition state $\mathbf{x}$ is such that, the forward and backward trajectories must end in the product and reactant, respectively. This implies that $\mathbf{x}$ satisfies $p(TP|\mathbf{x}) = 1$, hence, $p_0 = 1$. For systems with diffusive barrier crossing mechanism, such as nucleation, transition states

satisfy $p(TP|\mathbf{x}) = 0.5$ [101]. Transition states are on the surface $r(\mathbf{x})$ and

$$p(TP|\mathbf{x}) = 2p_B(\mathbf{x})(1 - p_B(\mathbf{x})) \tag{1.27}$$

where $p_B(\mathbf{x})$ is the committor probability, then $p_0 = 1/2$, while

$$p_B = (1 + tanh[r])/2. \tag{1.28}$$

Fig. 1.4 shows the functions $p_B(r)$ and $p(TP|r)$ for a system with diffusive barrier crossings. The realizations of the transition path probabilities must have the shape of $p(TP|r)$ for this model to be useful.

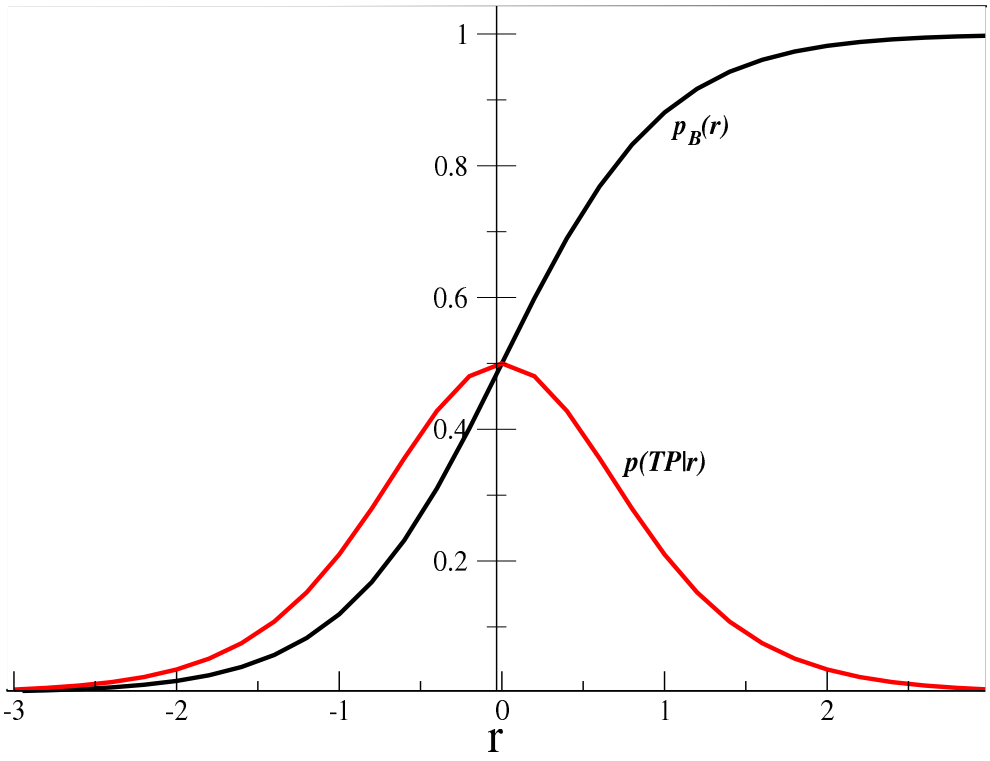

Figure 1.4: The $p(TP|r)$ and p_B functions for a system with diffusive barrier crossing.

To apply the maximum likelihood estimation, the underlying model in the form of parameter-dependent probability distributions for the data needs to be specified. The data will consist

of the observed acceptances and rejections for a large number of shooting points with their corresponding values of M collective variables $q_1, q_2.....q_M$ [101]. The definition of the model is achieved by stipulating the dependency of the expected reaction coordinate q on the M collective variables. One possibility of such a model is;

$$q = \alpha_0 + \sum_{k=1}^{M} \alpha_k q_k + \sum_{k,l=1}^{M} A_{kl} q_k q_l, \tag{1.29}$$

where α_0 is a free parameter that allows the reaction coordinate to shift so that the transition states appear at $r(q) = 0$. The second term is a linear combination of order parameters weighted by α_k, while the third term is the sum of the correlations between the order parameters weighted by the matrix element A_{kl}. The next step will be to construct a likelihood function, L, which quantifies the probability of the observed data as a function of the model parameters;

$$L(\alpha) = \prod_{r \in acc} p(TP|q(r)) \prod_{r \in rej} [1 - p(TP|q(r))], \tag{1.30}$$

where, α denotes all model parameters including the coefficients, α_k and the matrix elements, A_{kl}. The first product is over all the accepted transitions while the second product is for all the rejected trajectories. Maximizing the likelihood function (eqn. 1.30) above with respect to the parameters, α, will yield the optimum reaction coordinate. In practice, it is easier and more convenient to maximize the logarithm of eqn. 1.30,

$$\ln L(\alpha) = \sum_{r \in acc} \ln p(TP|q(r)) + \sum_{r \in rej} \ln[1 - p(TP|q(r))]. \tag{1.31}$$

The maximum likelihood analysis constructs the best reaction coordinate from a few collective variables. These few variables are often sufficient to obtain the reaction coordinate, the major challenge is how to determine which variables are important. Peters *et al.* [12] showed that this challenge can be overcome by a systematic search. For a set of M collective variables, the search starts with each of the M variables in the model for the reaction coordinate. The best single variable reaction coordinate is compared with the best from all the pairs of the collective variables. The best reaction coordinate from the pairs of order parameters is compared with the combinations of three or more variables. The Bayesian information criterion [102], BIC, determines if the addition of a new variable is significant to the reaction coordinate. If the additional parameter increases the likelihood estimate by

$0.5 \ln N_R$ [102], where N_R is the number of realizations in the likelihood function, then the new variable is regarded as significant.

The maximum likelihood analysis does not require the evaluation of the computationally expensive committor histogram, as such, it is a flexible and computationally efficient method of finding reaction coordinates. It has been successfully used to study the mechanistic details of homogeneous nucleation in Ising model[12, 11]. Beckham *et al*[103] used Maximum likelihood analysis to obtain the accurate reaction coordinate for the solid-solid transition of terephthalic acid. Using the maximum likelihood analysis, Lechner *et al*. [20] showed that reaction coordinates can be non-linear.

1.5 Scope of the Thesis

The major objective of this thesis is to develop a molecular understanding of the dynamics of competitive nucleation. In order to achieve this objective, the question: **What is (are) the most suitable reaction coordinate(s) that can be followed to properly understand the dynamics of the formation of different structures during the nucleation of nanoclusters?** must be answered. The evolution of the different structures during nucleation of nanoclusters are studied by following the global, local and structural order parameters of the system. These order parameters and their combinations are tested as suitable reaction coordinates for the different transitions using the maximum likelihood analysis.

Chapter 2 examines the competitive nucleation between the different phases forming on a nanoscale heterogeneity using the Potts model. The free energy surfaces for nucleation at different external field strengths and different interaction parameters are calculated using Monte Carlo simulations. The normalized free energy barriers are used to calculate the rate of nucleation to each of the phases using transition state theory. The survival probability and mean first passage time methods are also used to evaluate the overall rate for the formation of a stable phase. This overall rate is combined with the probability of seeing the phase within an ensemble of nucleation events to find the rates to each of the phases.

An important variable in understanding the mechanism of any process is the reaction coordinate. In Chapter 3, the aimless shooting method of transition path sampling is extended to study competitive nucleation, where multiple transitions may occur using the Potts

model as the test system. The transition path probabilities are evaluated as a function of different order parameters of the shooting points. The multiple path maximum likelihood expression is developed and used to maximize the probabilities of configurations being on a given transition path.

In Chapter 4, molecular dynamics simulations are used to study nucleation phenomenon in gold nanoclusters of size range $300 \leq N \leq 1000$ at different temperatures. Different structures are identified using different set of order parameters. The overall rates of nucleating to any structure for each of the cluster size as a function of temperature is calculated using the survival probability method. The probability of observing each structure in an ensemble of nucleation events is measured. These probabilities are then used to calculate the rate of formation of each of the structures, and obtain estimates of the nucleation free energy barriers to the structures at each temperature.

In Chapter 5, the aimless shooting method is applied to the competitive nucleation of gold nanocluster of size $N = 561$ at $T = 700\ K$. The transition path probabilities as a function of global, local and structural order parameters are calculated. The multiple path maximum likelihood analysis developed in Chapter 3 is used to test for the best reaction coordinate for the different transitions. Many order parameters and their combinations are screened as reaction coordinates and these are used to gain mechanistic insight into the formation of Ih, Dh, and FCC structures.

The summary of the important findings in this thesis and their implications to nucleation of nanoclusters in particular or phase transitions in general are presented in Chapter 6. The direction of future work is also suggested in this chapter.

Chapter 2

Competitive Rates of Heterogeneous Nucleation in a Potts Model

2.1 Introduction

One of the major objectives of this thesis is to understand the dynamics of competitive nucleation in nanoclusters. Understanding the dynamics of competitive nucleation is essential to the production of materials whose desired properties are structure dependent, and in the understanding of certain disease conditions. In a competitive process, the probabilities of having a given structure and their rates of formation are said to be determined by the nucleation barrier and the growth kinetics [3, 7]. Also, the rate of any nucleation event is dramatically increased by the presence of heterogeneous surface due to the lowering of the free energy barrier to processes such as vapor condensation and crystallization [8]. Hence, heterogeneous nucleation is more abundant in nature than homogeneous nucleation and is responsible for important atmospheric physics [9] as well as protein crystallization [104].

Lattice models have often been used to explain nucleation and also to test new simulation algorithms and methodologies. In condensed matter physics, the commonly used lattice models include the Ising, Potts, and Toda models which are lattice models having spins in one or more directions. In the presence of an external field, these spin models undergo first order phase transition, which makes them attractive as useful models to explain nucleation. The Ising model has two phases ($q = 2$) corresponding to the system with all spins up or all spins down, and has been used to study various nucleation processes [11, 12, 81, 82], in the study of magnetic materials [105, 106, 107], and in developing methods for studying rare events [11, 12]. The Potts model is an extension of the Ising model where each spin can take any number of possible states, $q = 3, 4, 5.....$ The Potts model with $q = 3$ has been used to study the dynamics of liquid - solid nucleation [108] due to the simplicity. Also, Potts models

have been used to test the validity of Ostwald's rule during the competitive heterogeneous nucleation [85] and competitive homogeneous nucleation [7]. Fig. 2.1 shows transition graphs representing different scenarios where the Ising and Potts models can be used to study phase transitions. In each case, the system starts in the metastable phase, **A**. Fig.2.1 (a) is the basic Ising model that exhibits a phase transition to a single more stable phase, (b) shows the transition graph for a succession of three phases where the system initially transforms to an intermediate metastable phase before finally transforming to the most stable phase, (c) shows the formation of two competing stable phases from a single metastable phase, (d) shows the scenario found in (c), but with phase C nucleating to form another phase, while (e) shows the formation of three competing phases. Sanders *et al* [7] used the generalized Potts model [83, 84] to study homogeneous competitive nucleation of many phases. Their results showed that the applications of Ostwald's rule should be interpreted probabilistically because there is a chance that any of the phases could nucleate. They also showed that the rate of nucleation depended on the probability of observing a nucleus, so the rate was effected by the number of potential phases that could be formed.

Most nucleation processes in nature are heterogeneous rather than homogeneous. Sear [85] studied competitive heterogeneous nucleation using the Potts model. He investigated the nature of the impurity that favors the nucleation of a phase that is not the equilibrium phase on an impurity. His results showed that though the equilibrium phase may have a favorable external field, the less stable phase with the strongest interaction with the impurity will nucleate on the impurity.

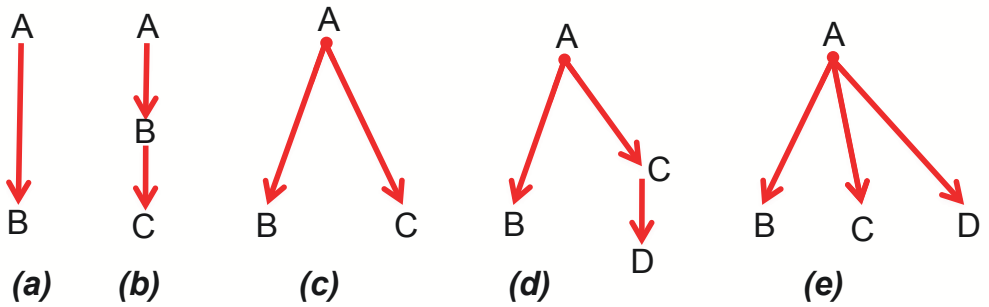

Figure 2.1: Transition graphs depicting Ising and Potts models.

In this chapter, the rates of formation of new phases on an impurity using a simple spin model with nearest neighbor interaction is measured. In the Potts model used here, the interaction between the phases and the impurity are equal, removing any advantage of one phase over the other. The free energy surfaces for the formation of different phases at different field strengths and interactions are calculated. Then using the transition state theory (TST) developed by Volmer and Weber [34], Becker and Döring [35], Zeldovich [109], and Frenkel [36], the individual rates to the new phases are calculated. The rates are subsequently compared with the rates obtained through the mean first passage time (MFPT) [110] and survival probability [1] methods. The remainder of this chapter is organized as follows: Section 2.2 describes the model and the simulation methods used to calculate the free energy surfaces and the nucleation rates. Section 2.3 describes the results from the different methods used to calculate the rates of nucleation while Section 2.4 discusses the general features of competitive nucleation and compares the rates from the different methods, and Section 2.5 has the conclusions to this chapter.

2.2 Model and Methods

2.2.1 Model

The system used in this study is the three state Potts model [83, 84] nucleating in the presence of a heterogeneity. The transitions are represented by graph **c** in fig. 2.1. There are $q = 3$ phases, with one phase being the metastable phase and two more stable phases. The heterogeneity could be considered to be a fourth phase, with different interactions, but the spins associated with the heterogeneity cannot change.

The system consists of $L \times L = 40 \times 40$ square lattices with a total number of spins $N = L^2$ within a period boundary. Each lattice site i has a spin σ_i with values $\{1, 2, 3, 4\}$, where the $\sigma_i = 1$ is for the metastable phase, $\sigma_i = 2$ and $\sigma_i = 3$ are for the stable phases, while $\sigma_i = 4$ is for the fixed heterogeneity. The energy of a given configuration is

$$E(\sigma) = -\sum_{\langle i,j \rangle} \mathbf{J}_{\sigma_i,\sigma_j} - \sum_{\alpha=1}^{q} H_\alpha M_\alpha, \tag{2.1}$$

where J_{σ_i,σ_j} is the interaction energy between neighboring spins σ_i and σ_j, and the sum in

the first term is overall possible spin neighbor pairs. In the second term,

$$M_\alpha = \sum_i^N \delta_{\sigma_i,\alpha}, \tag{2.2}$$

is the magnetization of the spin type α, where,

$$\delta_{\sigma_i} = \begin{cases} 1, & \sigma_i = \alpha \\ 0, & otherwise, \end{cases}$$

and H_α is the external field strength, which controls the relative stability of each of the phases. It is the interplay of these field strengths, coupled with the interaction energy that allows the transition paths between the different phases to be tuned. Here, the field strengths are selected such that, $H_A < H_B \leq H_C$ while $\mathbf{J}_{A,B} = \mathbf{J}_{A,C}$ and $\mathbf{J}_{B,C} < 0$ which ensures that phase **A** is the metastable mother phase. Also, the value **J** is such that the diagonal elements $\mathbf{J}_{\alpha,\alpha}$ equals to unity (i.e $\beta\mathbf{J}_{\alpha,\alpha} = 1$ for all α). The choice of the interaction parameters between the stable phases and the impurity ensure that nucleation occurs on the impurity only. $\beta\Delta H = \beta H_C - \beta H_B$ is the field difference between phases B and C. To make the probability of the phases B and C nucleating from the metastable phase equal, the field difference is set as $\beta\Delta H = 0$, so that the $A \rightarrow B$ free energy barrier is expected to be equal to the $A \rightarrow C$ barrier. Also, $\beta\Delta H = 0$ ensures a possible transition between phases B and C. For all the simulations, a constant temperature of $k_B T = 1.5$ is used. The system consists of an impurity made of a single line of spins of length $l = 7$. Fig. 2.2 shows two stable phases surrounding an impurity (black lattices). The white background represent the metastable phase, while the light grey and dark grey lattices are the B and C phases respectively.

2.2.2 The Nucleation Free Energy Surface

In calculating the free energy surface for the Potts model, the aim is to evaluate the minimum reversible work of formation of a critical cluster containing a stable phase. A critical cluster can be defined as a contiguous cluster of the stable phases surrounding the impurity. In addition to the impurity whose size is fixed, a cluster contains different number of spins representing the stable phases, n_B and n_C. In order to obtain the free energy surface, the partition function of the system with a fixed N, H_B, H_C, T and l is defined as,

$$\mathbb{Z} = \sum_{n_B=0}^{N} \sum_{n_C=0}^{N} Z(n_B, n_C), \tag{2.3}$$

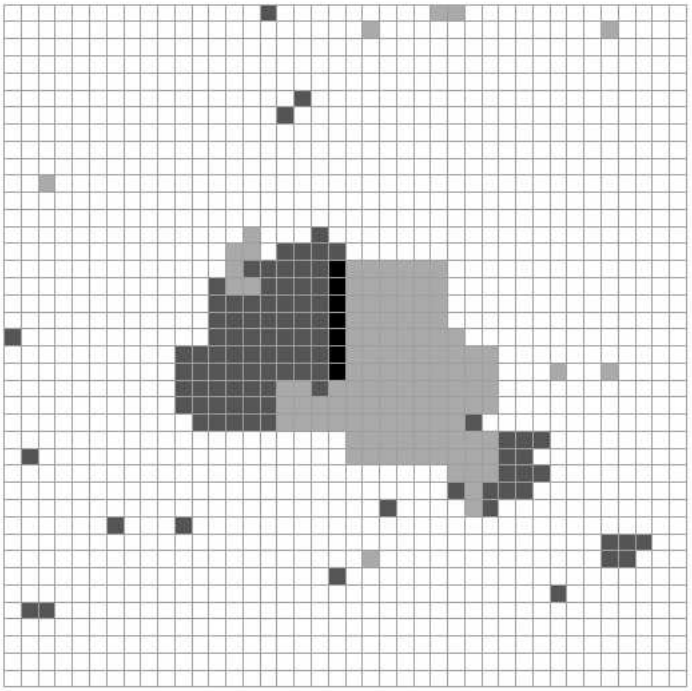

Figure 2.2: Example of configuration of Potts model with $\mathbf{J}_{B,C} = -1.0$, $H_B = H_C = 0.12$. The light grey and dark grey lattices are the stable phases, the black lattices represent the impurity. The white background represents the metastable phase.

where

$$Z(n_B, n_C) = \sum \exp(-\beta E(\sigma)). \tag{2.4}$$

The summation in the definition of $Z(n_B, n_C)$ is for all configurations with the cluster having n_B and n_C spins. The free energy as a function of n_B and n_C is given as

$$G(n_B, n_C) = -kT\ln Z(n_B, n_C). \tag{2.5}$$

Wolde *et al* [44] defined the free energy barrier to homogeneous nucleation as the minimum reversible work required to constrain the system to the transition state. Following this definition, Scheifele *et al* [81] renormalized the free energy barrier to heterogeneous nucleation with the partition function of the metastable phase. The nucleation time, τ, obtained through this free energy barrier was consistent with calculations using other methods [81]. Applying this normalization to this system, the partition of the metastable phase is defined as,

$$Z_m = \sum_{n_B=0}^{n_B^*} \sum_{n_C=0}^{n_C^*} Z(n_B, n_C), \tag{2.6}$$

where the embryos with size (n_A^*, n_B^*) represent the critical states at the boundary between the metastable phase and the states where the embryo spontaneously grow into the new stable phase. The free energy of the metastable phase is $G_m = -kT\ln Z_m$. Therefore, the work of forming an embryo having n_B, n_C spins on the heterogeneity from the metastable phase is given as

$$\Delta G(n_B, n_C) = G(n_B, n_C) - G_m = -kT\ln\frac{Z(n_B, n_C)}{Z_m}. \tag{2.7}$$

This re-normalization is supported by the fact that the present system is one where there is always one maximum cluster containing the impurity, such that n_B, n_C can be considered to be order parameters that describe the microscopic state of the system.

In order to calculate $\Delta G(n_B, n_C)$, a Monte Carlo (MC) simulation is carried out for a system with $\beta H_A = -0.120$ and $\beta H_B = \beta H_C = 0.120$. To improve the sampling of low probability states, such as the critical embryo, the umbrella sampling method is applied. This is achieved by adding a biasing potential, $U_B = \kappa_B(n_B - n_{0B})^2 + \kappa_C(n_C - n_{0C})^2$, to the potential energy of the system in eq. 2.1, where n_{0B} and n_{0C} are the umbrella centers for components B and C respectively. κ_B and κ_C are the umbrella constants which control the fluctuation of the components from the umbrella centers. To access the entire energy

landscape, a grid of $n_{0B} \times n_{0C}$ is used as the umbrella centers where n_{0B} and n_{0C} range from 0 to 110 at the interval of 10. At each MC move, a spin is randomly flipped and the move is accepted with a probability $min\{1, exp(-\beta\Delta E)\}$. One Monte Carlo step (mcs) is equivalent to $N = L^2$ MC moves. For each umbrella center, the simulation runs for 6.4×10^5 mcs, saving n_B and n_C after each 250 mcs. The Multiple Bennett Acceptance Ratio (MBAR) estimator [111] is used to connect data from different umbrella centers together forming a smooth free energy surface. This approach gives the probability of observing a n_B, n_C cluster in the biased simulation window, which results in free energies for a given cluster size that differ by an additive constant. The MBAR method provides a way of removing the biases in each simulation window and matching the windows together to form a complete unbiased free energy surface.

The free energy surfaces are similarly calculated for two additional conditions. The second case is the heterogeneous nucleation to the stable phases having unequal fields, where $\beta H_A = -0.120$, $\beta H_B = 0.120$ and $\beta H_C = 0.170$. In the last scenario, unequal fields are still used , but a partial mixing of the spins of the stable phases is allowed. This is achieved by increasing the value of $\beta \mathbf{J}_{B,C}$ to $\beta \mathbf{J}_{B,C} = -0.8$ from $\beta \mathbf{J}_{B,C} = -1.0$ used for the first two scenarios. The full set of cases studied are summarized in Table 3.1.

Cases	βH_A	βH_B	βH_C	$\beta J_{B,C}$	q
case **1**	-0.12	0.12	0.12	-1.0	3
case **2**	-0.12	0.12	0.17	-1.0	3
case **3**	-0.12	0.12	0.17	-0.8	3
case **4**	-0.12	0.12	-	-	2

Table 2.1: Summary of conditions and parameters used to calculate the free energy surfaces and the rates. The free energy surfaces were calculated for cases **1-3**.

2.2.3 Competitive Rates of Nucleation

The aim of this work is to calculate the rates of nucleation to different phases in a competitive process on an impurity. The rates are calculated using three different independent methods of evaluating rates of nucleation. The first approach is by using the transition state theory (TST) [36, 112] to calculate the rates $J_{B_{TST}}$ and $J_{C_{TST}}$ to phases B and C, respectively. In

using TST, the assumption that the transition to each of the stable phases is a mutually exclusive event and independent of each other is made. Therefore, the rates are defined as

$$J_{B_{TST}} = f_B^+ z_B \exp(-\beta \Delta G(n_B^*, n_C)), \tag{2.8}$$

and

$$J_{C_{TST}} = f_C^+ z_C \exp(-\beta \Delta G(n_B, n_C^*)), \tag{2.9}$$

where f_B^+ and f_C^+ are the rates of attachment of the spins B and C to the critical clusters leading to B and C phases. To obtain f_B^+, ten different configurations within the umbrella centers containing the critical size n_B^* are chosen. Using these configurations as initial configurations, MC simulations are performed to evaluate the rate of attachment from

$$f_B^+ = \frac{\langle \Delta n_B^2(t) \rangle}{2t}, \tag{2.10}$$

where $\langle \Delta n_B^2(t) \rangle$ is the mean square fluctuation of component B in the cluster, $\Delta n_B(t) \equiv n_B(t) - n_B(0)$. $\langle\ \rangle$ in the expression indicates the ensemble average from these MC simulations which were stopped when $\mid \Delta n_B(t) \mid > 20$. The same procedure is repeated for component C to evaluate f_C^+. z_B is the Zeldovich factor defined as

$$z_B = \sqrt{\frac{\beta \eta_B}{2\pi}}, \tag{2.11}$$

where $\eta_B = -(\delta^2 G / \delta n_B^2)_{n=n_B^*}$ is the curvature at the top of the barrier. For a given transition, η_B is obtained from a quadratic fit to the data within $0.2kT$ of the barrier along the channel.

Given that a system can spontaneously nucleate to any one of the possible phases, the rates can be considered as rates of parallel processes. For a system, with total number of trajectories, N_T, all starting from phase **A**, with each trajectory forming phase **B** or **C**. The total number of transitions to different phases are conserved such that $N_T = N_A + N_B + N_C$, where N_A is the number of unnucleated trajectories, N_B is the number of trajectories forming phase **B** and N_C is the number of trajectories forming phase **C**. Considering N_T as the initial quantity of the reactant, the rate of forming **B** is given by,

$$rate_B = \frac{dN_B}{dt} = k_b N_A, \tag{2.12}$$

where k_b is the rate constant associated with crossing the barrier. Similarly, the rate for the formation of **C** is given by

$$rate_C = \frac{dN_C}{dt} = k_c N_A. \tag{2.13}$$

Finally, the overall rate for the disappearance of **A** is given by

$$rate = -\frac{dN_A}{dt} = (k_b + k_c)N_A. \tag{2.14}$$

If all the trajectories start as phase **A**, at time t=0, then integrating eq. 2.14

$$-\int_{N_T}^{N_A} \frac{dN_A}{N_A} = \int_0^t (k_b + k_c)dt, \tag{2.15}$$

yields,

$$\frac{N_A}{N_T} = \exp(-(k_b + k_c)t), \tag{2.16}$$

or

$$N_A = N_T \exp(-(k_b + k_c)t). \tag{2.17}$$

Integrating the rate law with respect to B ,

$$\int_0^{N_B} \frac{dN_B}{N_A} = \int_0^t (k_b)dt \tag{2.18}$$

gives

$$N_B = \frac{k_b}{k_b + k_c} N_T(1 - \exp(-(k_b + k_c)t)), \tag{2.19}$$

or

$$\frac{N_B}{N_T} = \frac{k_b}{k_b + k_c} - \frac{k_1}{k_b + k_c} \exp(-(k_b + k_c)t). \tag{2.20}$$

At infinite time, *i.e*, $t \to \infty$, eq. 2.20 becomes,

$$\frac{N_B}{N_T} = \frac{k_b}{k_b + k_c}. \tag{2.21}$$

Note that $\frac{N_B}{N_T}$ is the probability of having **B** products from the initial quantity of **A**, N_T. The rate constants $k_b + k_c$ can be related to the reaction time using the time required for N_T to reduce to $1/e$ its value, τ. Using eq. 2.16, it follows that for first order reaction,

$$(k_b + k_c)\tau = -\ln\left(\frac{N_T/e}{N_T}\right) = -\ln\frac{1}{e} = 1, \tag{2.22}$$

giving,

$$(k_b + k_c) = \frac{1}{\tau}. \tag{2.23}$$

τ is a measure of the decomposition time, hence, $(k_b + k_c)$ is equivalent to the overall rate, J, of the decomposition of **A**, while k_b and k_c is a measure of the rates of formation of **B** and **C** respectively. Therefore, eq. 2.21 can be rewritten as

$$\frac{N_B}{N_T} = P_B = \frac{J_B}{J}, \tag{2.24}$$

where P_B is the probability of having product **B**, J_B is the rate of formation of **B** and J is the rate of decomposition of **A**. Similarly, integration of eq. 2.13 will give

$$\frac{N_C}{N_T} = P_C = \frac{J_C}{J}. \tag{2.25}$$

Eqs. 2.24 and 2.25 are in agreement with the work of Sanders *et al.* [7] who, using the nucleation time for their derivation, stated that the rates in a competitive nucleation process were given by

$$J = \sum_i J_i, \tag{2.26}$$

and

$$J_i = P_i J, \tag{2.27}$$

where J_i is the rate of forming a given structure. For this work, i stands for the different phases nucleating, the sum in eq. 2.26 is over all possible phases and P_i is the probability of seeing the i^{th} phase in an ensemble of nucleation events.

As an independent check, the rate of nucleation is calculated using the survival probability (SP) of the metastable phase. This method, which has been used to study the rate of nucleation in gold nanoclusters[1, 3], evaluates the fraction of systems that have not nucleated after time t. Assuming first order kinetics for the nucleation process, the rate is obtain from [1],

$$\ln R(t) = -JV(t - t_0), \tag{2.28}$$

where $R(t)$ is the fraction of unnucleated sytems at a given time, t, V is the volume and t_0 is the lag time required to reach steady state. To evaluate $R(t)$, a Monte Carlo simulation of 2000 independent trajectories is carried out starting with configurations where the largest cluster contains only the impurity ($n_B \sim 0$, $n_C \sim 0$). For each starting configuration, a spin is randomly selected and flipped and the move is accepted with a probability $min\{1, exp(-\beta\Delta E)\}$. One Monte Carlo step (mcs) is equivalent to $N = L^2$ MC moves. The simulation is stopped when the largest cluster is greater than 60% of $N = L^2$. The nucleation time with units of mcs is measured as the time at which $n_B > n_B^*$ or $n_C > n_C^*$. Fig. 2.3 shows the size of n_B as function of time for twenty trajectories for the case where $H_B = H_C$. The size $n_B = 150$ is chosen as the size to determine the nucleation time, as 150 is well beyond the critical size of n_B or n_C.

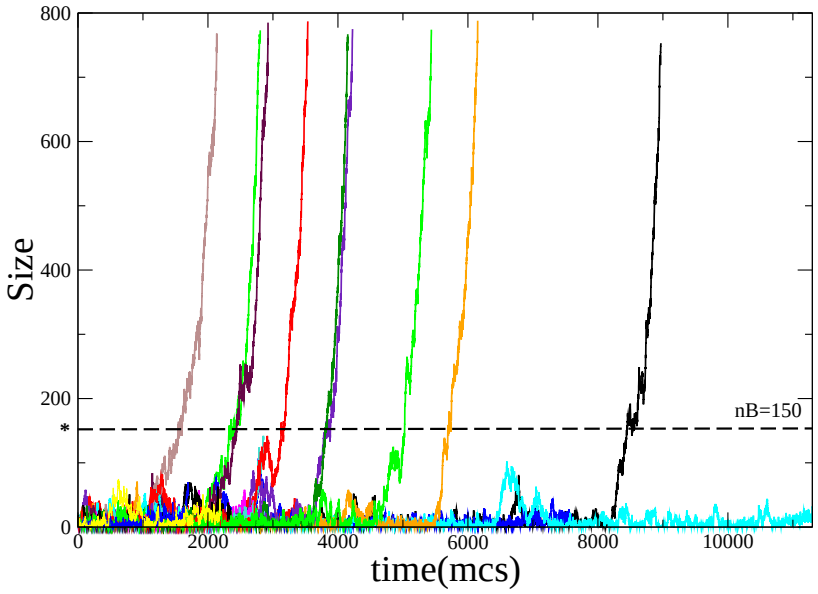

Figure 2.3: Plots of the size of component B in the largest cluster as a function of time (mcs) for twenty different trajectories. The dashed line $n_B = 150$ or $n_C = 150$ is used to determine the nucleation time. The trajectories with small sizes of component B have high C component where such trajectories stop.

Finally, the rate of nucleation is evaluated using the mean first passage time (MFPT), a method introduced into nucleation studies by Reguera *et al*[110]. The MFPT method has the advantages of ease of implementation, precise determination of critical size directly from kinetics and can also help to differentiate nucleation from growth. For each trajectory, the time, t, it takes to observe a maximum cluster of size $N = (n_B + n_C)$ for the first time is noted. The $MFPT$ as a function of size, $\tau(N)$, is the average of this time for size N over 500 different trajectories.

For a system where the barrier is high enough for the steepest descent approximation to be invoked, the MFPT expression is given as[110]

$$\tau(N) = \frac{\tau_J}{2}(1 + \mathrm{erf}((N - N^*)c)), \tag{2.29}$$

where τ_J is the nucleation time, $erf(N) = 2/\sqrt{\pi}\int_0^N \exp(-N^2)dN$ is an error function, N^* is the critical size while c is the local curvature about the top of the nucleation barrier. c is proportional to the Zeldovich factor, Z, as $c = \sqrt{\pi}Z$ [110]. Eq. 2.29 is fitted to the data obtained from simulation and the fit parameters, τ_J, N^* and c are obtained from this fit. The steady state nucleation rate is related to the nucleation time as,

$$J_{MFPT} = \frac{1}{\tau_J}. \tag{2.30}$$

2.3 Results

2.3.1 Free Energy Surfaces

The free energy surface calculated from $\Delta G(n_B, n_C)$ for $\beta H_B = \beta H_C = 0.12$ is shown in fig. 2.4. In a two dimensional free energy surface, the transition states between the metastable droplet and the spontaneous growth of the droplet occur along a boundary line of n_B^*, n_C^* embryos. However, fig. 2.4 shows that there are two free energy channels leaving the liquid state, one leading to the formation of B and the other leading to the formation of C. These channels are the most probable routes for the $A \rightarrow B$ and $A \rightarrow C$ transitions. The free energy barrier at the saddle point along the $A \rightarrow B$ channel is $\sim 8.0kT$ at the critical size of $n_B^* = 68$ ($n_C = 5$). It should be noted that at every point, both B and C components are present in a given cluster, but along the channel leaving the metastable state to B, n_C is approximately constant at $n_C \sim 5$. Similarly, for $A \rightarrow C$ transition, the critical size is

$n_C^* = 65$ ($n_B = 5$). The metastable region used to normalize the free energy is taken as the region where $n_B \leq 68$ and $n_C \leq 65$. It should noted that for equal fields, the embryo size used to define the metastable region is expected to be equal. However, the values used here were obtained from a quadratic fits and the difference in $\Delta G(n_B, n_C)$ at this sizes is less than $0.2k_BT$. Another definition of the metastable region where,

$$\frac{n_B^2}{n_B^* 2} + \frac{n_C^2}{n_C^* 2} - 1 \leq 0. \tag{2.31}$$

The difference between $\Delta G(n_B, n_C)$ from these two different definitions is less than $\sim 0.1k_BT$. The summary for the free energy surface is contained in Table 2.2. Table 2.2 also contains data from the free energy surfaces calculated for all the other conditions considered. When $\beta H_C > \beta H_B$, the free energy barrier along $A \rightarrow C$ is lower than that of $A \rightarrow B$. There is also a reduction in the critical size, n_C^* (see Fig. 2.5). When partial mixing is allowed for the unequal fields, by using $\mathbf{J}_{B,C} = -0.8$, the entire free energy surface becomes lower with corresponding reductions in ΔG_B^* and ΔG_C^*, as seen in Fig. 2.6. An increase in $\mathbf{J}_{B,C}$ allows for mixing, which has a similar effect as that of lowering the surface tension in the work of formation. This mixing also causes an increase in the entropy of mixing which causes a reduction in ΔG. All the free energy surfaces show that there is only one barrier leading to each of the stable phases. This is consistent with the method used to evaluate the rates to each of the phases by way of TST.

Conditions	βH_B	βH_C	n_B^*	n_C^*	ΔG_B^*	ΔG_C^*
1: Equal fields, no mixing	0.12	0.12	68	65	8.095	8.186
2: Unequal fields, no mixing	0.12	0.17	69	47	9.876	8.021
3: Unequal fields, partial mixing	0.12	0.17	58	40	7.944	6.233

Table 2.2: Summary of critical sizes and free energy barriers for different conditions at which the simulation was performed.

The free energy energy for heterogeneous nucleation calculated by Scheifele *et al*[81] showed that for impurity of length $l \geq 3$, there is a marked wetting of the impurity by the stable phase prior to the crossing of the free energy barrier, which is indicated by the minimum in the free energy plot (cf Figure 3b[81]). This feature is absent from the free energy surfaces above. To test the absence of wetting phenomena in this model, the probability of

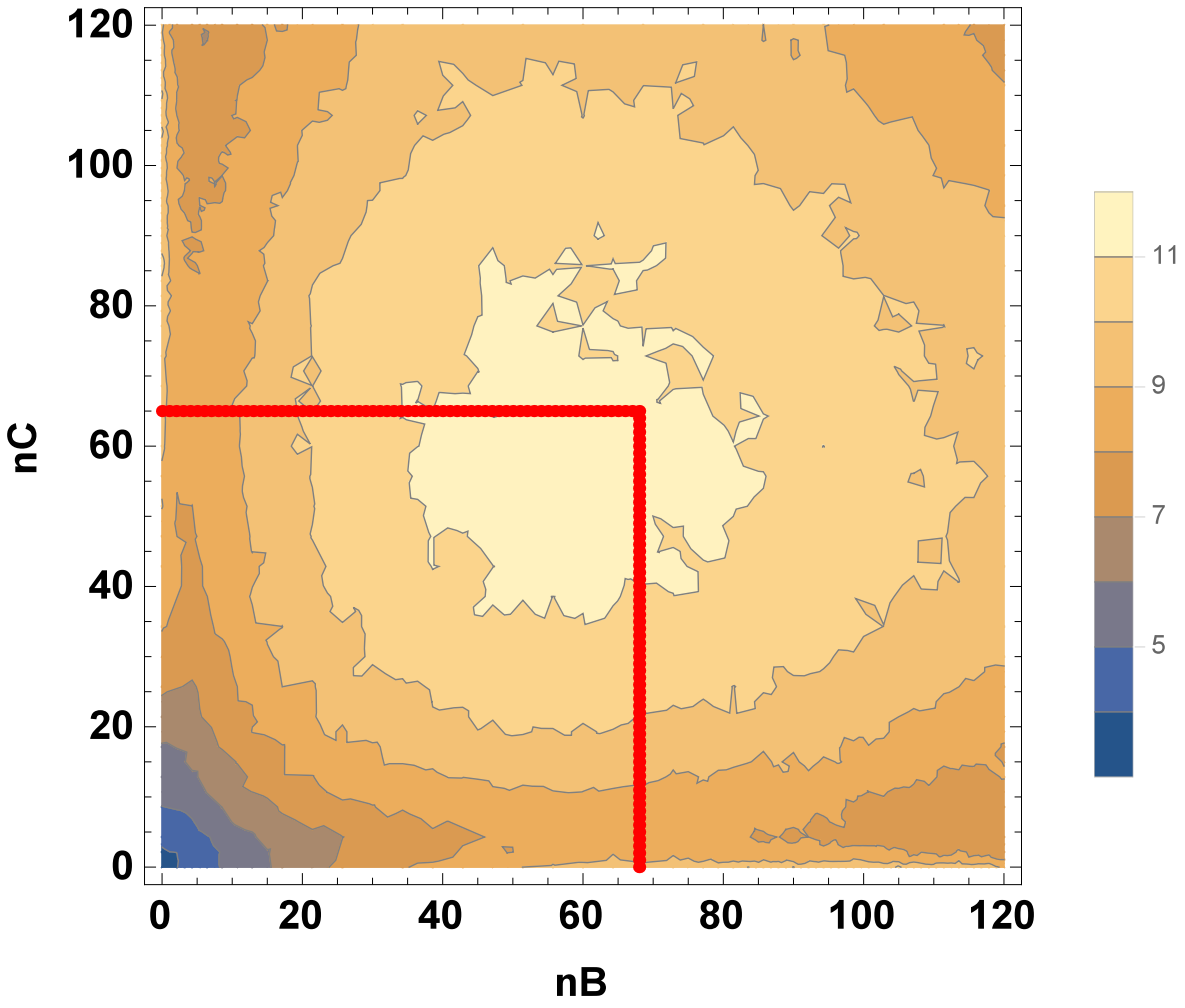

Figure 2.4: Free energy surface, $\Delta G(n_B, n_C)$ for nucleation of phases B and C from a metastable phase on an heterogeneity of length $l = 7$ for the case where $\beta H_B = \beta H_C = 0.12$. The region below the red dots indicates the metastable region.

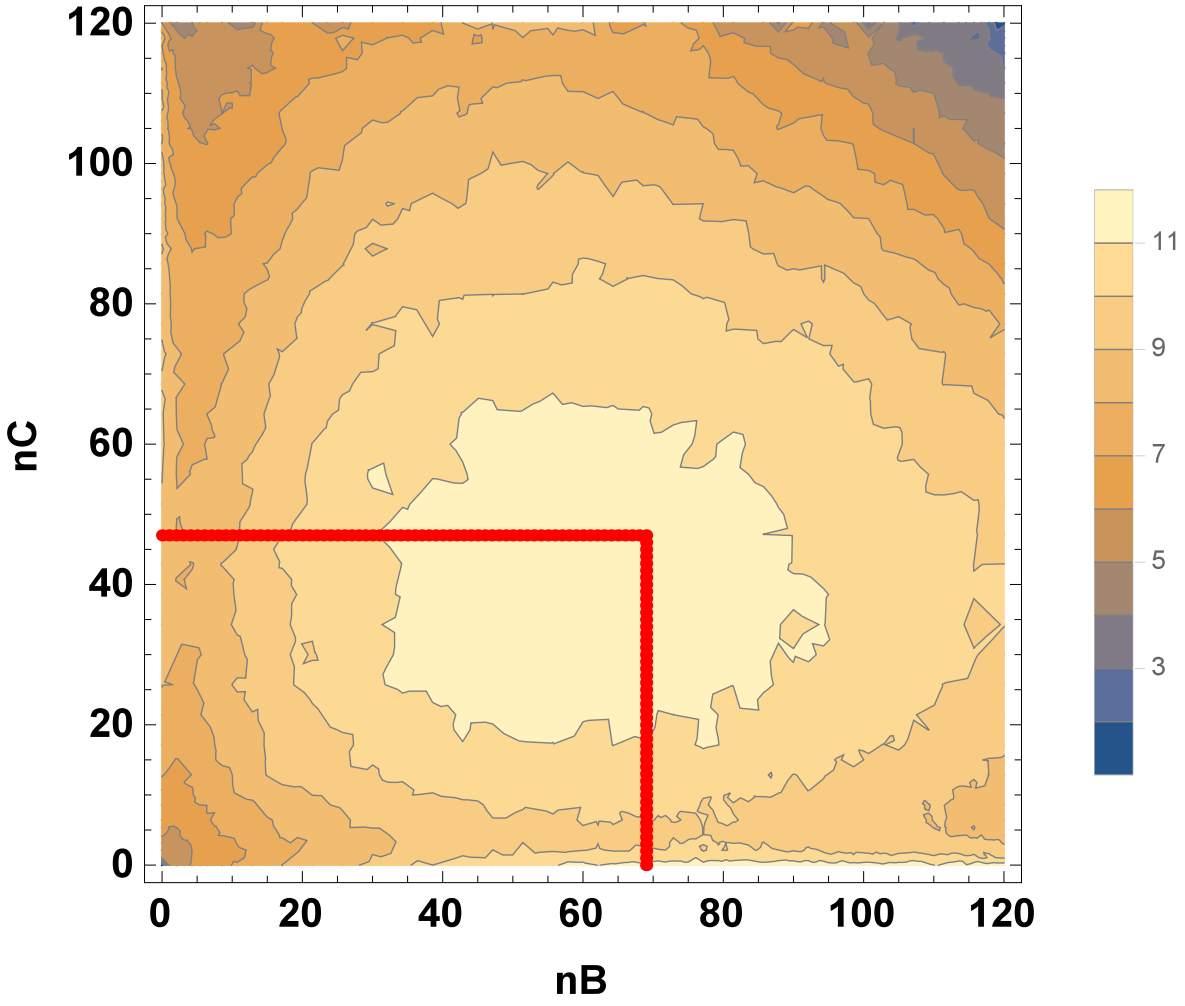

Figure 2.5: Free energy surface, $\Delta G(n_B, n_C)$ for nucleation of phases B and C from a metastable phase on an heterogeneity of length $l = 7$ for *case* **2** where $\beta H_B = 0.12$ and $\beta H_C = 0.17$. The region below the red dots indicates the metastable region.

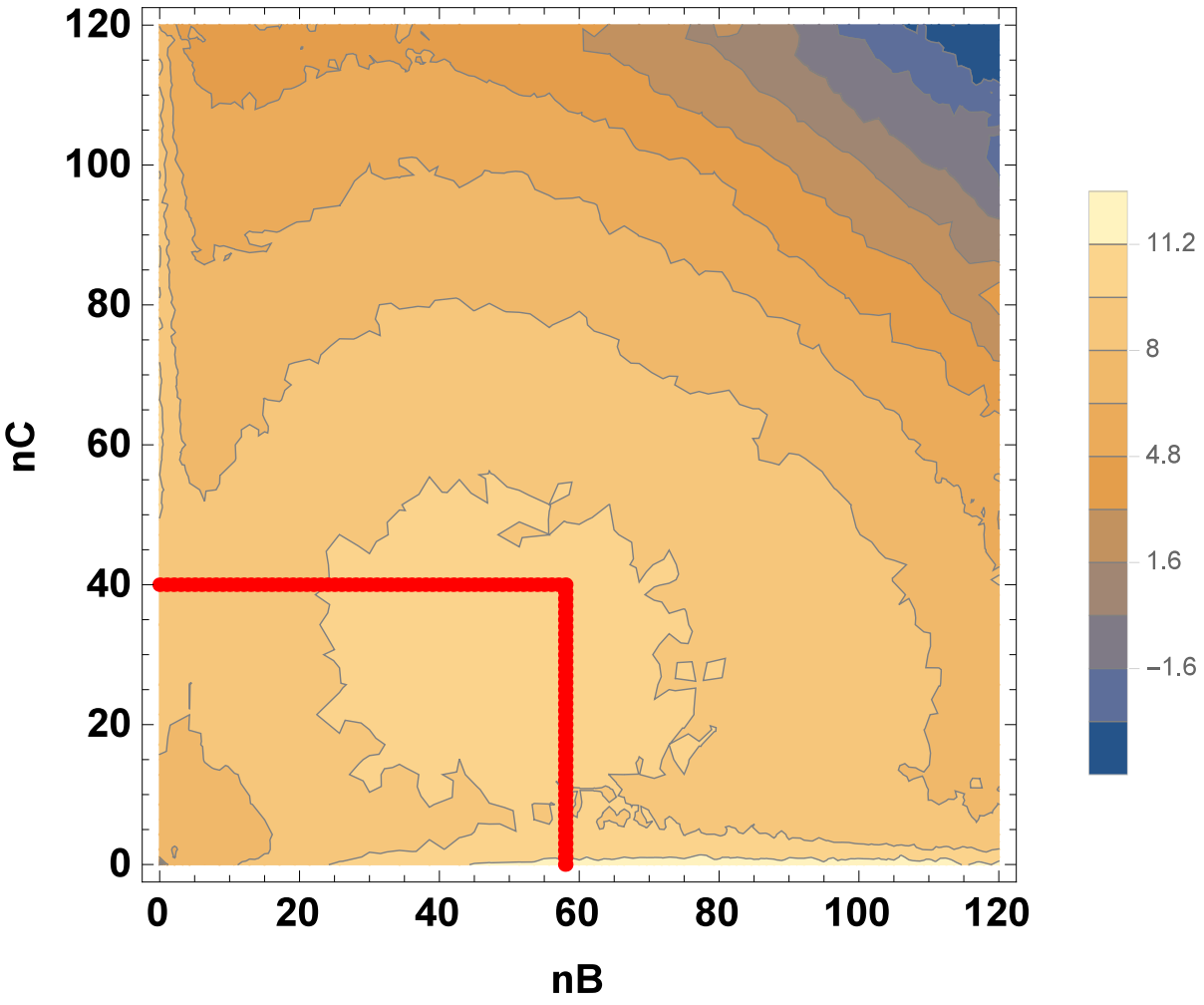

Figure 2.6: Free energy surface, $\Delta G(n_B, n_C)$ for nucleation of phases B and C from a metastable phase on an heterogeneity of length $l = 7$ for *case* **3** where $\beta H_B = 0.12$ and $\beta H_C = 0.17$ and $J_{B,C} = -0.8$. The region below the red dots indicates the metastable region.

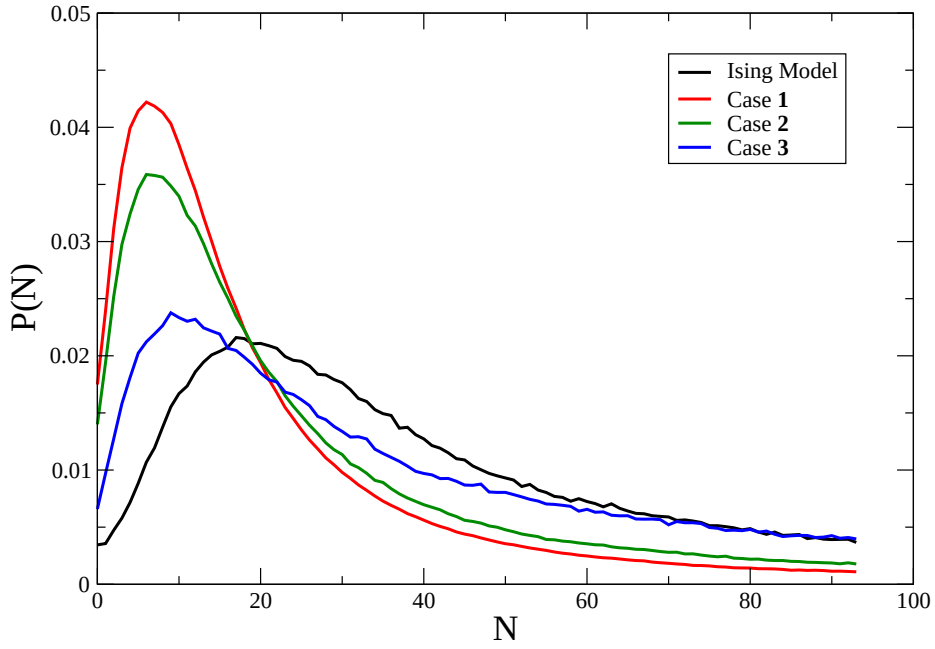

Figure 2.7: Probabilities of N-sized cluster on the heterogeneity for Potts model with $q = 3$ and $q = 2$ (Ising model). For the case when $q = 3$, $N = n_B + n_C$.

having a given cluster size around the impurity is evaluated. For the different cases studied, the total size of the cluster is evaluated as $N = n_B + n_C$ for the Potts model, while N for a test Ising model is the size of the cluster on the heterogeneity. The probability of having a given size, $P(N)$, is calculated for $N \leq 100$ for a given trajectory. The average of $P(N)$ is taken for 100 independent trajectories. Fig. 2.7 shows the $P(N)$ for a heterogeneous Ising model ($q = 2$) and $P(n_B + n_C)$ for the different cases where the free energy surfaces were calculated. A maximum in P(N) represents a local minimum in the free energy. $P(N)$ for $q = 2$ shows that there is wetting at $N \approx 18$, meaning that the impurity is surrounded by at least a layer of the stable phase. For the Pott's model ($q = 3$), there is partial wetting for cases 1 and 2 at about $N(n_B + n_C) \approx 5$. The reduction in the degree of wetting results from the competition between the spins from the different stable phases since they dislike each other. An increase in the field strength reduces the probability, but does not increase the size of the wetting cluster or layer, but with $\beta J_{B,C}$ increased to -0.8, the level of wetting

increases to $N(n_B + n_C) \approx 9$. This is due to an increase in mixing which allow spins B and C to sit next to each other on the impurity. It is expected that as $J_{B,C}$ increases, complete wetting of the heterogeneity will eventually occur.

2.3.2 Transition State Theory

To calculate the rate, $J_{B_{TST}}$, as given in eq. 2.8 using the ΔG_B^* obtained, the values of f_B^+ and z_B are first evaluated. As an example, fig. 2.8 shows a plot of the mean square fluctuation $< \Delta n_B^2(t) >$ at $\beta H_B = 0.12$. The linear fit gives the slope from where $f_B^+ = 11.74\ mcs^{-1}$ is obtained. f_B^+ for other conditions and all f_C^+'s are obtained in a similar way. Fig. 2.9 shows plots of $\Delta G(n_B, n_C)$ close to ΔG_B^* with quadratic fits for different values of n_C. The value of n_C is held constant along the free energy channel while $\Delta G(n_B, n_C)$ within $0.2kT$ of ΔG_B^* is plotted. The second derivative of the quadratic fit gives $\eta_B = -(\delta^2 G/\delta n_B^2)_{n=n_B^*}$ which is used to obtained z_B. Another quantity needed to calculate $J_{B_{TST}}$ from eq. 2.8 is $exp(-\Delta G(n_B^*, n_C))$. From the free energy surface, it can be seen that there is no single point on the free energy surface that represents the critical cluster. Instead there is a saddle point region that the cluster moves through. For all the $\Delta G(n_B^*, n_C)$,

$$\exp(-\Delta G(n_B^*, n_C)) = P(n_B^*, n_C), \tag{2.32}$$

where $P(n_B^*, n_C)$ is the probability of having critical size n_B^*. At the critical size, n_B^*, the cluster can pass through any point where $\Delta G(n_B^*, n_C)$ is very close to the minimum value. This means that

$$\sum \exp(-\Delta G(n_B^*, n_C)) = P(n_B^*, 1) + P(n_B^*, 2) + P(n_B^*, 3).....P(n_B^*, i), \tag{2.33}$$

provided $\Delta G(n_B^*, n_C)$ is within $1.0kT$ of the minimum values which is regarded as ΔG_B^* shown in Table 2.2. Table 2.3 shows the summary of kinetic factors, f_B^+, f_C^+, z_B and z_C, $\sum \exp(-\Delta G(n_B^*, n_C)), \sum \exp(-\Delta G(n_B, n_C^*))$ and the rates for the different transitions.

Conditions	f_B^+	f_C^+	z_B	z_C	$\sum \exp(-\Delta G_B^*)$	$\sum \exp(\Delta G_C^*)$	$J_{B_{TST}}(\times 10^{-4})$	$J_{C_{TST}}(\times 10^{-4})$
Case **1**	11.74	13.60	0.00987	0.00886	1.26×10^{-3}	1.18×10^{-3}	1.46 ± 0.18	1.43 ± 0.18
Case **2**	19.31	18.03	0.00942	0.00803	8.68×10^{-4}	4.76×10^{-3}	1.57 ± 0.21	6.90 ± 0.24
Case **3**	8.96	10.91	0.01078	0.00985	4.21×10^{-3}	1.74×10^{-2}	4.07 ± 0.24	18.49 ± 0.20

Table 2.3: Summary of the different factors and free energy barriers used to calculate the rates for the different conditions.

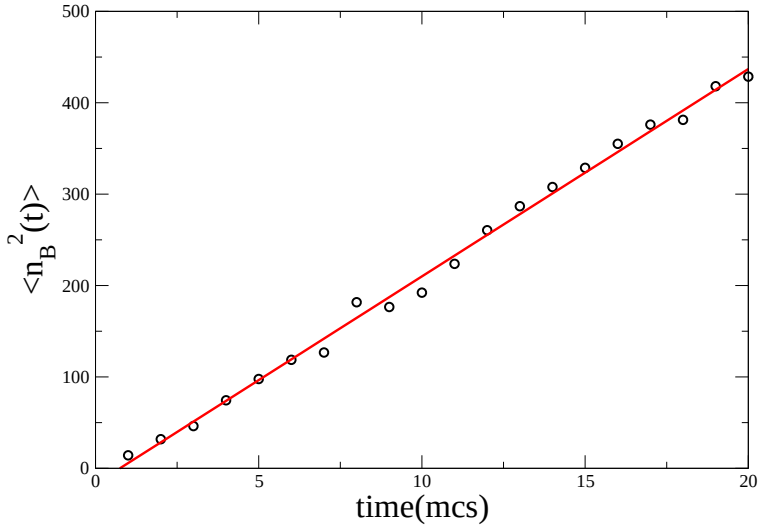

Figure 2.8: The fluctuation of size, $< \Delta n_B^2(t) >$, for component **B** as as a function of time.

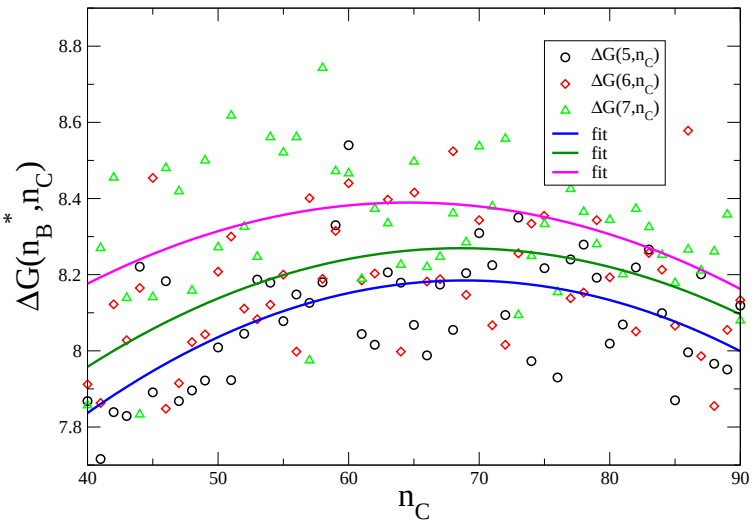

Figure 2.9: Plots of ΔG_B^* at $n_C = 5, 6, 7$ and the quadratic fits to them, which are used to obtain the curvature of the free energy surface, η_B.

Fig. 2.10 is a plot of the rates to each of the phases and the overall rates for the three cases studied. When $\beta H_B = \beta H_C$, the rates are approximately equal to each other. When βH_C is increased, $J_{C_{TST}}$ increased significantly while $J_{B_{TST}}$ remained constant. The increase in $J_{C_{TST}}$ corresponds to the decrease in free energy barrier to phase **C**. When partial mixing is allowed, both $J_{B_{TST}}$ and $J_{C_{TST}}$ increase, but the increase in $J_{C_{TST}}$ is more than $J_{B_{TST}}$. The overall rate increase steadily from *case* **1** through *case* **2** to *case* **3**.

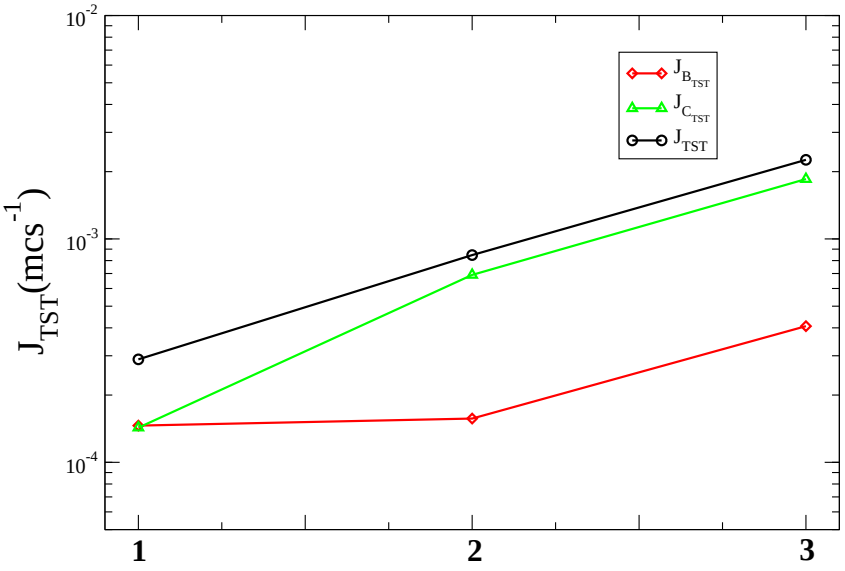

Figure 2.10: Plots of the rates $J_{B_{TST}}$ and $J_{C_{TST}}$ compared to the overall rates, J_{TST}, at conditions defined for the free energy calculations.

2.3.3 Survival Probability

Fig. 2.11 shows plots of $\ln R(t)$ versus t, where $R(t)$ is the fraction of unnucleated systems for the different cases. The plots are linear, confirming a first order process, and the slope equals $-JV$. In a bulk, uniform system, the volume term in eq. 2.28 arises because the nucleation event can occur anywhere with equal probability, thus it accounts for the translational degrees of freedom of the nucleating embryo. The Potts model used here is a 2-dimensional lattice model nucleating on an impurity. The external field strength used ensures that there is only

one cluster in the system containing the impurity. As a result, $V = 1$ is used and the rate is reported in units of the number of clusters per unit time. Hence, the slope equals the overall rate at which the system leaves the metastable phase to the stable phases. Fig. 2.11 also shows the $\ln R(t)$ versus t plot for heterogeneous nucleation of Ising model ($q = 2$).

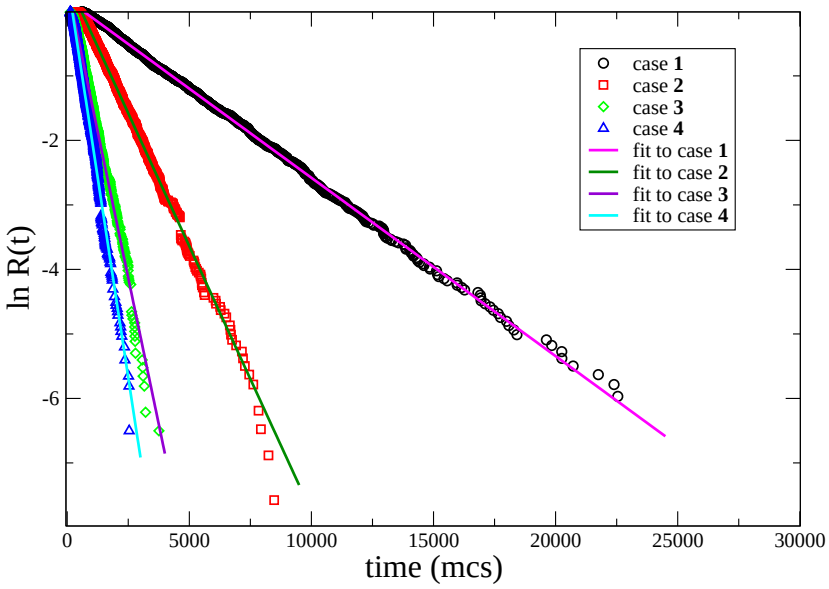

Figure 2.11: Plots of $ln\ R(t)$ versus MC steps with the slope representing $-JV$ for different cases listed in Table 3.1 showing the linear fits to the simulation data.

In order to obtain the individual rates, the probabilities of seeing a given phase from an ensemble of nucleation events are evaluated. P_B is the probability of seeing phase **B** and it is calculated as the ratio of the number of trajectories ending in **B** to the total number of trajectories. Table 2.4 contains P_B and P_C, the overall rates and the individual rates to the different phases for the three conditions studied. When $\beta H_B = \beta H_C$, $P_B \sim P_C$, but P_B is reduced significantly when $\beta H_C = 0.17$ due to the reduction in ΔG_C^*, allowing most of the trajectories to end in **C**. The individual rates are obtained from the overall rate using eq. 2.27. Fig. 2.12 is a plot of $J_{B_{SP}}$ and $J_{C_{SP}}$, and the overall rates for the three cases studied using eq. 2.28. The increase in $J_{C_{SP}}$ corresponds to the decrease in ΔG_C^* due to the increase in βH_C in case **2** and mixing in case **3**. The validity of obtaining the $J_{B_{SP}}$ and $J_{C_{SP}}$ using

this method has been shown in the earlier work by Sanders *et al* [7] who tested their results with those obtained using the forward-flux sampling method [113].

Conditions	P_B	P_C	J_{SP}	$J_{B_{SP}}$	$J_{C_{SP}}$
Case **1**	0.482	0.518	0.000277	0.000134	0.000144
Case **2**	0.123	0.877	0.000824	0.000101	0.000722
Case **3**	0.189	0.811	0.001786	0.000338	0.001448

Table 2.4: The probabilities of seeing different phases, the overall rates obtained from the slopes in fig. 2.11 and the individual rates for the different conditions.

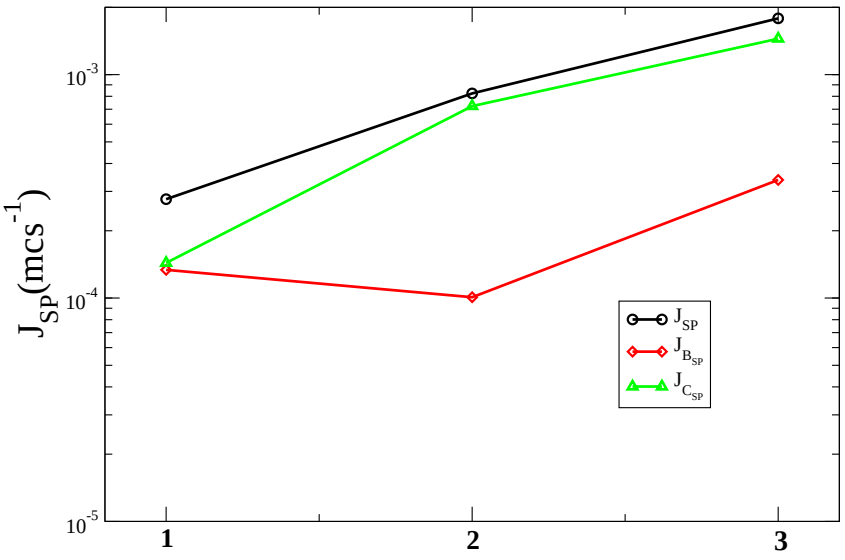

Figure 2.12: Plots of the rates $J_{B_{SP}}$ and $J_{C_{SP}}$ compared to the overall rates at conditions defined for the free energy calculations.

2.3.4 Mean First Passage Time

Fig. 2.13 is a plot of mean first passage time as a function of cluster size, $\tau(N)$, obtained from simulations and the corresponding fits to eq. 2.29, for the different conditions which were studied. For all the cases, $\tau(N)$ reaches a good plateau showing that nucleation and

growth are not coupled together. As can been seen from fig. 2.13, the fits are reasonably good especially around the inflection point for cases 1 and 2. Table 2.5 is a summary of the parameters obtained by fitting the simulation data to eq. 2.29, the overall rates and the rates of formation of the phases. Despite the good fits around the inflection point, the fit parameter N^* cannot be described as the critical size. This is based on the fact that $\tau(N)$ follows the combination of $N = n_B + n_C$, and sometimes $n_B + n_C = N^*$ is not necessarily on the transition path, thereby giving N^* the probability of transition less than 50% . Most importantly, N^* contains no information on the contribution from each of the two phases, as such, N^* does not indicate which phase it would likely form without visual inspection of the configuration. Similarly, c from the fit may not be a true measure of the curvature at the top of the nucleation barrier since the MFPT is not restricted to a particular transition. Despite these short comings of fitting eq. 2.29 into the simulation data, the nucleation times, τ_J, obtained from the fit is equivalent to the value of the MFPT along the plateau region. From the value of τ_J and using eq. 2.30, the overall rate of nucleation is obtained.

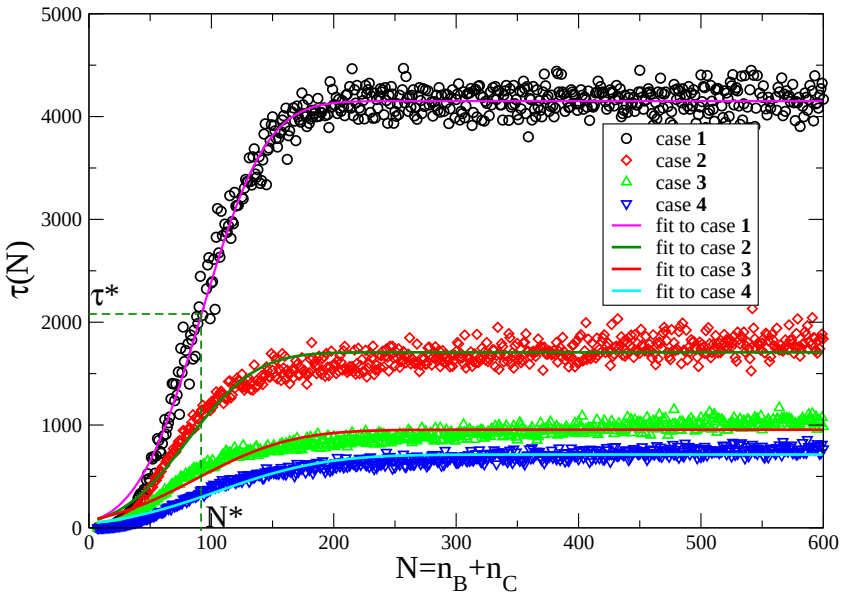

Figure 2.13: MFPT from simulations for the different cases studied.

Conditions	τ_J	N^*	c	J_{MFPT}	$J_{B_{MFPT}}$	$J_{C_{MFPT}}$
Case **1**	4150.23	91.88	0.0177	0.000241	0.000116	0.000125
Case **2**	1680.11	80.81	0.0161	0.0005952	0.000073	0.000523
Case **3**	796.81	87.72	0.0115	0.001255	0.000237	0.001018
Case **4**	712.74	105.55	0.0103	0.00140	-	-

Table 2.5: Fit parameters from fitting eq. 2.3.4, the overall nucleation rates and the individual rates for the different conditions using the MFPT method.

2.4 Discussions

For the different methods used to calculate the rates of nucleation, J_B remains almost unchanged as βH_C is increased from 0.12 to 0.17, but J_C has increased significantly. With the mixing parameter increased to -0.80, both J_B and J_C increase as a result of the lower free energy barrier to phases B and C. In all the cases studied, J_B and J_C are lower than J obtained for heterogeneous Ising model ($q = 2$) with the same conditions. This is due to two possible factors. The phase space of the metastable state becomes larger and therefore it takes a longer time to sample when there are two or more phases involved. Another possibility is the competition between the phases. Since the spins dislike each other and therefore don't like sitting next to each other, the competition to occupy sites on the heterogeneity delays the nucleation of any of the phases. This competition also reduces the degree of wetting of the impurity. As the ability of the phases to mix increases, more wetting occurs, causing a reduction in the free energy barrier, hence a faster rate.

Fig. 2.14 provides a complete summary of the overall rate of leaving the metastable state, obtained using the three different methods, for all the conditions studied. Fig. 2.14 also contains the rate, J^0_{TST}, which is obtained using the transition state theory, but the ΔG^*_B and ΔG^*_C in eqs. 2.8 and 2.9 are not re-normalized. The rates are highest when 20% mixing is allowed. This is consistent with the reduced free energy barriers to phases B and C. The rate is lowest when $\beta H_B = \beta H_C$, which corresponds to equal free energy barriers. When the fields are unequal, without mixing, the increase in the overall rate is a result of the lowering of ΔG^*_C.

Comparing the overall rates of nucleation, J_{TST} are within the errors of J_{SP} for all the

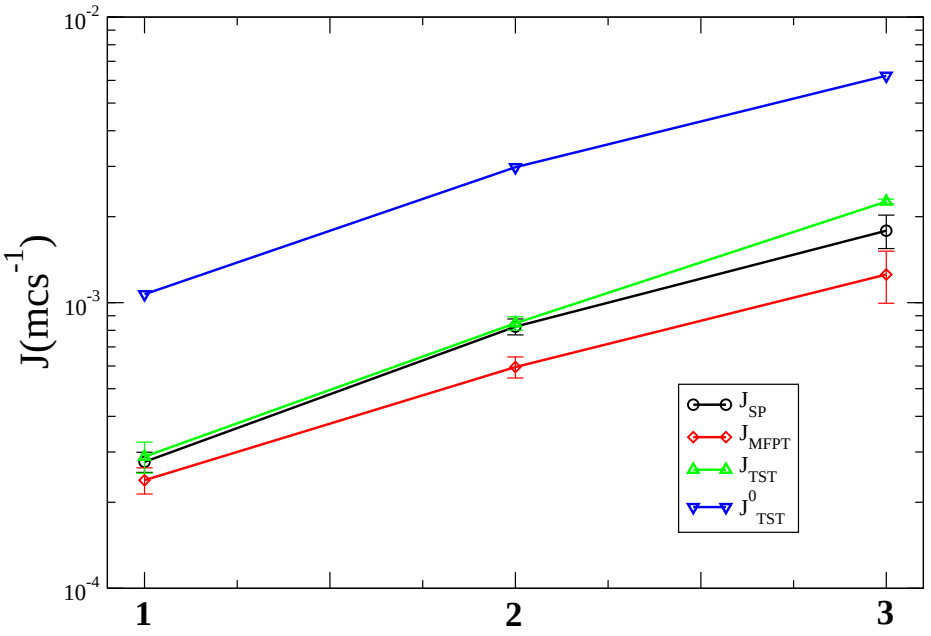

Figure 2.14: Comparison of the rates of exiting the metastable phase, $J_{TST}, J_{SP}, J_{MFPT}$ for different conditions.

cases studied. J_{MFPT} underestimate both J_{TST} and J_{SP} though they are within error of each other. J^0_{TST} overestimate J_{SP} and J_{MFPT} as shown in fig. 2.14. The result using the TST reproduces those obtained from the other two methods within reasonable error, which seems to confirm the initial findings of Scheifele[81], who showed that re-normalizing the free energy surface with the probability of the metastable state gives a more accurate rate using the transition state theory. Though shown earlier for heterogeneous nucleation of single component[81], the need to re-normalize the free energy surface with the metastable state as a reference can be applicable to competitive nucleation. Though the components do not like sitting next each other, there is no evidence of a formation of a homogeneous cluster elsewhere; all the clusters contain the impurity. Aside from the size of the system, which allows for only one cluster containing the heterogeneity, the interaction between the heterogeneity ensures that phases always form on the heterogeneity which is consistent with the observations of Sears *et al*[85], where the phase with high interactions with the impurity

nucleates on it. All these ensure that the transition is from the metastable phase to a stable phase containing the heterogeneity.

Scheifele *et al*[81] showed that the three methods they used to calculate the rates gave the same result for heterogeneous nucleation in the low barrier regime in the Ising model. Two of the three methods used here are the same with those of Scheifele *et al*[81], and J_{TST} is able to reproduce J_{SP} when the saddle point approximation is applied. In the Potts model, the free energy surface is three dimensional with the nucleating cluster being described by two variables, unlike the case of the Ising model. This means that there is no longer a single point on the free energy surface that represents the critical cluster. Instead there is a saddle point region that the cluster moves through. As a result, it is necessary to account for transitions moving through the transition region near the saddle point where $\Delta G(n_B^*, n_C)$ is within $1.0kT$ of ΔG_B^*. As the free energy barrier becomes lower, these transition regions widens, more points fall within $1.0kT$ thereby increasing $\sum exp(-\Delta G(n_B^*, n_C))$, hence a more accurate J_{TST} in *case* **3**.

The critical size obtained from the fit to the MFPT does not define the transition state as it has no information on which phase it is going to. Also, parameter c is not a representation of the curvature and therefore cannot be used to estimate the Zeldovich factor. These two are important kinetic parameters and given the type of model used here, a Fokker-Planck equation[114] as a function of two parameters should be solved. This, I suggest will give a MFPT, $\tau(n_B, n_C)$ where n_B^* and n_C^* can be obtained directly as fit parameters.

2.5 Conclusions

This chapter examines the competitive nucleation between different phases forming on a nanoscale heterogeneity. The free energy surfaces for nucleation at different external field strength and different interaction parameters are calculated using Monte Carlo simulations. The free energy barriers are used to calculate the overall rates of nucleation and the rates to each of the phases using three different methods. The results show that normalizing the free energy surfaces with respect to the metastable state is important in obtaining accurate rates from TST method, and these rates compare to the rates obtained from other methods. Unlike a single component nucleating on the heterogeneity, the competition between the different components increases the nucleation time, leading to lower rates of nucleation. The rate is

lowest when the two phases have equal external field strength. When the field strength of one phase increases, the overall rate increases due to the lowering of the free energy barrier to that phase. The rate increases when the interaction parameter increases, due to the reduction of the free energy barrier caused by an increase in the entropy of mixing.

Chapter 3

Reaction Coordinates for Competitive Phase Transition

3.1 Introduction

A reaction coordinate is a single variable, or combination of variables that describes the progression of a process from its initial state to its final state. In CNT, the cluster size is usually used to describe the reaction progress, with the critical size describing the transition state from metastable to stable phase. However, despite the fact that the cluster criteria used to identify the growing embryo contains information regarding cluster structure, there is growing evidence to suggest that a more explicit description of the reaction coordinate may provide useful information about the mechanisms of nucleation.

For example, recent studies have used transition path sampling to show that the surface area of an embryo can be an important variable describing the transition state[11, 12, 17]. These suggest that both small compact embryos and large diffuse embryo can be critical. The primary approach for these studies is to test different order parameters or their combination as the best reaction coordinate using the maximum likelihood[12, 18] or genetic neural network analyses [19]. These studies only considered systems where a metastable phase undergoes a transition to a single stable phase. However, molecular dynamic simulations of freezing in nanoparticles show that under the same conditions, clusters will freeze to different structures[1, 2, 3]. Also, the generalized Potts model[83, 84] has been used to model systems that can have two or more product phases[7]. These suggest that different order parameters are responsible for the different structures, hence, each of the products has a unique reaction coordinate.

In this chapter, the aimless shooting method of transition path sampling is extended to the study of competitive nucleation, where multiple transitions may occur. The multiple

path maximum likelihood expression is developed in order to maximize the probabilities of a configuration being on a certain transition path. The developed multiple path maximum likelihood analysis (MPMLA) is applied to the Potts model undergoing heterogeneous nucleation which was studied in Chapter 2.

3.2 Theoretical Overview

3.2.1 Transition Path Sampling

In order to study the dynamics of freezing in nanoparticles without any bias towards a particular reaction coordinate, numerous trajectories are required. These trajectories must be obtained with no previous knowledge or reference to a particular reaction coordinate. Nucleation is a rare event, as such, obtaining these trajectories is ordinarily a difficult task. To overcome this difficulty, transition path sampling (TPS) [115, 94, 87] is used to sample only the reactive trajectories. The trajectories are said to be reactive when they connect the initial and the final states together, *i.e* when the forward trajectory ends in the product and backward trajectory ends in the reactant or *vice versa*. For a system with a single initial state (reactant A) and a single product, B, the transition path ensemble (TPE) is the weighted set of all the reactive trajectories [94]. Mathematically, the TPE can be given as [93]

$$P_{AB}[\mathbf{x}(L)] \equiv Z_{AB}^{-1} h_A(\mathbf{x}_0) P[\mathbf{x}(L)] h_B(\mathrm{x}_L) \tag{3.1}$$

where Z_{AB} is a normalization factor, while h_A and h_B are signature functions defining the states A and B, such that their values are unity if the configuration x is within the reactant or product regions, and zero otherwise. $P[x(L)]$ is the dynamical path probability for a path $\mathbf{x}(L) = \{\mathbf{x}_0, \mathbf{x}_{\Delta t}, ..., \mathbf{x}_{L\Delta t}\}$, L is the integer number of points where the configuration is harvested. The major advantage of TPS is that it does not require *a priori* information on the mechanism [116]. It also increases sampling efficiency by focusing mainly on the rare but reactive trajectories [12].

3.2.2 Multiple States Transition Path Sampling

The TPS as explained in the previous subsection is very efficient when used for processes with only two distinct stable states[12, 18, 19]. However, many systems are of a complex nature.

For example, a single reactant may give two or more products. Fig. 3.1a shows a process where two products evolve directly from a single initial state. There may also be an interconversion between the products as shown in fig. 3.1b. For these types of systems, the simple TPS will not be efficient. To study such processes, the multiple state TPS (MSTPS)[21, 117] is used, where the transition path ensemble is define as a weighted set of all trajectories connecting any two stable states,

$$P_{MSTPS}[\mathbf{x}(L)] \equiv \sum_{i,j\neq i} Z^{-1} \prod_k \bar{h}_k[\mathbf{x}(L)] h_i(\mathbf{x}_0) P[\mathbf{x}(L)] h_j(\mathbf{x}_L). \tag{3.2}$$

Here, Z is the normalization factor

$$Z \equiv \int D\mathbf{x}(L) P[\mathbf{x}(L)] \prod_k \bar{h}_k[\mathbf{x}(L)] \sum_{i,j\neq i} h_i(\mathbf{x}_0) h_j(\mathbf{x}_L), \tag{3.3}$$

where $\bar{h}_k[\mathbf{x}(L)]$ is ensures that only the start and end of the path are in the stable basins. The notation,

$$\int D\mathbf{x}(L) \equiv \int ... \int dx_0 dx_{\Delta t} dx_{2\Delta t} ... dx_{L\Delta t} \tag{3.4}$$

implies an integration over all time slices $L\Delta t$. The different h functions define the stable state regions, which ensures that only the end points enter as stable state. h is expressed as

$$h_i(\mathbf{x}) = \begin{cases} 1, & \text{if } \mathbf{x} \in \mathbf{i} \\ 0, & \text{otherwise.} \end{cases}$$

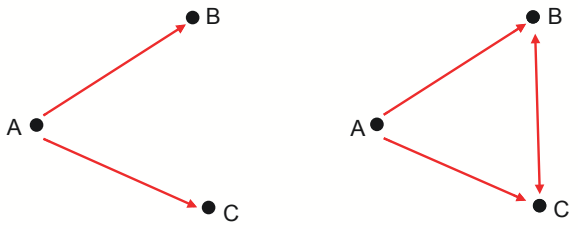

Figure 3.1: Schematic diagram showing possible transitions. (a) Transition only from the metastable phase to the phases B and C. (b) Possible transition between phases B and C in addition to $A \rightarrow B$ and $A \rightarrow C$ transitions.

The full transition path ensemble, which is given as,

$$TPE = \sum_{i,j\neq i} h_i[\mathbf{x}^n_{-t/2}]h_j[\mathbf{x}^n_{t/2}] + h_i[\mathbf{x}^n_{t/2}]h_j[\mathbf{x}^n_{-t/2}], \tag{3.5}$$

consists of all the configuration that have been accepted as being on a transition path.

3.2.3 Multiple Paths Maximum Likelihood Analysis

In a two state transition, ($\mathbf{A} \rightarrow \mathbf{x}$), the exact reaction coordinate is the *committor probability* ($p_B(\mathbf{B})$)[19, 118], also referred to as the *committor*. The committor probability is the fraction of trajectories committing to the final product ($\mathbf{B}$) from a given configuration ($\mathbf{x}$) initiated with Boltzmann distributed velocities[119, 115]. An alternative and computationally less expensive way of obtaining the reaction coordinate is through the transition path probability, $p(TP|\mathbf{x})$[12, 120]. This is the probability that trajectories from $\mathbf{x}$ lie on the transition path $\mathbf{A} \rightarrow \mathbf{B}$. Hummer[120] showed that for a diffusive barrier crossing, as found in nucleation processes,

$$p(TP|\mathbf{x}) = 2p_B(\mathbf{x})(1 - p_B(\mathbf{x})) \tag{3.6}$$

such that at $p_B(\mathbf{x}) = 0.5$, $p(TP|\mathbf{x})$ is maximum.

For a transition to two different products (3.1a) with or without the possibility of interconversion among the products, there are more than one reaction path. The transition paths are independent and trajectories initiated from configuration $\mathbf{x}$ can lie on any of the transition paths. Considering a general case of m phases, the transition path probabilities obey the additive law

$$\sum_{i,j}^{m} p_{ij}(TP|\mathbf{x}) = 1. \tag{3.7}$$

Here $p_{ij}(TP|\mathbf{x}) = p_i(\bar{\mathbf{x}})p_j(\mathbf{x}) + p_j(\bar{\mathbf{x}})p_i(\mathbf{x})$, $p_i(\mathbf{x})$ is the probability that the forward trajectories commits to i and $p_i(\bar{\mathbf{x}})$ is the probability that backward trajectory commits to i. The summation eq. 3.7 in all $p_{ii}(TP|\mathbf{x})$ signifying configurations not on any transition path. For the scenario in fig 3.1a,

$$p_{AB}(TP|\mathbf{x}) = 2p_B(\mathbf{x})(1 - p_B(\mathbf{x}) - p_C(\mathbf{x})) \tag{3.8}$$

$$p_{AC}(TP|\mathbf{x}) = 2p_B(\mathbf{x})(1 - p_B(\mathbf{x}) - p_C(\mathbf{x})) \tag{3.9}$$

where the relation, $p_A(\mathbf{x}) = 1 - p_B(\mathbf{x}) - p_C(\mathbf{x})$ has been used. Fig. 3.2 shows the transition path probabilities from eqs. 3.8 and 3.9 for an arbitrary reaction coordinate $r(\mathbf{x})$. The

committor probabilities, p_B and p_C, are obtained from model functions that have the ideal characteristics as shown in the inset. For a good reaction coordinate $r(\mathbf{x})$, the function $p(TP|r)$ has a peak at r^* indicating the transition state, $r(\mathbf{x}) = r^*$[120]. To obtain a good reaction coordinate from these transition path probabilities, the maximum likelihood analysis is applied to these probabilities.

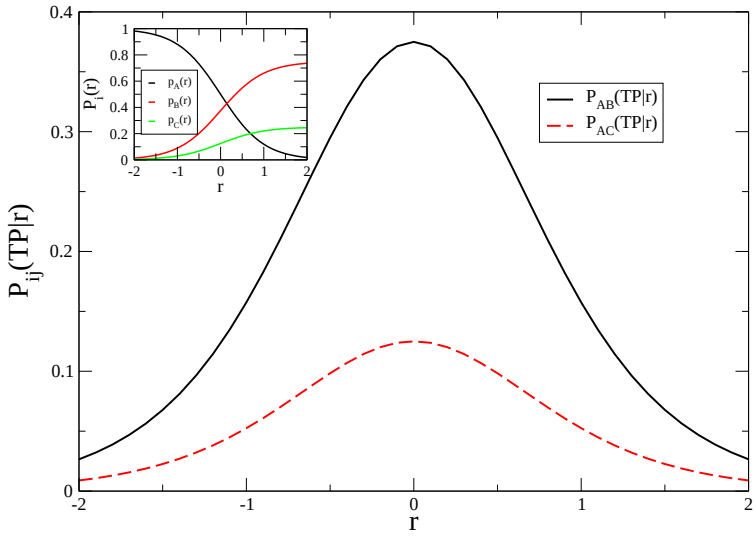

Figure 3.2: Plot of transition path probabilities as a function the reaction coordinate, r.

To perform the likelihood maximization, a model, $p(TP|r)$, that fits the simulation realization of the transition path probabilities obtained from the transition path ensemble is required. This function must have a maximum at the transition state with both sides decaying to zero. A model function commonly used[120, 12, 18] is

$$p(TP|r) = p_0(1 - \tanh[r^2]). \tag{3.10}$$

where p_0 is an adjustable parameter, and $r(\mathbf{q})$ is the reaction coordinate, which depends on some order parameters $\mathbf{q} = q_1, q_2, ..., q_n$. The reaction coordinate can be modelled as a linear combination of the order parameters

$$r(\mathbf{q}) = \sum_{k=1}^{n} \alpha_1 q_k - \alpha_0 \tag{3.11}$$

where the coefficients $\alpha_0, \alpha_1, ..., \alpha_n$, are free parameters. The likelihood expression,

$$L_{ij} = \prod_{k}^{TP} p_{ij}(TP|\mathbf{q}_k)) \prod_{k}^{non-TP} (1 - p_{ij}(TP|r(\mathbf{q}_k))), \tag{3.12}$$

is then maximized to obtain the maximum estimate in addition to the parameters $p_0, \alpha_0, \alpha_1, ..., \alpha_n$. In order to ease the process of maximization, the log of the likelihood expression is used[121],

$$\ln L_{ij} = \sum_{i}^{TP} \ln p_{ij}(TP|\mathbf{q}_k)) + \sum_{k}^{non-TP} \ln(1 - p_{ij}(TP|r(\mathbf{q}_k))). \tag{3.13}$$

The first sum in eq. 3.13 is over all the trajectories on the $\mathbf{i} \rightarrow \mathbf{j}$ transition path while the second sum is over all the trajectories that are not on that transition path, though it may belong to another transition path. For each of the different transitions, the order parameter or their combinations which gives the highest value in the log likelihood estimate is the desired reaction coordinate. The search for the best overall reaction coordinate begins with testing all single order parameters. The order parameter with the highest likelihood estimate is the best reaction coordinate. The best single order parameter is then compared to the reaction coordinates formed by combining pairs of order parameters, which are in turn compared to the reaction coordinates formed by combining triplets of order parameters, etc. When adding a second or third order parameter, the likelihood will always increase, but a new parameter is only significant to the reaction coordinate if the increase in the likelihood is equal or greater than the Bayesian information criterion, $BIC = (1/2)\ln N_R$, where N_R is the size of the transition path ensemble. Otherwise, the previous reaction coordinate with highest log likelihood is regarded as the desired reaction coordinate.

3.3 Simulation Details

3.3.1 Aimless Shooting

In order to test this approach on a system that nucleates to multiple products, the generalized Potts model [83, 84] nucleating on a heterogeneity, which was studied in Chapter 2, is used. To harvest the transition path ensemble (TPE), an initial transition path is required. For the Potts model studied in the previous chapter, the free energy surfaces clearly show the different initial paths. The initial shooting points should lie along the channels on the $A \rightarrow B$ and $A \rightarrow C$ transition paths. 200 initial shooting points were chosen very close to the critical

sizes along the two transition paths as shown in fig. 3.3. A small time interval, Δt, is chosen as the interval in MC steps, between candidate points for the shooting. The chosen configuration is propagated forward and backward until a stable basin (A, B or C) is reached. The trajectory is said to be reactive if the forward and the backward moves end in different stable basins and non-reactive otherwise. All reactive trajectories are accepted as part of the TPE and non-reactive trajectories are rejected. If the trajectory is accepted, a new shooting point is a chosen along it from $\mathbf{x}_{-\Delta t}$, $\mathbf{x}_0$, $\mathbf{x}_{+\Delta t}$ with equal probability of 1/3, where $\mathbf{x}_0$ is the configuration of an old shooting point of a trajectory. If the trajectory is non-reactive, $\mathbf{x}_0$ is used again as the shooting point and the process is repeated. Each shooting point is saved along with the identity of the stable phases where the trajectories ended. After every 20 shooting points, the acceptance ratio is evaluated. If the the acceptance ratio is less than 40%, Δt is reduced by 1. Similarly, the the acceptance ratio is greater than 75%, Δt is increased by 1. This check ensures that the acceptance ratio is kept between $40\% - 75\%$ as small Δt keeps a new shooting point closer to the previously reactive point. We choose our initial Δt as 5 MC steps.

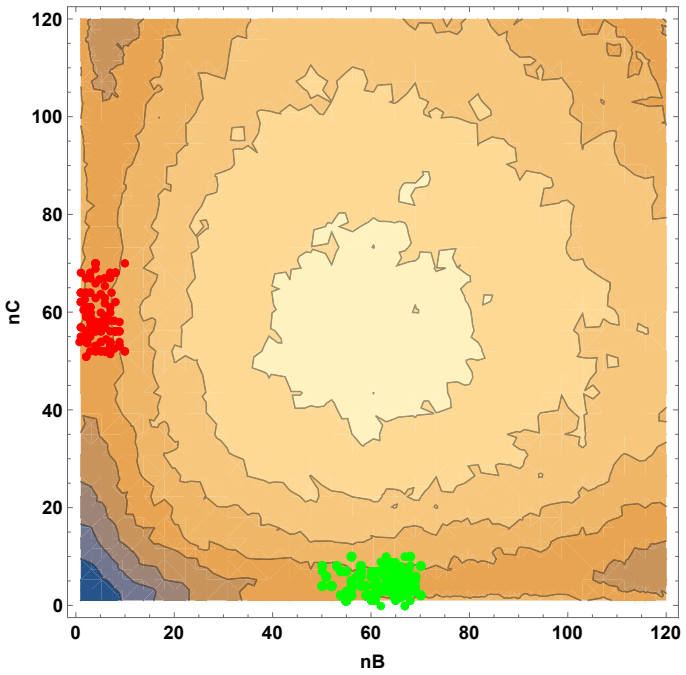

Figure 3.3: Free energy surface, $\Delta G(n_B, n_C)$, for nucleation of phases B and C showing the initial shooting points for the aimless shooting.

The aimless shooting algorithm like most TPS schemes does not require *a priori* knowledge

of the reaction coordinate. However, it is necessary to have a function that identifies when the trajectory has reached one of the end states. The characteristic functions $h_A(q)$, $h_B(q)$ and $h_C(q)$ for the identification of the metastable state (A), and the two products B and C are given by,

$$h_A(q) = \begin{cases} 1, & n_B \leq 30 \; and \; n_C \leq 30 \\ 0, & otherwise \end{cases}$$

$$h_B(q) = \begin{cases} 1, & n_B \geq 120 \; and \; n_C \leq 50 \\ 0, & otherwise \end{cases}$$

$$h_C(q) = \begin{cases} 1, & n_B \leq 50 \; and \; n_C \geq 120 \\ 0, & otherwise \end{cases}$$

Here, $q = (\sigma_1, \sigma_2, ..., \sigma_i, ...)$ denotes a given a configuration of the lattice, n_B and n_C are the B and C components of the largest cluster. The values of n_B and n_C are chosen such that they are far away from the stable regions. This ensures that once the trajectory gets into the product region, it does not go back into the reactant region. For each initial shooting point, 300 other shooting points are generated. Each shooting point is accepted into a particular transition ensemble depending on where its forward and backward trajectories end. The transitions paths are $A \rightarrow B$, $A \rightarrow C$, and $B \rightarrow C$ transitions, resulting in three sets of transition path ensembles. The aimless shooting was performed for the three different cases studied in Chapter 2 viz;

- Equal field strength
- Unequal fields without mixing
- Unequal fields with 20% mixing.

3.4 Results and Discussions

The committor probabilities calculated from the shooting points as a function of n_B when $H_B = H_C$ are shown in fig. 3.4. The committor, $p_B(n_B)$, increases with n_B, while $p_A(n_B)$ and $p_C(n_B)$ decrease with increase in n_B. At $n_B < 26$, $p_C(n_B)$ is higher than $p_A(n_B)$, and $p_A(n_B)$ seems to increase between $n_B = 26$ and $n_B = 32$ before decreasing. The stable phase on the

impurity at any given time contains both components B and C. The committor probability above is calculated using only one component, whereas at $n_B < 26$ we have configurations with $n_C >> n_B$. This means that such configurations commit to phase C more than phases A and B. As n_B increases, configurations with $n_C >> n_B$ reduces in number, making $p_A(n_B)$ higher than $p_C(n_B)$ and also causing $p_A(n_B)$ and $p_C(n_B)$ to decrease with increase in n_B. This behavior also explains why it is not possible to obtain an accurate reaction coordinate using the committor probability for a competitive process. For the committor probability to describe the reaction coordinate, it should increase monotonously, having a minimum value in the reactant and having a maximum value of one in the product. In the case of the present system, the maximum likelihood analysis is performed by maximizing the transition path probabilities.

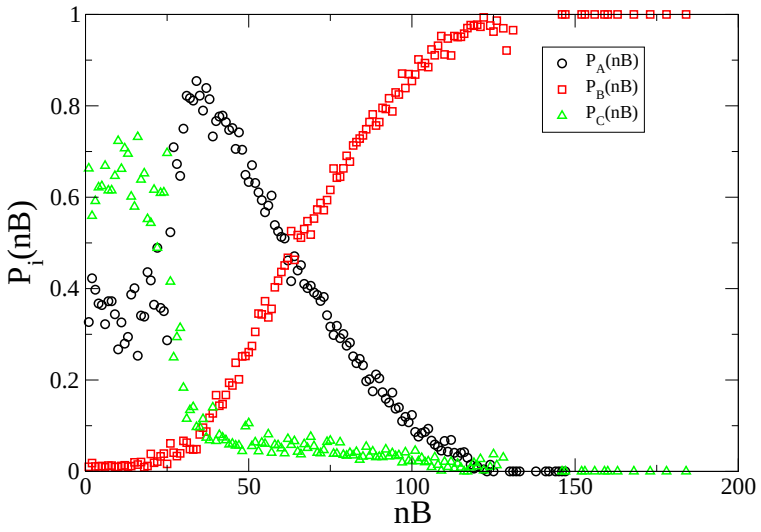

Figure 3.4: The committor probabilities, $p_A(n_B), p_B(n_B)$ and $p_C(n_B)$ as a function of the size of component B at equal fields($i.e$ $H_B = H_C = 0.12$).

When the fields, H_B, H_C, are unequal, the behaviors of $p_A, p_B,$ and p_C remain similar to those in the case of equal fields. The major difference is that $p_B(n_B)$ does not reach the value of 1.0. Also, $p_C(n_B)$ does not decay to zero as n_B increases as shown in fig. 3.5, while $p_B(n_C)$ approaches zero at larger as n_C increases. This can be understood as follows: As the free energy barrier to phase C is reduced, the probability of configurations along the $A \rightarrow B$

path committing to phase C increases, thereby reducing the probability of them ending in phase B.

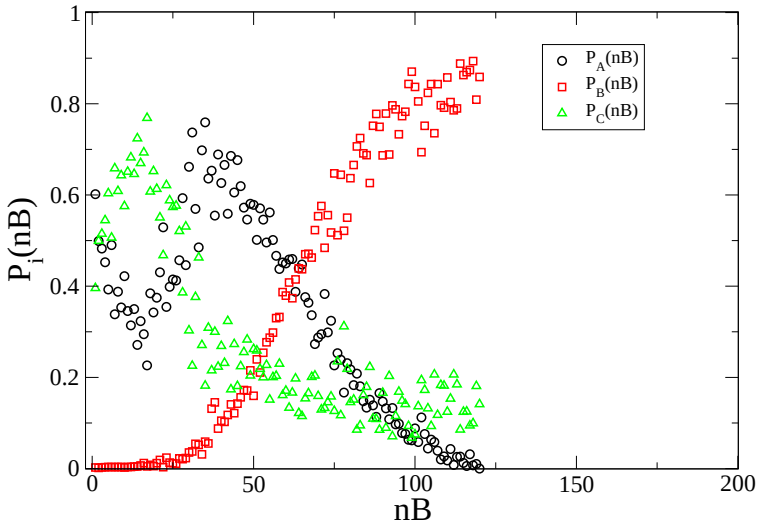

Figure 3.5: The committor probabilities, $p_A(n_B)$,$p_B(n_B)$ and $p_C(n_B)$ unequal fields($i.e$ $H_B = 0.12, H_C = 0.17$).

Fig. 3.6 shows $p_B(n_B)$ and $p_C(n_C)$ when 20% mixing is allowed between components B and C. It shows that both $p_B(n_B)$ and $p_C(n_C)$ do not reach 1.0 even at points very close to the basin of attraction defining phases B and C. When mixing is allowed, the overall free energy surface is reduced, but the phases B and C are not the basins with the lowest $\Delta G(n_B, n_C)$. Some configurations will prefer to go the region with the lowest free energy as shown in fig. 3.7. This reduces the chances of configurations ending in B and C.

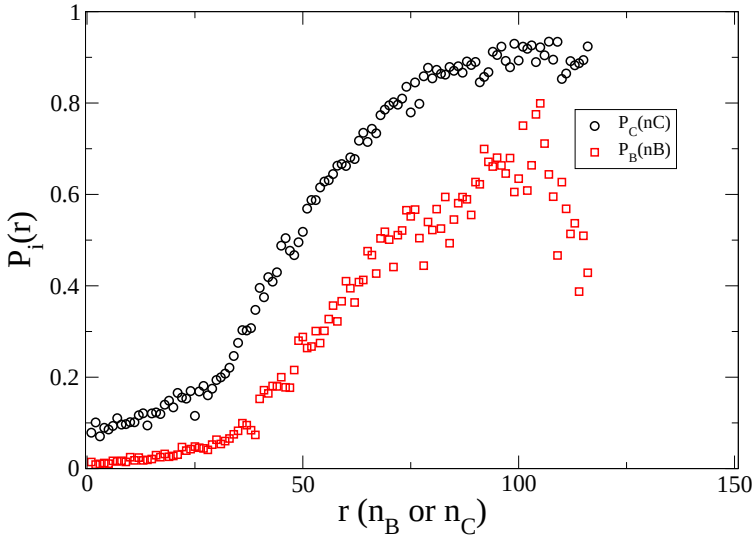

Figure 3.6: The committor probabilities, $p_B(n_B)$ and $p_C(n_C)$ unequal fields(*i.e* $H_B = 0.12, H_C = 0.17$) and $J_{B,C} = -0.8$.

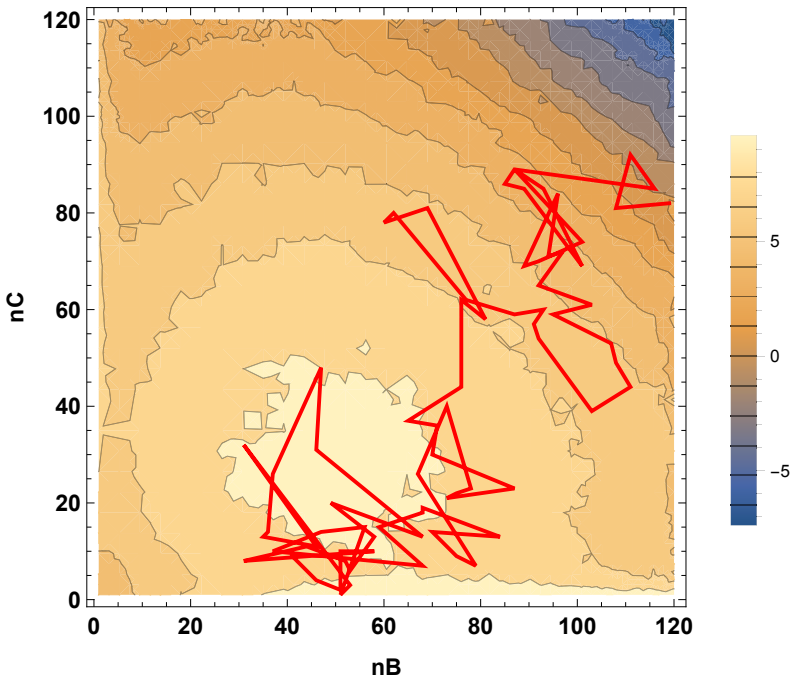

Figure 3.7: Free energy surface, $\Delta G(n_B, n_C)$, for nucleation of phases B and C when mixing is allowed, showing the initial shooting points deviating away from basins B and C .

The transition path probability, which is the probability of a given configuration being on a given transition path is calculated as a function of different order parameters. Fig. 3.8 shows plots of the transition path probabilities, $p_{ij}(TP|q)$, for the three different cases studied. Fig. 3.8(a) shows the $p_{ij}(TP|q)$ when the fields are equal. The peaks indicate the highest probabilities of being on the transition path. The $p_{AB}(TP|n_B)$ and $p_{AC}(TP|n_C)$ are equal, and are an order of magnitude larger that $p_{BC}(TP|n_B)$. This shows that $A \rightarrow B$ and $A \rightarrow C$ are the major transitions with a small percentage of $B \rightarrow C$ interconversion. When H_C increased (fig. 3.8(b)), $p_{AC}(TP|n_C)$ increased more than $p_{AB}(TP|n_B)$ while the peaks shift to a smaller value of n_C. When mixing is allowed, both $p_{AB}(TP|n_B)$ and $p_{AC}(TP|n_C)$ are reduced in values. The mixing causes a general reduction in $\Delta G(n_B, n_C)$, which also create a region with $\Delta G(n_B, n_C)$ lower than that of phase **B** or **C**. During the aimless shooting, most configurations move towards the region with lowest $\Delta G(n_B, n_C)$, causing them to move away from the $A \rightarrow B$ and $A \rightarrow C$ transition paths as shown in fig. 3.7. Fig. 3.8(c) shows a further increase in $p_{AC}(TP|n_C)$ and a significant shift in the position of its peak relative to the peak in $p_{AB}(TP|n_B)$. It also shows a significant increase in $p_{BC}(TP|n_B)$ and a change in its shape. As n_B increases, the probability of the configuration being on the $B \rightarrow C$ transition path increases.

The accurate reaction coordinate for each of the transition is obtained by subjecting the TPE along each of the transition paths to the maximum likelihood analysis. To reduce the order parameters to the same length scale for an effective comparison, the order parameters are redefined as

$$q_{n_B} = \sqrt{n_B} \tag{3.14}$$

and

$$q_{s_B} = S_B/4, \tag{3.15}$$

where S_B is the surface area of phase **B**. Another order parameter tested is the mole fraction of component **B** in the largest cluster. It is defined as,

$$\chi_{n_B} = \frac{n_B}{n_B + n_C}. \tag{3.16}$$

Table 3.1 shows the different order parameters tested, their likelihood estimates ($LE_{\alpha max}$), r and r^* for the $A \rightarrow B$ transition when the fields are equal. For the $A \rightarrow B$ transition, the linear combination of q_{n_B} and q_{s_B} is the best reaction coordinate based on the value of

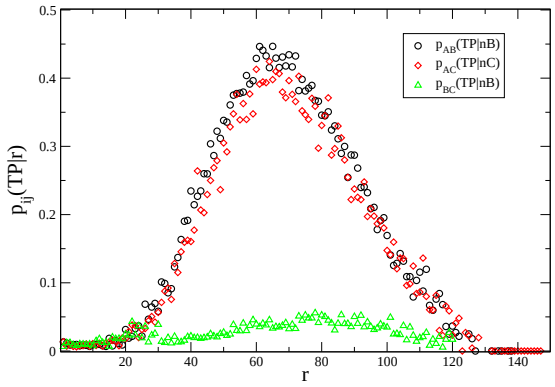

(a) Equal fields

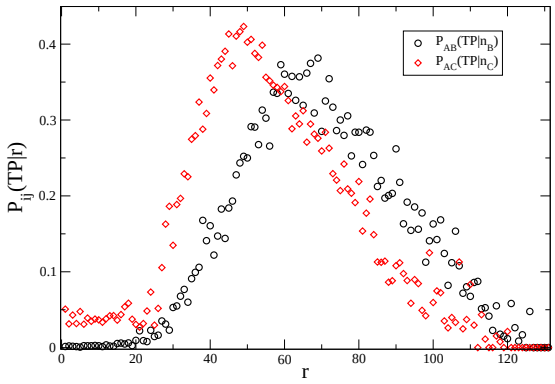

(b) Unequal fields

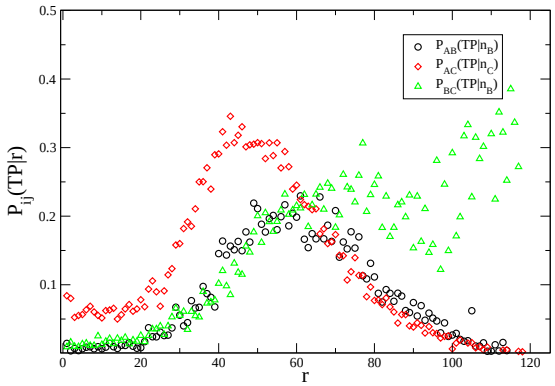

(c) Unequal fields with 20% mixing

Figure 3.8: Free energy surface, $\Delta G(n_B, n_C)$ for nucleation of phases B and C from a metastable phase on an heterogeneity of length $l = 7$.

$LE_{\alpha max}$. Table 3.2 contains same information for the $A \rightarrow C$ transition. Similarly, the linear combination of q_{n_C} and q_{s_C} is the best reaction coordinate for $A \rightarrow C$ transition. Peters *et al*. [12] showed that a combination of embryo size with its surface area is the best reaction coordinate for homogeneous nucleation in Ising model. Also, Pan and Chandler[11] analyzed the transition state ensemble for homogeneous nucleation using the Ising model, and observed that though size was the best reaction coordinate, other order parameters were still important. Both studies showed that the critical nucleus is rough and anisotropic [11, 12]. The ratio $\frac{q_S}{q_N}$ can provide some insight to the shape of the embryo in lattice models[12]. If the nuclei is a perfect square, $\frac{q_S}{q_N} = 1$, while $\frac{q_S}{q_N} = 2/\sqrt{\pi}$ (≈ 1.13) for a rounded 2-dimensional lattice nuclei. Fig. 3.9 shows the shooting points from the $A \rightarrow B$ transition path projected onto the order parameters q_{n_B} and q_{s_B}. The green line is the least squares fit, $q_{s_B} = 1.50 q_{n_B}$, which indicates that the nuclei adopt the rectangular shape of the impurity which has $\frac{q_S}{q_N} = 1.51$. The red line shows the critical condition, $q^*_{s_B} = 13.82\sqrt{n_B} - 102.04$. It shows that the surface, S_B is dependent on the size such that small critical nuclei are compact with small surface areas unlike the small fractal nuclei observed by Peters *et al* [12]. Large nuclei have large surface area, while small nuclei have small surface area.

Order Parameters	r	$LE_{\alpha max}$	$r = 0$ surface (r^*)
q_{n_B}	$0.5399 q_{n_B} - 4.369$	-24977.1	$n^*_B = 64.85$
q_{n_C}	$0.3296 q_{n_C} - 0.7527$	-26193.7	$n^*_C = 5.24$
q_{s_B}	$0.2667 q_{s_B} - 2.763$	-27143.3	$S^*_B = 41.5$
q_{s_C}	$0.2405 q_{s_C} - 0.4604$	-26740.2	$S^*_C = 7.68$
q_{n_B}, q_{s_B}	$0.6014 q_{n_B} - 0.0435 q_{s_B} - 4.439$	-23940.2	$S^*_B = 55.26\sqrt{n_B} - 407.83$
χ_{n_B}	$3.54519 \chi_{nB} - 2.81708$	-25656.5	$\chi^*_{n_B} = 0.796$

Table 3.1: Different order parameters tested for $A \rightarrow B$ transitions in the Potts model with equal fields. $BIC = (1/2)\ln N_R = 4.36$.

For the case where the fields are unequal, the linear combination of q_{n_B} and q_{s_B} is the best reaction coordinate for $A \rightarrow B$ transition, while the linear of q_{n_C} and q_{s_C} is the best reaction coordinate for $A \rightarrow C$ for the nucleation of phase C, as can be seen in Tables 3.3 and 3.4. Allowing for mixing between the different components seems to change the dynamics of the

Order Parameters	r	$LE_{\alpha max}$	$r = 0$ surface
q_{n_B}	$0.3442q_{n_B} - 0.8718$	-24460.3	$n_B^* = 6.42$
q_{n_C}	$0.5258q_{n_C} - 4.224$	-23427.0	$n_C^* = 64.54$
q_{s_B}	$0.2471q_{s_B} - 0.5336$	-25017.8	$S_B^* = 8.65$
q_{s_C}	$0.2648q_{s_C} - 2.7218$	-25362.1	$S_C^* = 41.15$
q_{n_C}, q_{s_C}	$0.5784q_{n_C} - 0.0382q_{s_C} - 4.279$	-23401.2	$S_B^* = 60.56\sqrt{n_C} - 448.06$
χ_{n_C}	$3.6589\chi_{nB} - 2.8178$	-23822.8	$\chi_{n_C}^* = 0.7701$

Table 3.2: Different order parameters tested for $A \rightarrow C$ transitions in the Potts model. $BIC = (1/2)\ln N_R = 4.65$.

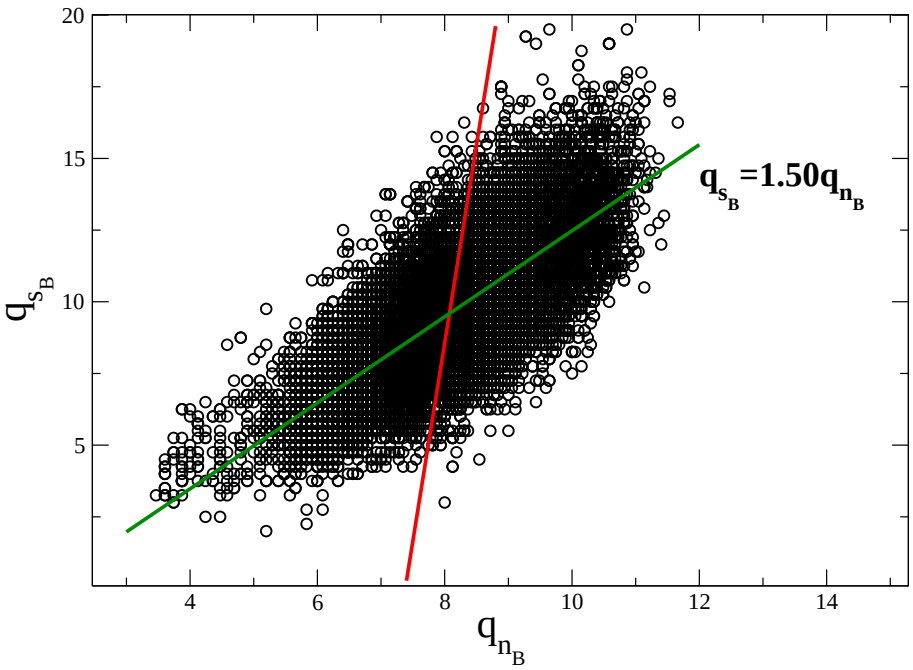

Figure 3.9: Shooting points showing the collective variables (q_{s_B}, q_{n_B}) for the $A \rightarrow B$ TPE. The red line shows the critical condition, while the green line is a least squares fit , $q_{s_B} = 1.50q_{n_B}$.

transformations because it leads to the introduction of a new stable state at large n_B and n_C, that renders phases B and C metastable. The maximum likelihood analysis shows that the linear combination of q_{n_C} and q_{S_C} is the best reaction coordinate for $A \rightarrow B$ transition as shown in Table 3.5. This seems counter intuitive. However, increasing the interaction parameter, J_{BC}, allows the components to mix with relative ease. Also, H_C is higher than H_C which means C has lower free energy barrier. Therefore, making phase C more probable to nucleate. Hence, to increase the probability of forming phase B, component C must be removed. Hence q_{n_C} becomes an important order parameter for the $A \rightarrow B$ transition. This is an example of the order parameter working in a negative sense, *i.e*, where the removal of the particular type of structure, characterized by the order parameter, allows the transition to occur. Table 3.6 contains the maximum likelihood results for $A \rightarrow C$ transition when mixing is allowed. It shows that the overall size, $N = n_B + n_C$, is the best reaction coordinate for the transition. With mixing allowed, the entire free energy surface becomes a transition path for the $A \rightarrow C$ transition. Any chosen configuration has a higher probability of going to phase C than B.

Order Parameters	r	$LE_{\alpha max}$	$r = 0$ surface
q_{n_B}	$0.6068q_{n_B} - 4.9307$	-15356.1	$n_B^* = 66.02$
q_{n_C}	$0.4361q_{n_C} - 1.0486$	-16323	$n_C^* = 5.78$
q_{s_B}	$0.2985q_{s_B} - 3.108$	-17074	$S_B^* = 41.65$
q_{s_C}	$0.3145q_{s_C} - 0.5377$	-17013	$S_C^* = 6.84$
q_{n_B}, q_{s_B}	$0.7282q_{n_B} - 0.0847q_{s_B} - 5.0877$	-15272	$S_B^* = 34.39\sqrt{n_B} - 240.26$
χ_{n_B}	$4.2022\chi_{nB} - 3.5698$	-15941.5	$\chi_{n_B}^* = 0.849$

Table 3.3: Different order parameters tested for $A \rightarrow B$ transitions in the Potts model with unequal fields. $BIC = (1/2)\ln N_R = 4.36$.

Order Parameters	r	$LE_{\alpha max}$	$r = 0$ surface
q_{n_B}	$0.2863q_{n_B} - 0.8557$	-31443	$n_B^* = 8.93$
q_{n_C}	$0.4957q_{n_C} - 3.5411$	-31038	$n_C^* = 51.0$
q_{s_B}	$0.2055q_{s_B} - 0.5652$	-31871.8	$S_B^* = 11.0$
q_{s_C}	$0.2419q_{s_C} - 2.2031$	-32789	$S_C^* = 36.43$
q_{n_C}, q_{s_C}	$0.5779q_{n_C} - 0.0574q_{s_C} - 3.638$	-30979.2	$S_B^* = 40.27\sqrt{n_C} - 253.52$
χ_{n_C}	$2.8811\chi_{nB} - 0.5205$	-31733.2	$\chi_{n_C}^* = 0.18$

Table 3.4: Different order parameters tested for $A \rightarrow C$ transitions in the Potts model with unequal fields. $BIC = (1/2)\ln N_R = 4.65$.

Order Parameters	r	$LE_{\alpha max}$	$r = 0$ surface
q_{n_B}	$0.6116q_{n_B} - 4.6099$	-17453.0	$n_B^* = 56.8$
q_{n_C}	$0.4302q_{n_C} - 1.1771$	-16349.9	$n_C^* = 7.5$
q_{s_B}	$0.3048q_{s_B} - 2.7514$	-19163.8	$S_B^* = 36.1$
q_{s_C}	$0.2780q_{s_C} - 0.5315$	-17155.4	$S_C^* = 7.64$
q_N	$0.5367q_N - 4.6082$	-19461.6	$N^* = 73.71$
q_S	$0.1928q_S - 2.2245$	-19922.6	$S^* = 46.13$
q_{n_B}, q_{s_B}	$0.6894q_{n_B} - 0.0596q_{s_B} - 4.6776$	-17415.6	$S_B^* = 46.26\sqrt{n_B} - 313.88$
q_{n_C}, q_{s_C}	$0.4789q_{n_C} - 0.0377q_{s_C} - 1.2073$	-16340.5	$S_C^* = 50.79\sqrt{n_C} - 128.02$

Table 3.5: Different order parameters tested for $A \rightarrow B$ transitions in the Potts model with $H_C = 0.17, H_B = 0.12$ and 20% mixing. $BIC = (1/2)\ln N_R = 4.36$.

Order Parameters	r	$LE_{\alpha max}$	$r = 0$ surface
q_{n_B}	$0.2789q_{n_B} - 0.8361$	-34789.1	$n_B^* = 8.98$
q_{n_C}	$0.4959q_{n_C} - 3.2706$	-35879.3	$n_C^* = 43.49$
q_{s_B}	$0.1919q_{s_B} - 0.4443$	-35516.5	$S_B^* = 9.26$
q_{s_C}	$0.2298q_{s_C} - 1.7489$	-38169.2	$S_C^* = 30.59$
q_N	$0.5949q_N - 4.7879$	-33075.2	$N^* = 64.77$
q_S	$0.1847q_S - 1.8565$	-35421.3	$S^* = 40.18$
q_{n_B}, q_{s_B}	$0.2951q_{n_B} - 0.0129q_{s_B} - 0.8478$	-34786.7	$S_B^* = 91.51\sqrt{n_B} - 262.85$
q_{n_C}, q_{s_C}	$0.5808q_{n_C} - 0.0584q_{s_C} - 3.3835$	-35793.6	$S_C^* = 39.81\sqrt{n_C} - 231.84$

Table 3.6: Different order parameters tested for $A \rightarrow C$ transitions in the Potts model with $H_C = 0.17, H_B = 0.12$ and 20% mixing. $BIC = (1/2)\ln N_R = 4.36$.

For all the three cases studied, there is always a $B \rightarrow C$ interconversion. For all the $B \rightarrow C$ transitions, the mole fraction, χ_{nC}, is the best reaction coordinate. Although size is not the best reaction coordinate for these transitions, the critical sizes obtained from the multiple paths maximum likelihood analyses are comparable to those obtained from the free energy surfaces in Chapter 2 (see fig. 3.10). This suggests that the method of decoupling the transition path is rigorous and accurate, provided the order parameters are unique to each phase.

The accuracy of the obtained reaction coordinates can be verified through the committor distribution. To do this, MC simulations of configurations belonging to the transition state as identified by the reaction coordinate are made and the probability of it ending in a given phase is evaluated. Fig. 3.11 shows the committor histogram for (a) $r(q_{n_C})$ and (b) $r(q_{n_C}, q_{s_C})$ for the $A \rightarrow C$ transition. To produce the histogram in fig. 3.11(a), a set of 120 configurations restricted to $q_{n_C}^* = 8.033$ ($n_C^* = 64.54$) are selected from the TPE. For each of the configurations, 100 trajectories are propagated till a stable phase defined by the characteristic functions is reached. p_C is calculated as the ratio of trajectories which ended in phases C. For fig. 3.11(b), 110 configurations lying on the line $q_{s_C}^* = 15.14\sqrt{n_C} - 112.02$ are selected and shows that the committor distribution has a peak at $p_C \approx 0.5$, indicating that a configuration in the TSE has equal chance of forming C or shrinking. This shows that

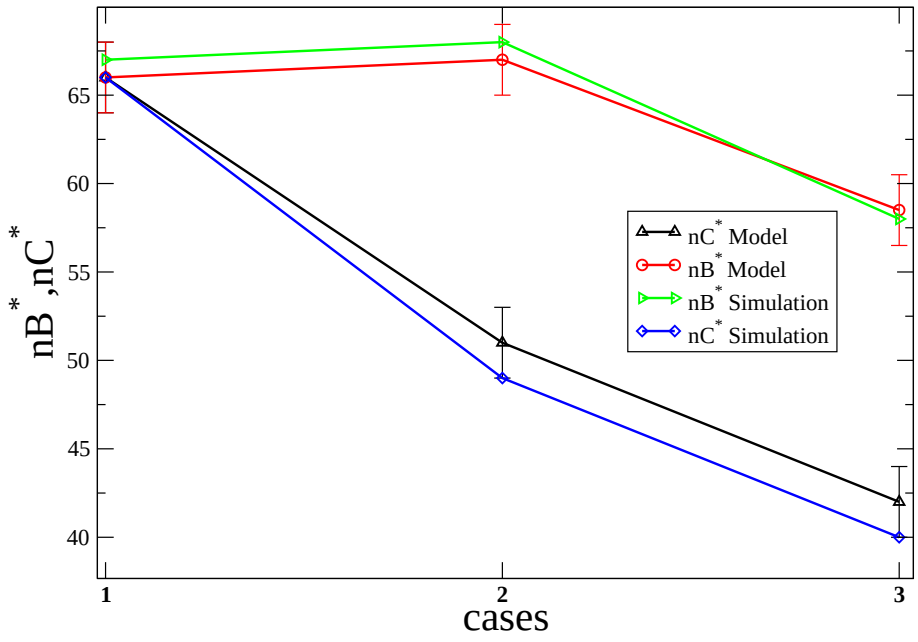

Figure 3.10: Comparison of the critical sizes obtained from free energy surfaces and those from the MPMLA for the different cases.

$r(n_B, S_B)$ is an accurate estimate of the reaction coordinate for the $A \rightarrow B$ transition, while $r(n_C, S_C)$ is the best reaction coordinate for the $A \rightarrow C$ transition.

3.5 Conclusions

In this chapter, the maximum likelihood method has been extended to obtain reaction coordinate for multiple products transitions. Multiple states transition path sampling is used to harvest reactive trajectories along the different transition paths. Defining the likelihood model for different reaction paths, the best reaction coordinate for the different transitions are obtained. The results show that decoupling the different transition paths is rigorous and accurate to obtained the best reaction coordinates. Also, it is important that the order parameters tested are unique properties of each of the competing phases. The values of these order parameters in relationship to others can be used to follow the progress of the phases during a competitive process. The shape of the nuclei is highly correlated to the shape of the heterogeneity, which can be explored in crystal seeding and other fabrication processes.

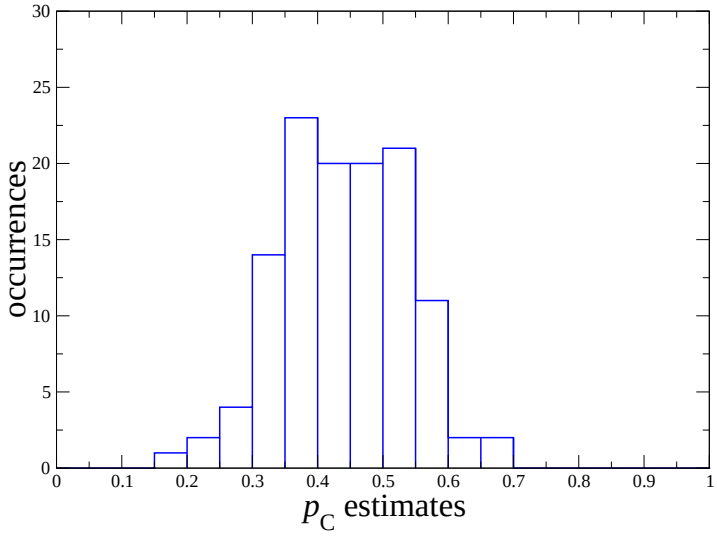

(a) $r(n_C)$

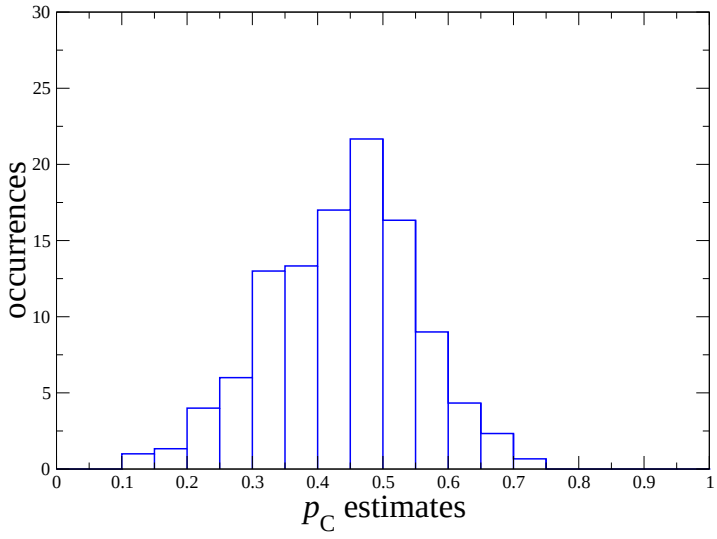

(b) $r(n_C, S_C)$

Figure 3.11: A committor probability distributions for two reaction coordinates obtained from the maximum likelihood analysis.

Chapter 4

Competitive Rates of Freezing in Gold Nanoclusters

4.1 Introduction

It is well known that small atomic clusters form a variety of novel structure types, including non-crystalline solids such as icosahedra (Ih) and decahedra (Dh). The relative stability of the structures is determined by the competition between surface and volume effects. An icosahedron is generally more stable at small sizes due to its low surface energy, but as the cluster size grows, the decahedron becomes more stable because it reduces the degree of internal stress. Experimental [122] and simulation [123, 124] studies of gold clusters both suggest that the thermodynamic crossover from $Ih \rightarrow Dh$ occurs at cluster sizes $N < 100$ and the $Dh \rightarrow FCC$ transition sets in at $N \approx 400-500$, but the Ih structure is still observed to be the dominant structure formed in clusters containing a few thousand atoms [1]. Chusak and Bartell [1] observed that gold clusters of size, $N \sim 450$, freezing from the same conditions, led to the formation of various motifs such as Ih, Dh and FCC, with Ih being the most prevalent. This study suggests that freezing in nanoclusters is a competitive process where a single droplet may freeze to one of a number of different structures. Therefore, it is expected that there is a distribution of different cluster types which appear with a given probability that is determined by the relative heights of the nucleation barriers for each structure. The goal of this chapter is to study the competitive nature of the nucleation in freezing gold nanoclusters and to understand the factors that influence the probabilities of observing the different structures. To achieve this, ensembles of nucleation events are studied in order to find the nucleation probabilities of the clusters over a range of cluster sizes and temperatures. These are then related to both the nucleation rates and the difference in free energy barriers for the various processes.

4.2 Simulation Methods

4.2.1 Simulation Details

Gold clusters with sizes ranging between 309 and 923 are studied. These include three clusters with magic numbers for Mackay icosahedra $(309, 561, 923)$, two clusters of perfect Marks decahedra $(389, 686)$ and four clusters with sizes, $N = 459, 500, 600, 800$. The particles within the clusters interact with each other through the embedded atom method (EAM) interaction potential[125] within a canonical ensemble (NVT). The EAM potential is built on the insight gained through density functional theory (DFT) which uses the local electron density to deduce the energy of the system. It is based on the assumption that the total electron density of a metal is approximated by a linear superposition of the density from individual atoms. The electronic density in the vicinity of each atom is expressed as the sum of the density contributed by the atom plus a constant background density. The total energy of an atom is given as:

$$E_i = F_i(\rho_i) + 1/2 \sum_{j(i \neq j)}^{N_{nb}(i)} V_{i,j}(r_{ij}). \tag{4.1}$$

Here $V_{ij}(r_{ij}) = \frac{1}{4\pi\epsilon_0} Z_i^a(r_{ij}) Z_j^a(r_{ij})/r_{ij}$ is the pair potential between atom i and its neighbor j, and r_{ij} is the inter-atomic distance for atomic pair. The local electron density, ρ, for atom i is given as

$$\rho_i = \sum_{j(\neq j)} \rho_j^a(r_{ij}). \tag{4.2}$$

The values of the parameters used in the calculation of electron density, $\rho_j^a(r_{ij})$, the pair potential, V_{ij} and the embedded atomic potential functional $F_i(\rho_i)$ are obtained by fitting experimental data to information such as lattice parameters, elastic constants, cohesive energies, vacancy formation energy etc. The EAM shows a better overall agreemeent to experimental surface energies, and shows a more practical finite temperature and finite FCC and HCP lattice energy [126] difference over potentials such as Foiles *et al* [125], Johnson [127] and the glue potential[128]. The simulations are carried out in the NVT ensemble in a cubic simulation cell with volume $V = 1 \times 10^6$ Å^3 and periodic boundaries. The equations of motion are integrated using the velocity Verlet algorithm with a time step, $\Delta t = 2.8$ fs and the Noose-Hoover thermostat [129, 130] is used to maintain a constant temperature, T.

For each of the cluster sizes considered, an approximate spherical structure with FCC lattice is constructed. Each cluster is heated from 300 K to 1500 K in increments of 50 K. At each temperature the cluster is equilibrated for 2.5×10^5 time steps. The choice of the final temperature ensures the complete melting of the nanocluster. The final configuration is further equilibrated for 2.5×10^5 time steps at 1000 K to generate 500 different configurations each saved after every 140 ps. This ensemble of 500 configurations serves as the starting configurations for the freezing runs. Each set of the 500 configurations are cooled to a given temperature between 680 K and 740 K by a spontaneous jump in the temperature, which involved assigning each atom a random velocity from a uniform distribution appropriate for the new T. The MD simulations were then allowed to run for 4.8×10^5 time steps, a time long enough to observe freezing in nearly all the trajectories. Configurations along the trajectory were saved every 500 time steps for structural analysis.

Freezing events are recognized by the evolution of the configurational energy and through the global order parameter described below. The onset of freezing is marked by a sudden drop in the energy. Fig. 4.1 shows the evolution of the energy per particle, U/N, for a 561-atom cluster, for 6 MD runs at 700 K. Five of the trajectories show the characteristic drop in the energy that signifies freezing while one trajectory remains liquid on the time scale of the simulation.

4.2.2 Structural Analysis

Bond Order Parameters

The structure of the clusters is studied using a number of order parameters based on the Steinhardt[14] bond order parameters. The bond orientational order parameter, Q_l, is defined as

$$Q_l = \sqrt{\frac{4\pi}{2l+1} \sum_{m=-l}^{l} |\frac{1}{N} \sum_{i=1}^{N} q_{lm}(i)|^2}, \tag{4.3}$$

where

$$q_{lm}(i) = \frac{1}{N_{nb}} \sum_{j=1}^{N_{nb}(i)} Y_{lm}(\mathbf{r}_{ij}). \tag{4.4}$$

The summation in eqn 4.4 is over the number of neighbors, (N_{nb}), for atom i, where two atoms are considered neighbors if the distance between them is less than or equal to 3.5 Å, which is the radius corresponding to the first minimum of the radial distribution function

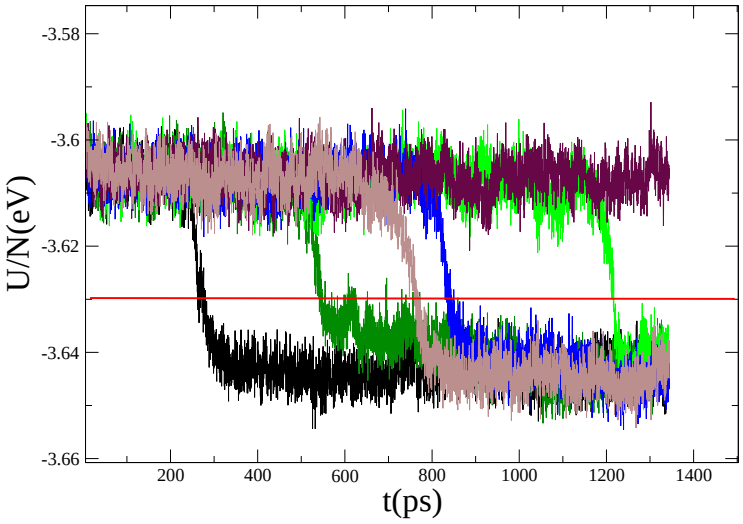

Figure 4.1: The energy of the cluster per atom as a function of simulation time for six trajectories ($N = 561$). The red solid line, $U = -3.63eV$, identifies the energy used to determine when a cluster has nucleated.

for gold. $Y_{lm}(\mathbf{r}_{ij}) = Y_{lm}(\theta_{ij}, \phi_{ij})$ are the spherical harmonic functions, where θ and ϕ are the polar and azimuthal angles of the vector $\mathbf{r}_{ij}$, respectively; l is is a free integer parameter, and m is an integer that runs from $m = -l$ to $m = +l$. The value of q_{lm} depends on the relative positions and orientations of the neighbors of atom i, and therefore allows the evaluation of the structures of clusters with different symmetries depending on the choice of l. For this work, $l = 6$ is chosen since Q_6 is sensitive to hexagonal structures and gives non-zero Q_6 values for the cluster structures observed in our simulations. Q_l have been used extensively in studies of clusters [44, 131, 2] and liquid-solid nucleation in the bulk [132].

The Q_s and Q_b, which are just the Q_6 order parameters calculated independently for the surface and bulk atoms of the cluster [2], are also measured. These help us to understand how surface ordering may play a role in the freezing of the clusters as well as distinguishing between different structure types. They are defined as

$$Q_{b,s} = \sqrt{\frac{4\pi}{13} \sum_{m=-6}^{6} |\frac{1}{N_{b,s}} \sum_{i=1}^{N_{b,s}} q_{6m}(i)|^2}, \tag{4.5}$$

where N_b and N_s are the number of surface and bulk atoms, respectively. To distinguish the

surface atoms from the bulk atoms, a slightly modified "cone" algorithm[131] is used. For a given atom, a "cone region" is defined as the region inside a cone of side length, l_c, with azimuthal angle, θ_c, and whose vertex rests on the atom center. An atom is said to be on the surface if it is possible to find a cone surrounding the particle that contains no other atoms, otherwise, the atom is regarded as bulk atom. Fig. 4.2 shows a diagram of how the cone algorithm is used to probe surface and bulk atoms. For this work, $\theta_c = 120°$ and $l_c = 3.5$ Å.

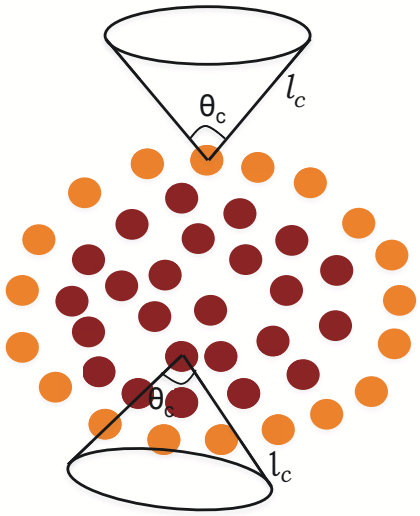

Figure 4.2: A diagram showing how surface and bulk atoms are identified using the cone having azimuthal angle, θ_c, and side length, l_c. The upper cone identifies a surface atom while the lower cone shows a bulk atom.

Common Neighbor Analysis

The local order of the individual atoms is studied using a common neighbor analysis (CNA) [133, 134, 135]. This method, which identifies atoms by considering the number and connectivity of the neighbors shared by two neighboring atoms, was first proposed by Honeycutt and Anderson[136]. Considering a pair of atoms, α and β, the CNA is classified by a set of indexes, (i), (ii), (iii) and (iv). The indexes: **(i)** indicates whether α and β are nearest neighbors ($i = 1$) or not ($i = 2$); **(ii)** indicates the number of nearest neighbors shared by α and β, which are called common neighbors; **(iii)** indicates the number of bonds or connections among the common neighbors; **(iv)** indicates the number of bonds in the longest continuous chain formed by the common neighbors. In this work, two atoms are considered neighbors if the distance between them is less than or equal to 3.5 Å.

Fig. 4.3 is an illustration of a diagram constructed from the classification of local structural environments. Atoms i (brown) and j (yellow) are a pair of nearest neighbors, while atoms k (blue) are the common neighbors to the pair, *i,j*. From this figure it can be seen that i and j have 4 common neighbors, and these common neighbors have 2 bonds between themselves. Also, the pair bond with their common neighbors in the same way, with two bonds in the longest chain. Therefore, the CNA environment of i with respect to j is **1422**. The local environment of an atom is determined in the both bulk and surface based on the number of CNA environments that an atom forms with its nearest neighbors. An atom is regarded as a bulk atom if the number of nearest neighbors is greater than or equal to 10, and a surface atom otherwise. For a bulk atom, if the number of pairs with index 1421 is equal or greater than 5, then that atom has an fcc local structure. It be noted that fcc is used to identify the local environment of the atom, while FCC identifies the entire cluster structure. Other indexes used for bulk atoms include 1422 and 1555. If the number of pairs for a given atom with 1555 is greater than or equal to 2, then the atom is bulk Ih, if the number of pairs with index 1422 is greater than or equal to 5, then the atom has *hcp* local environment. Bulk atoms not identified as fcc, Ih or *hcp* are regarded as amorphous. For surface atoms, if the number of pairs for a given atom with 1555 is greater than or equal to 1, then the atom is $Ih - vertex$. If the number of pairs for a given atom with 1211 is greater than or equal to 3, then the atom is on the 100 surface. There are some local environments on the surface, which cannot be identified by counting a single index. Examples of such local structures include, 111, $Ih - edge$, $Ih - join$ and $fcc - edge$, therefore a combination of indices such as 1211,1311, 1322, and 1422 are used to identify such local environments. A surface atom not identified as being a vertex, on an edge, joint, on the 111 or 100 planes is regarded as an amorphous atom on the surface.

Finally, the effectiveness of our structural analysis is dramatically improved when performed on configurations that have been subjected to a conjugate gradient quench that takes the configuration to its local potential energy minimum, or an inherent structure [137], to remove the thermal noise from the structure. All the structural quantities reported in this chapter refer to our analysis on these quenched configurations.

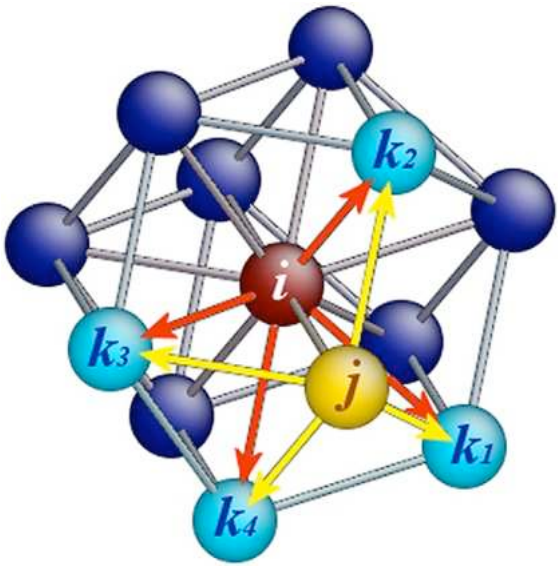

Figure 4.3: Diagrams showing how the classification of local structures defined in CNA are constructed. Reproduced with permission from ref. [135]

4.3 Results and Discussions

4.3.1 Structural Identifications

All the clusters quickly establish a stable energy profile at early times in the trajectory indicating that they have reached a state corresponding to a metastable liquid droplet. Most of the trajectories then exhibit a rapid decrease in energy as the cluster freezes to a solid structure while a fraction of clusters remains liquid to the end of the simulation run (see fig. 4.1). Examples of all the structure types observed in our simulations are shown in fig. 4.4 with some of the different structural motifs appearing in the core of the clusters highlighted using the CNA. In fig. 4.4, CNA atom types have been enlarged and colored to highlight the important structural motifs for each cluster type. Note that, not all atom types are highlighted for all structures. Red indicates amorphous, pink indicates bulk *Ih*, blue indicates surface *Ih*-edge, purple indicates surface *Ih*-vertex, brown indicates bulk *hcp* and green indicates bulk *fcc*. The remaining atoms are represented as points, making it easy to visualize. The liquid cluster, along with Ih, Dh, Dh_2 and FCC structures are observed in all cluster sizes studied but the structure denoted Th is only formed by the $N = 923$ cluster.

To study the structure of the liquid drop, the average number of atoms with each CNA

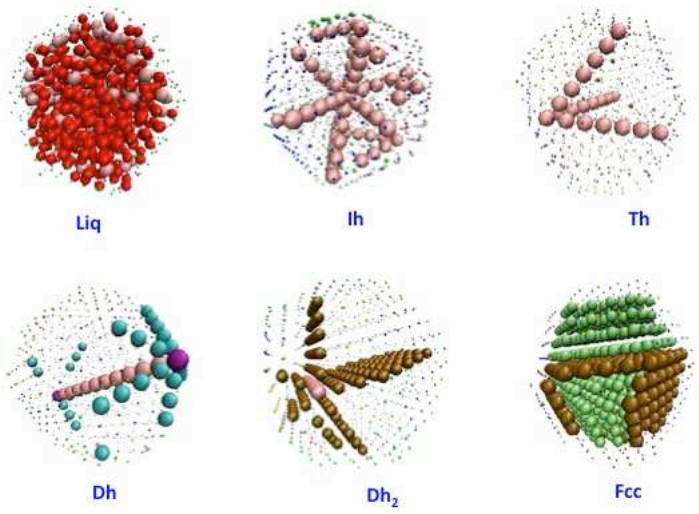

Figure 4.4: Different structural types observed for the $N = 923$ cluster. For the structures shown, red indicates amorphous, pink indicates bulk *Ih*, blue indicates surface *Ih*-edge, purple indicates surface *Ih*-vertex, brown indicates bulk *Hcp* and green indicates bulk *fcc*. The remaining atoms are represented as points for clarity

identity from the trajectories that did not exhibit a freezing event is obtained (fig. 4.5). The core of the droplet is relatively disordered and is dominated by amorphous and bulk icosahedral atoms. There are a few *fcc* or *hcp* atoms and the fraction of these increases marginally with decreasing temperature. The surface is also relatively disordered with the amorphous and Ih-vertex atoms being most abundant. However, 20-25% of the surface atoms are either $\langle 111 \rangle$ or *Ih*-edge atoms which are the atom types necessary to form the surface of an *Ih* cluster. The fraction of these atom types also increases with decreasing T, which is consistent with Nam et al [138] who observed an increase in the *Ih* surface order of gold nanoparticles as they were cooled. Fig. 4.6 and fig. 4.7 plot the number of bulk icosahedral atoms, $N_{b(Ih)}$, as a function of Q_6 for cluster sizes $N = 561$ and $N = 923$, respectively, while fig. 4.8 and fig. 4.9 show plots of Q_s as a function of Q_b for the same cluster sizes. The initial liquid drops and the drops that did not freeze, denoted as Liq* in fig. 4.7 and fig. 4.9, occupy the same region in the order parameter plots showing that the liquid structure does not evolve systematically in time.

While a perfect icosahedron was never seen in simulations, all the Ih structures observed have a significant number of the 20 possible tetrahedral subunits completed and a single, clearly defined icosahedral atom at the center, forming the vertex of the tetrahedral subunits. Most of the tetrahedral subunits are the correct size for a given cluster size, but subunits that are either one layer of atoms too small or too large are also observed. In all the Ih clusters there is a small number of neighboring subunits that are deformed or disordered and the CNA identifies the atoms in these sections as either amorphous or *Ih* bulk.

The Dh structures formed in the simulations all exhibit a line of the bulk icosahedral atoms running through the center of the cluster and at least one well formed five-fold symmetric cap made of $\langle 111 \rangle$ planes and $Ih - edge$ atoms. The Dh_2 structures, with the diagnostic line of bulk icosahedral atoms located off-center of the cluster, have been seen previously [1, 139] but it should be noted that the Dh_2 clusters all lack the presence of the cap surface structure. Later, the analysis of the freezing trajectories shows that the cap formation is a key initial step in the formation of the Dh solids, suggesting that the Dh_2 may have a different nucleation pathway. The *FCC* structures appear as truncated octahedra with a mix of *fcc* and *Hcp* stacked planes and a combination of $\langle 100 \rangle$ and $\langle 111 \rangle$ faces. The *Th* structure contains three lines of five-fold symmetric bulk *Ih* atoms forming the edges of a slightly truncated

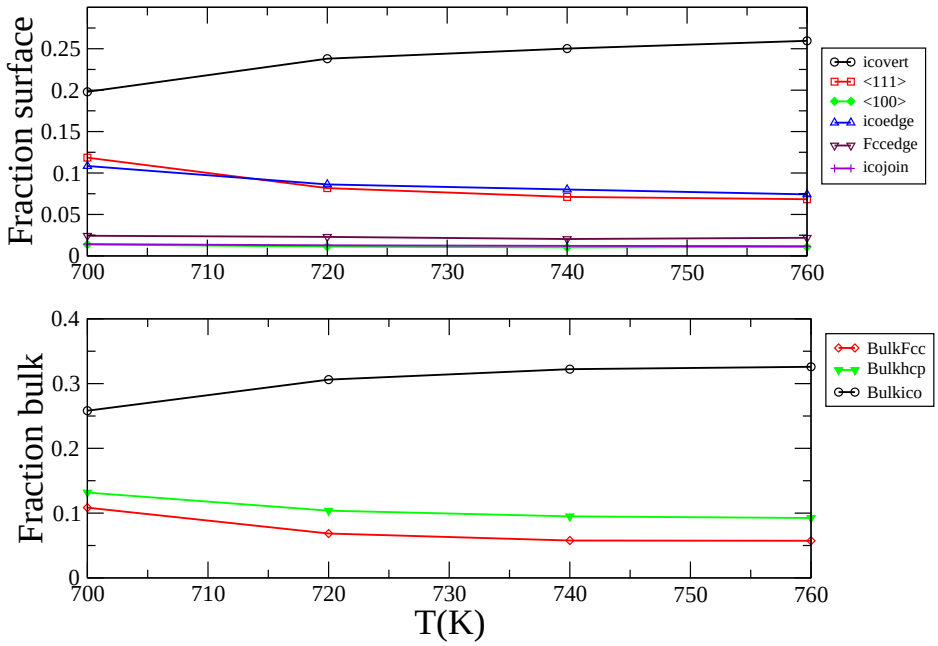

Figure 4.5: The fraction of surface (top) or bulk (bottom) atoms of a given CNA type as a function of temperature for liquid particles. Fraction of amorphous atoms not shown.

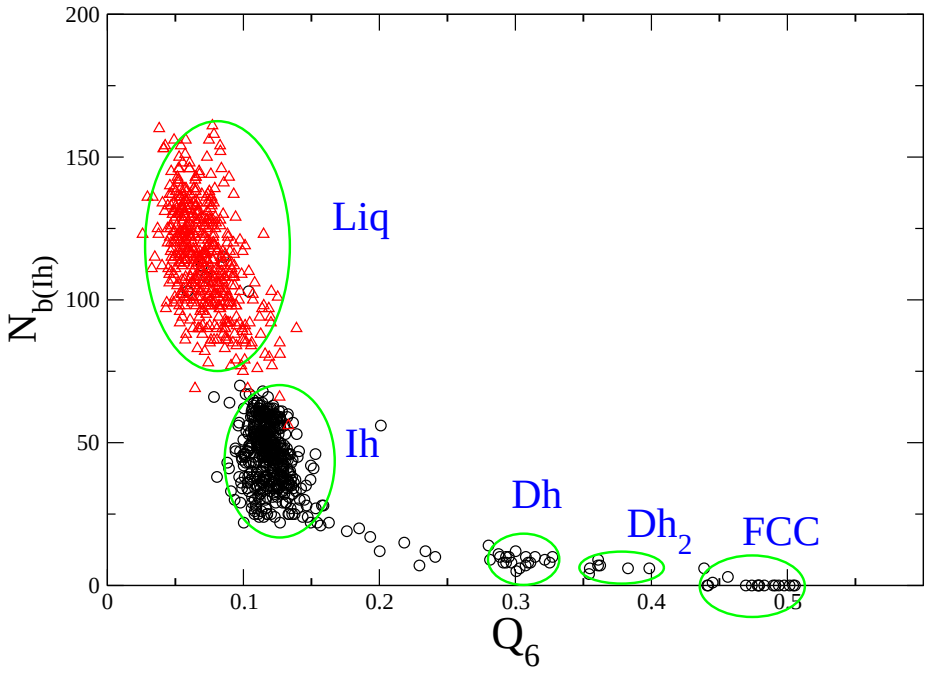

Figure 4.6: $N_{b(Ih)}$ as a function of Q_6 for the initial liquid configuration (triangles) and the final configurations (circles) of the $N = 561$ clusters.

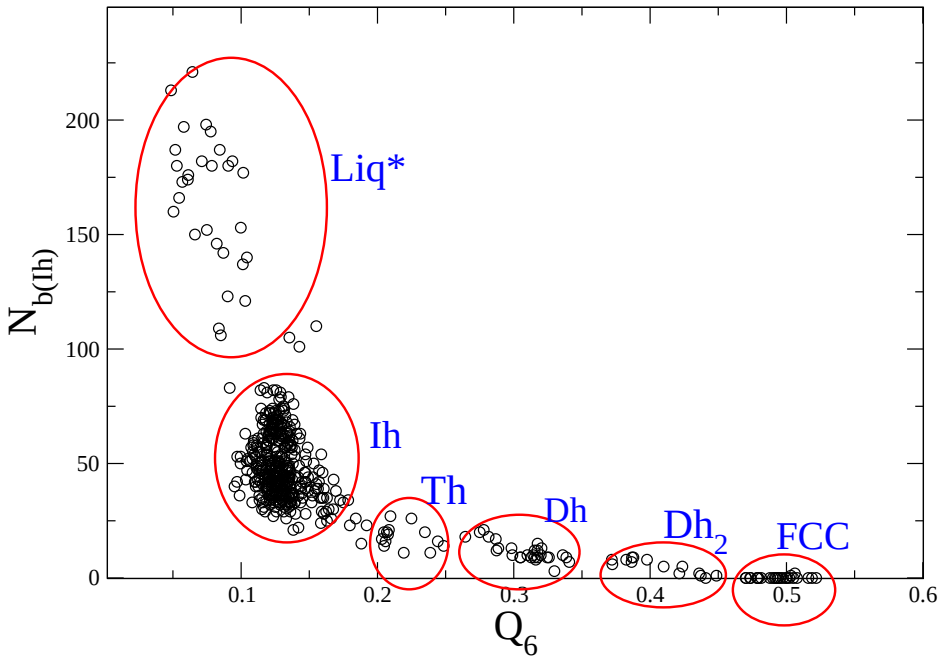

Figure 4.7: $N_{b(Ih)}$ as a function of Q_6 for the final configurations of the $N = 923$ clusters.

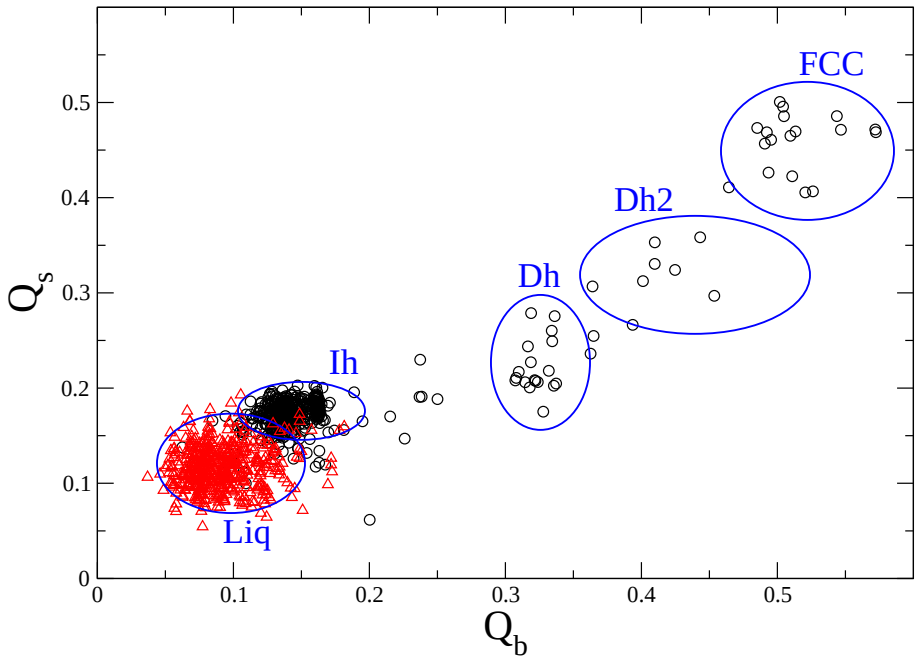

Figure 4.8: Q_s as a function of Q_b for the initial liquid configuration (triangles) and the final configurations (circles) of the $N = 561$ clusters.

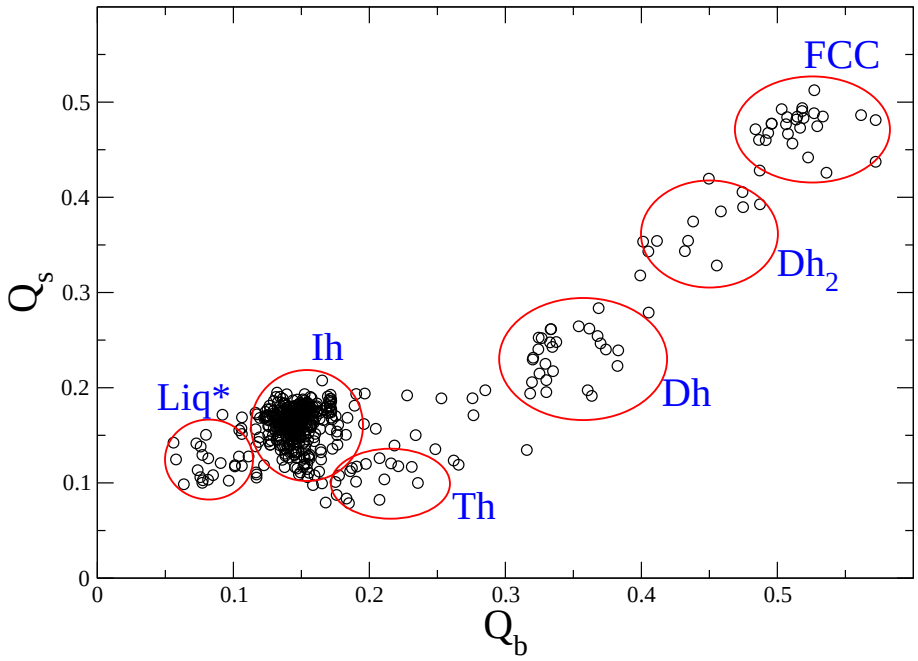

Figure 4.9: Q_s as a function of Q_b for final configurations of the $N = 923$ clusters.

tetrahedron that sits in the core of the nano-cluster and is an example of the poly-decahedral structures that have been observed in larger gold nano-clusters [139].

One of the goals was to see if the structural order parameters and the CNA analysis are able to help identify and distinguish the different frozen clusters. In general, Q_6 alone does a reasonable job of separating out the different solid structure types into distinctive groups, but it is unable to separate liquid clusters from the Ih structures. This last separation can be achieved by introducing $N_{b(Ih)}$, which significantly decreases when the liquid drops freeze. Plots of Q_b vs Q_s were used in a recent study of the freezing of Lennard-Jones clusters [2] to identify core ordered structures. In that study, the Dh, Dh_2 and FCC structures all showed a positive correlation with respect to the two order parameters, but the structures containing tetrahedral subunits in the core were negatively correlated. The same is true here. Relative to the Ih structure, the Th structure has fewer bulk Ih atoms, which increases Q_b, but three of the ordered $\langle 111 \rangle$ surfaces of the core tetrahedron are buried in the core and appear as Hcp planes. These are covered by disordered surface atoms that reduce Q_s, leading to the negative correlation. This suggests that the appearance of a negative correlation between Q_b and Q_s may be indicative of the presence of more complex core ordered structures in other

atomic cluster systems since they tend to have these buried planes covered in disordered atoms.

Finally, it is important to note that the structures observed here are determined by their accessibility from the liquid state, which in turn, is determined by their nucleation barriers. If the barrier to nucleation is too high, then the structure would not be observed on the time scale of our simulations so there may be additional metastable structures that gold particles can form that are not found in this work.

4.4 Nucleation Rates

The probability, P_i, that a cluster type i ($i = Ih, Dh, Dh2, FCC$) nucleates from a liquid drop is calculated from our simulations using only the trajectories that exhibited a freezing event so the small fraction of non-nucleated systems at the end of the simulation time did not count in the ensemble total. Fig. 4.10 shows P_{Ih} and indicates that the icosahedron is the most dominate cluster formed over the range of T and N studied, even though it is not necessarily the most thermodynamically stable structure. However, P_{Ih} decreases with decreasing temperature and increasing cluster size. Within the scatter of our data, $P_{Dh} \approx P_{FCC}$ (fig. 4.11) and both probabilities show the opposite trend to that seen for the Ih clusters. P_{Dh_2} is not shown, but remains approximately constant near 0.015 over the range of conditions studied.

These probabilities can be related to the difference in height of the nucleation free energy barriers between the various processes. Classical nucleation theory (CNT) gives the rate for each nucleation pathway as

$$J_i = A_i \exp\left(-\beta \Delta G_i^*\right), \tag{4.6}$$

where A_i is the kinetic coefficient, ΔG_i^* is the height of the free energy barrier to nucleation, $\beta = 1/kT$ and k is Boltzmann's constant. Taking the ratio of the rates, J_i/J_m, for processes i and m, using eqs. 2.27 and 4.6 and assuming $A_i = A_m$, yields the difference in the barrier heights as

$$\beta \Delta G_{m,i}^* = \beta \left(\Delta G_m^* - \Delta G_i^*\right) = \ln\left(\frac{P_i}{P_m}\right). \tag{4.7}$$

Using eq. 4.7 shows that for $N = 309$, $\beta \Delta G_{FCC,Ih}^* \approx 6$ at $T = 680$K but this decreases to $\beta \Delta G_{FCC,Ih}^* \approx 2$ for $N = 923$. It is important to note that as the Ih structure becomes highly

dominant our ability to accurately measure P_{Dh} and P_{FCC} decreases. Nam et al. [140] also found $\beta\Delta G^*_{FCC,Ih} \approx 5-6$ for $N = 459$ at $T = 770$K, using a direct free energy calculation that involved the use of a global order parameter as the reaction coordinate.

The key element to note from these results is the temperature and size dependencies of P_i, and hence the barrier heights, mirror what is expected in the equilibrium phase diagram of the clusters, which is driven by the competition between the surface free energy and the strain energy associated with the packing of tetrahedral subunits. This suggests, both the surface and the tetrahedral subunit strain energy may play a role in the nucleation barriers.

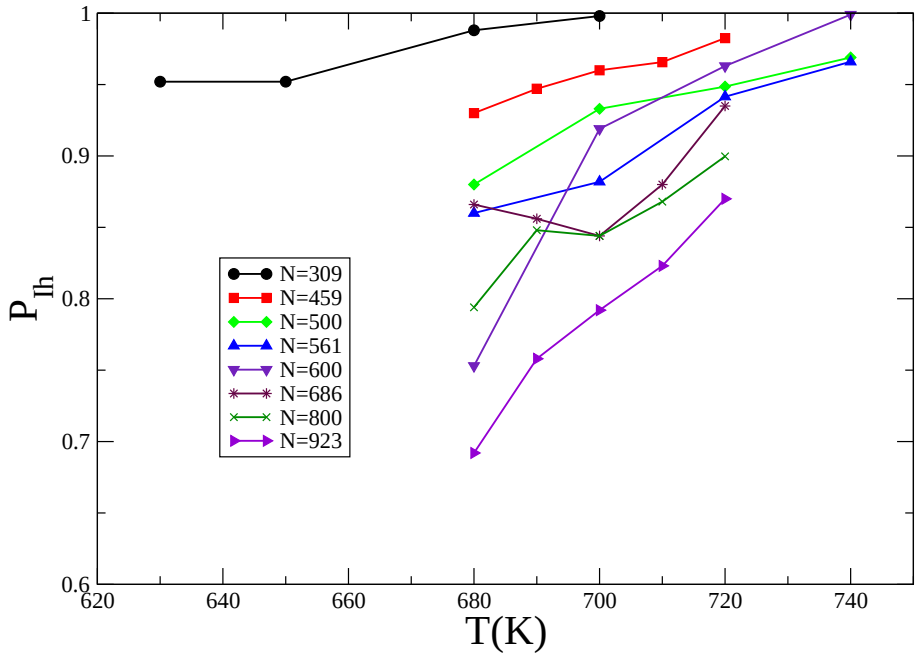

Figure 4.10: T versus P_{Ih} for cluster sizes $N = 309 - 923$

To calculate the individual rates from eqn. 2.27, the overall rate, J, at which the liquid clusters are freezing, must be evaluated. Assuming that nucleation obeys first order kinetics, the rate at which the clusters freeze is given by [1],

$$\ln R(t) = -JV_c(t - t_0), \tag{4.8}$$

where $R(t)$ is the fraction of unnucleated clusters at time t, V_c is the volume of the cluster

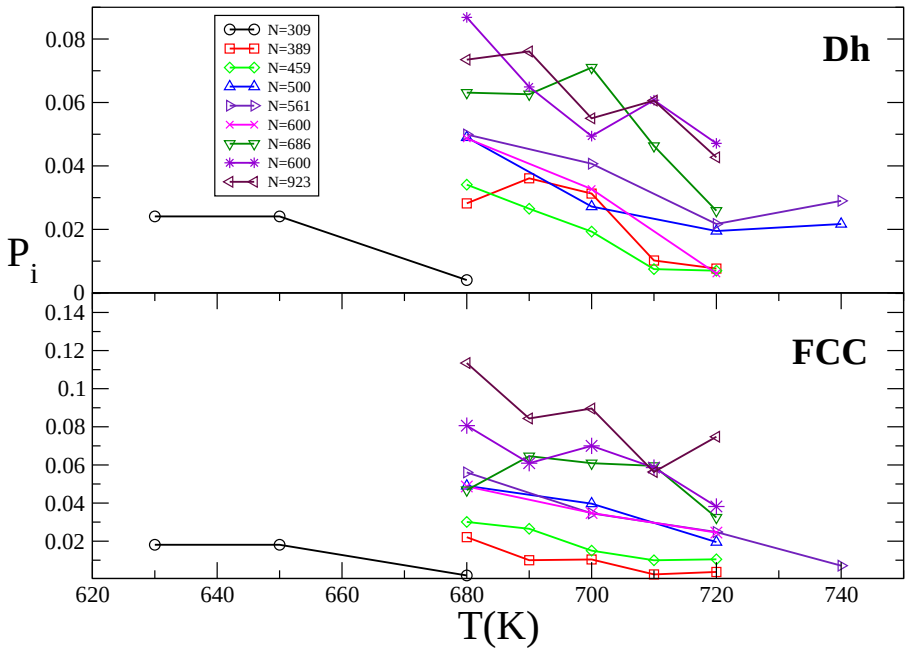

Figure 4.11: T versus P_i for i=Dh (top) and i=FCC (bottom) for cluster sizes $N = 309 - 923$

and t_0 is the lag time. The time to each nucleation event in the ensemble was determined by finding the time at which the energy in the trajectory dropped below a predetermined value of $U_x/N = -3.63\ eV$, that clearly separates the solid states from the liquid drop (see fig. 4.1). Fig. 4.12 is a plot of $\ln R(t)$ vs t, for $N = 561$ at $T = 680K, 700K, 730K$. The slope of the linear part of these plots gives the overall rate, J. Saika-Voivod *et al* [141] showed that, while different methods used in the determination of the nucleation time gave different results for the nucleation times themselves, the rate of nucleation obtained from eqn. 4.8 remained the same. An energy criteria was used here to determine the nucleation times because it is insensitive to the final structure of the nanocluster.

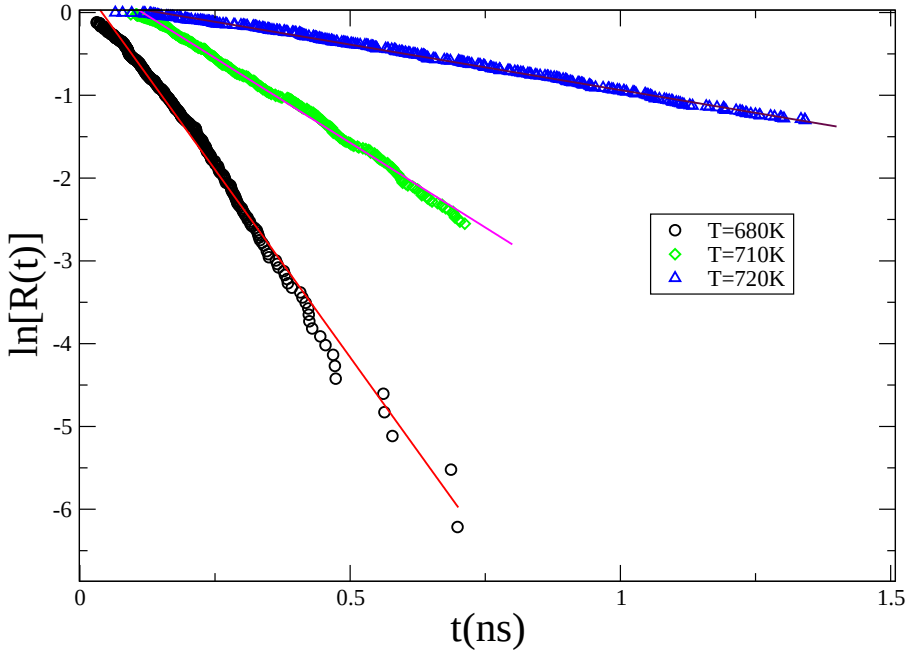

Figure 4.12: Determination of nulceation rate, J, from $R(t_n)$ for $N = 923$ at three different temperatures.

In a bulk, uniform system, the volume term in eqn. 4.8 arises because the nucleation event can occur anywhere with equal probability, thus it accounts for the translational degrees of freedom of the nucleating embryo. There is still considerable debate concerning where nucleation occurs in cluster systems and what role the surface plays as a pseudo-heterogeneous

interface for nucleation [142]. Even if nucleation occurred exclusively in either the surface or the bulk of the droplet, it is not clear how much of the volume or the surface should contribute to the translation degrees of freedom, making it difficult to determine V_c. The volume of these clusters are small and they nucleate to only one structure per drop so the experimental measure used here is the number of droplets forming a given structure. As a result, $V_c = 1$ is used, and the rate is reported in units of the number of clusters per unit time. Furthermore, fig. 4.13(left) shows that rescaling J by the number of atoms per cluster causes all the rates to collapse onto a single rate at low temperatures, although there is still some systematic size dependence which increases at higher T. The rates for the individual structure types (fig. 4.13(right)) show that the Ih rate is an order of magnitude faster than either the Dh or FCC rates for all cluster sizes studied here, but that the difference is decreasing with increasing cluster size and the rates will cross at a larger cluster size.

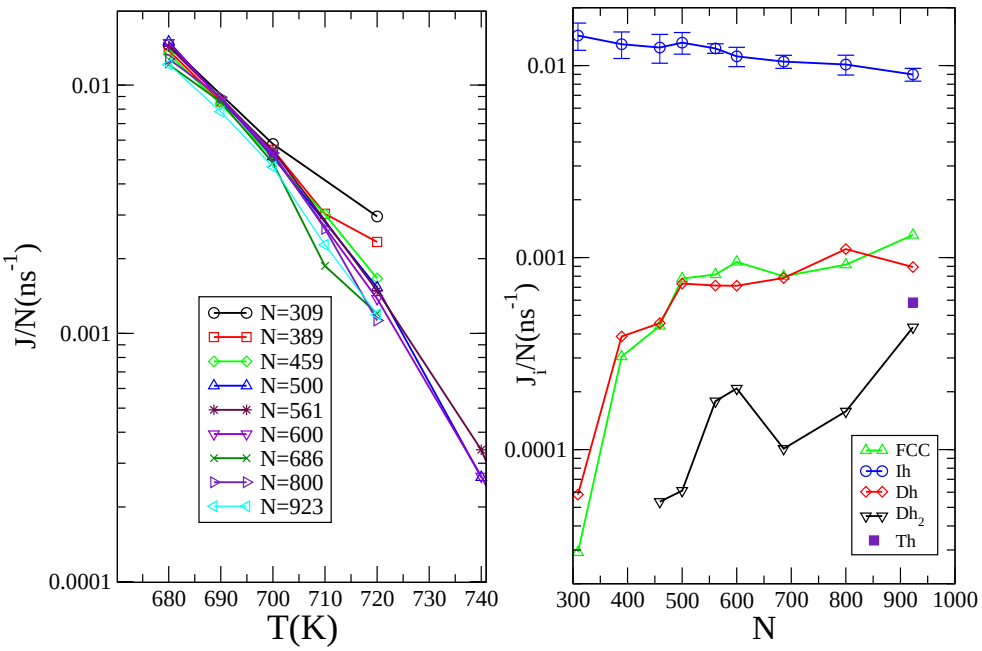

Figure 4.13: (Left) J/N as a function of T for different cluster sizes. (Right) J_i/N, for $i = Ih, Dh, Dh_2, Th, FCC$ as a function of N at $T = 700$K.

4.5 Conclusions

The goal of this chapter was to study the competitive nature of the nucleation which occurs during the freezing of gold nanoclusters and to understand the factors that influence the probabilities of observing the different structures. The results show that non-crystalline Ih is the predominant cluster type formed, and the rate of its formation is significantly faster than Dh and FCC clusters. As the cluster size increases, the probability of Ih clusters forming decreases, while that of Dh and FCC clusters forming increases during the freezing of gold nanoclusters of small to medium sizes. At larger cluster size($N = 923$), there is competition between the formation of FCC and Ih clusters leading to a lower rate for the Ih cluster, and the Th structure, which has been observed in smaller LJ clusters, is observed for the first time in the N=923 cluster. The probability of observing an Ih cluster increases with increasing temperature, while that of P_{Dh} and P_{FCC} decrease. The results show that the probabilities of freezing to different solid structures, which is determined by nucleation barrier and growth kinetics, follow a similar temperature and cluster size dependence as that of the equilibrium free energies of the structures. In the metastable liquid, there is a general ordering of the surface than the core, suggesting that ordering begins at the surface for very small embryos. The next chapter deals with understanding the arrangement of local structures to give the different structures observed in simulation.

Chapter 5

Effective Reaction Coordinates in the Nucleation of Gold Nanoclusters

5.1 Introduction

Recent studies [1, 3, 138] show that gold clusters, freezing from the same conditions, lead to the formation of various motifs such as Ih, Dh and FCC with Ih being the most prevalent. Nam *et al* [138] showed that the surface atoms of liquid clusters are somewhat ordered in a way that resembles the five-fold symmetry facets of the Ih structure and potentially lower the nucleation barrier for this structure relative to the others. Direct calculations of the nucleation barrier to freezing in gold nanoclusters also found that a significant number of the atoms in the critical embryo were located on the surface [45]. However, the study uses a generic solid-like order parameter to identify atoms belonging to the growing embryo and only uses the embryo size to describe the nucleation reaction coordinate. The embryo size is the usual order parameter used to describe nucleation, but by itself, it is unable to distinguish between the nucleation pathways of different structures. In this chapter, the multi-phase maximum likelihood analysis (MPMLA) developed in Chapter 3 is applied to the competitive nucleation of a gold nanocluster of size $N = 561$. The main goal is to identify reaction coordinates describing the formation of the different structures. The aimless shooting algorithm is used to harvest the transition path ensemble which consist of the configurations along the different transition paths. The MPMLA is then used to obtain the most accurate reaction coordinate for each of the major transitions. Finally, the resulting reaction coordinates, obtained in terms of various order parameters, are used to explore and understand the mechanism of nucleation for each of the pathways.

5.2 Simulation Details

5.2.1 Aimless Shooting

In order to perform the MPMLA, the transition path ensemble (TPE) and the transition path probabilities are required. These can be obtained using the aimless shooting method in a multi-state transition path sampling. The aimless shooting used here is similar to the one used in Chapter 3, but implemented through molecular dynamics. To harvest the TPE for this system, the aimless shooting is performed on 300 initial shooting points. To obtain these initial shooting points, 500 liquid gold nanoclusters at $1000K$ are cooled to $700K$ by a spontaneous jump in the temperature, which involved assigning each atom a random velocity from a uniform distribution appropriate for $T = 700K$ using the EAM potential[125]. The configurations are saved along the trajectories after every 500 timesteps. The maximum embryo size, which will be defined later, is evaluated using the saved configuration. The initial shooting configurations are chosen from trajectories that exhibit a freezing event indicated by a sudden drop in U_x/N and a sharp increase in n. Fig. 5.1 is a plot of the size evolution for five different trajectories. The green arrows indicate the beginning point for increase in n where the shooting points are picked from, up to the green dash line. A total of 300 shooting points were used, 20 leading to the Ih structure, 110 leading to the Dh structure, 50 leading to the Dh_2 structure and 120 that lead to the formation of the FCC structure. The initial velocities of the chosen configuration are drawn from the Maxwell-Boltzmann distribution for the selected temperature. The configuration is then propagated forward and backward in time using a molecular dynamics scheme, that integrates the equations of motion by way of the velocity Verlet algorithm, with a time step, $\Delta t = 2.8\ fs$. The backward trajectory is initiated by multiplying the velocities of the particles by -1. The forward and backward trajectories are stopped when a stable basin is reached. The trajectory is reactive if the forward and backward propagations end in different basins and are non-reactive otherwise. The shooting points are saved with the information describing the basins where the forward and reverse trajectories end. If the shooting trajectory is accepted as reactive, a new shooting point is chosen along it from $\mathbf{x}_{-\delta t}, \mathbf{x}_0, \mathbf{x}_{+\delta t}$ with equal probability. $\mathbf{x}_0$ is the original configuration of the shooting point on the reactive trajectory, $\mathbf{x}_{-\delta t}$ and $\mathbf{x}_{+\delta t}$ are configurations with number of time steps, δt, before and after the previous shooting point. After every 50 shooting points,

the acceptance ratio is evaluated. If the acceptance ratio is less than 40%, δt is reduced by 100 time steps . This helps to maintain an acceptance ratio of between $40\% - 75\%$, though some of the trajectories were not able to attend such an acceptance ratio. The initial timesteps, δt, was chosen as 500. For each of the initial trajectories, 300 shootings were made, thus giving our TPE a size of 9.0×10^4 points.

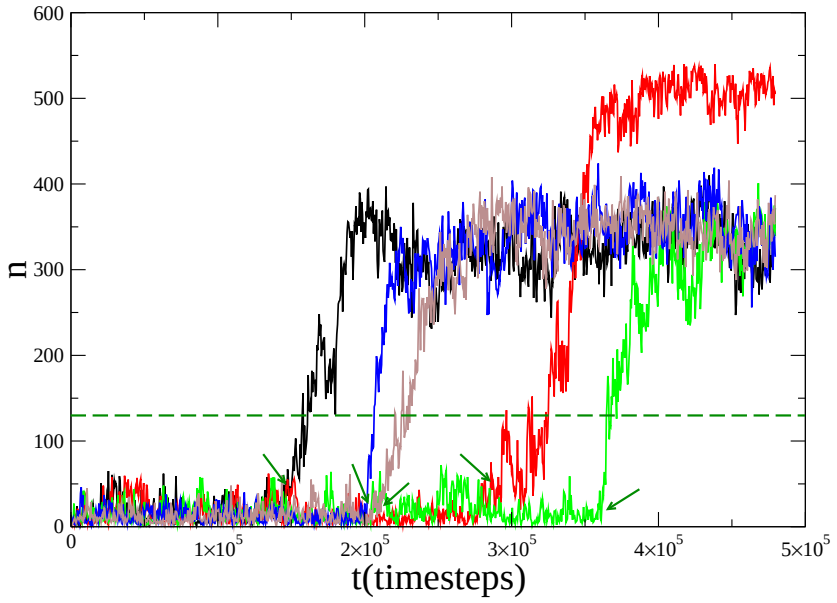

Figure 5.1: A diagram showing cluster size,n, along different trajectories used in picking initial shooting points. The arrows point to points where the initial shooting configurations were picked from.

5.2.2 Structural Basin Identification

The major advantage of the aimless shooting algorithm is that it does not require a pre knowledge of the reaction coordinate of the system. All that is required is to identify correctly when a product or reactant is reached during the simulation. For a system with many products, some closely related, a rigorous definition of the product basins is a major factor in performing an accurate sampling. The structural identification in the previous chapter used a 2-dimensional correlation of the order parameters. To make sure that the basins are not

on the path to another basin, we define each of them as an ellipsoid,

$$\frac{x^2}{a1^2} + \frac{y^2}{b1^2} + \frac{z^2}{c1^2} = 1, \tag{5.1}$$

where $x = Q_6 - \hat{Q}_6$; $y = Q_b - \hat{Q}_b$; $z = Q_s - \hat{Q}_s$. The mean values $\hat{Q}_6, \hat{Q}_b$ and $\hat{Q}_s$, are the values of the Q_6, Q_b and Q_s defining the coordinates of the center of the ellipsoid for a given products. Their values were obtained using unquenched trajectories that ended in each of the products during the initial freezing events described in subsection 5.2.1. Therefore, there are five different values of $\hat{Q}_6$ representing the liquid state, icosahedral, decahedral, off-centered decahedral and FCC structures. Q_6, Q_b and Q_s are the values of these order parameters obtained along the trajectory. $a1, b1$ and $c1$ are the semi-principal axes of the ellipsoid. Their values determine the width of a product basin. At any point along the aimless shooting trajectory, if the expression

$$\frac{(Q_6 - \hat{Q}_6)^2}{a1^2} + \frac{(Q_b - \hat{Q}_b)^2}{b1^2} + \frac{(Q_s - \hat{Q}_s)^2}{c1^2} \leq 1, \tag{5.2}$$

is true, the trajectory is considered to have entered the respective product basin. Table 5.1 shows the values of $\hat{Q}_6, \hat{Q}_b, \hat{Q}_s, a1, b1$ and $c1$ used for the identification of the different structures. Fig. 5.2 shows the different structural basins. The points represent the end configurations from different freezing trajectories. The different ellipsoids define the region for each of the structures, and are constructed using data in Table 5.1.

Structure	$\hat{Q}_6$	$\hat{Q}_b$	$\hat{Q}_s$	$a1$	$b1$	$c1$
Liquid	0.0423	0.0642	0.0636	0.041	0.044	0.034
Ih	0.112	0.126	0.129	0.044	0.042	0.056
Dh	0.238	0.281	0.168	0.042	0.048	0.034
Dh_2	0.303	0.354	0.232	0.045	0.041	0.030
FCC	0.384	0.447	0.325	0.051	0.074	0.050

Table 5.1: Mean values of Steinhardt order parameters and semi-principal axes used to identify the product basins.

To ensure that the basins identified are well defined, a second set of order parameters based on the cluster neighbour analysis (CNA)[134, 135] which identifies the local structure around a given atom as discussed in Chapter 4 are also used. The number of atoms in a cluster with

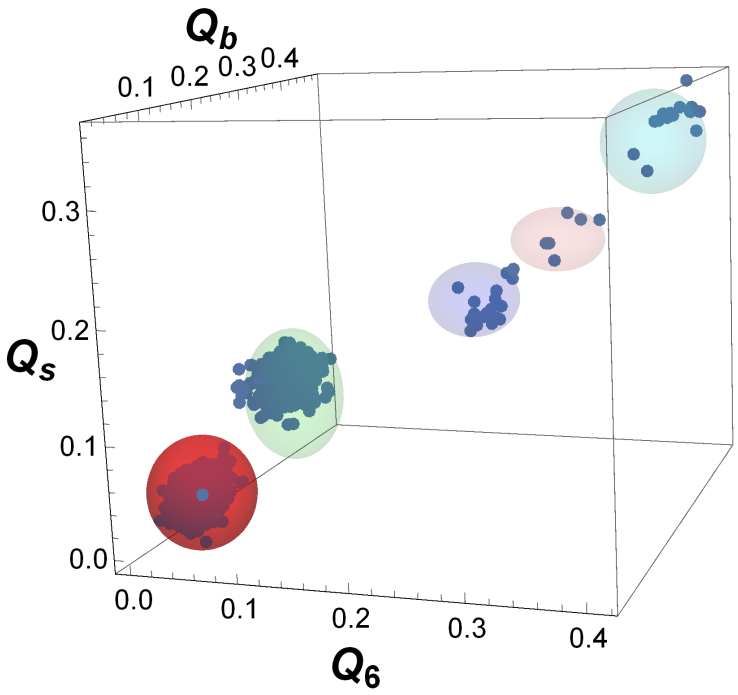

Figure 5.2: Identification of the different structural basins with ellipsoids constructed using data from Table 5.1. Red ellipsoid represent the metastable liquid, light green is for Ih, blue is for Dh while pink and cyan are for Dh_2 and FCC, respectively. The points are the end configurations from different freezing trajectories.

a given CNA environment is related to the global structure of the cluster. For example, the number of bulk icosahedral atoms (N_{bIh}) in a perfect icosahedral cluster ($N = 561$) is 49, while the same quantity in a perfect FCC cluster is zero. The number of icosahedral edge atoms (N_{Ihedge}), provides a measure of the surface ordering in the Ih and Dh structures and is highest in the Ih clusters, medium in the Dh clusters and zero in both the FCC and liquid clusters. The final parameter used is the number of bulk fcc atoms, N_{bfcc}. Therefore, the second expression for a product basin is given as,

$$\frac{(N_{bIh} - \hat{N}_{bIh})^2}{a2^2} + \frac{(N_{bfcc} - \hat{N}_{bfcc})^2}{b2^2} + \frac{(N_{Ihedge} - \hat{N}_{Ihedge})^2}{c2^2} \leq 1, \tag{5.3}$$

where $\hat{N}_{bIh}$, $\hat{N}_{bfcc}$, and $\hat{N}_{Ihedge}$ are the mean values of the number N_{bIh}, N_{bfcc} and N_{Ihedge} in the different structures. Table 5.2 shows the values of $\hat{N_{bIh}}$, $\hat{N_{bfcc}}$, $\hat{N_{Ihedge}}$, $a2, b2$ and $c2$ used in the second identification. $\hat{N_{bIh}}$, $\hat{N_{bfcc}}$, and $\hat{N_{Ihedge}}$ are the coordinates of the centers of the ellipsoid representing the different product basins, while $a2, b2$ and $c2$ are the semi-principal axes of the ellipsoid. During the aimless shooting, when a given configuration is identified as belonging to a given basin using the two sets of parameters above, then it is accepted to that basin and the trajectory ends, otherwise the shooting continues.

Structure	$\hat{N_{bIh}}$	$\hat{N_{bfcc}}$	$\hat{N_{Ihedge}}$	$a2$	$b2$	$c2$
Liquid	70	10	6	50	12	7
Ih	34	70	36	24	25	18
Dh	10	155	20	8	28	10
Dh_2	6	171	0	5	30	4
FCC	0	180	0	4	34	4

Table 5.2: Mean values of order parameters from CNA and their corresponding semi-principal axes used to identify the product basins.

5.2.3 Test Order Parameters

The configurations obtained from the aimless shooting are evaluated using order parameters, which are then used in a multi-path maximum likelihood analysis to construct the reaction coordinates. The most commonly used order parameter in nucleation studies is the embryo

size. Two different embryo criteria are used in this study. The first definition uses the local bond order parameters to distinguish between liquid-like and solid-like atoms. It is based on the Steinhardt order parameters and has been used extensively in the study of nucleation in both bulk[2, 3] and nano particle systems[44]. This is achieved by considering the correlation of the structure surrounding particle i with the structure surrounding each of its neighbors. The local structure around neighbouring atoms is highly correlated in a solid structure, but it is less correlated in a liquid. To measure the degree of correlation of the structure of atoms i and j, a scalar product is used;

$$s_{ij} = \sum_{m=-6}^{6} \tilde{q}_{6m}(i)\dot{\tilde{q}}^{*}_{6m}(j). \tag{5.4}$$

Here,

$$\tilde{q}_{6m}(i) = q_{6m}(i)/\sum_{m} q_{6m}(i), \tag{5.5}$$

where,

$$q_{6m}(i) = \frac{1}{N_{nb}} \sum_{j=1}^{N_{nb}(i)} Y_{6m}(\mathbf{r}_{ij}). \tag{5.6}$$

$\tilde{q}_{6m}(j)$ is the normalized q_{6m}, and $\tilde{q}^{*}_{6m}(j)$ is the complex conjugate of $\tilde{q}_{6m}(j)$, N_{nb} is the number of nearest neighbors of atom i, $Y_{lm}(\mathbf{r}_{ij}) = Y_{lm}(\theta(\hat{r}), \phi(\hat{r}))$ is a spherical harmonic function where the angles θ and ϕ, measured from an arbitrary coordinate reference, defined by the radial vector between atoms i and j. The value of s_{ij} is close to unity when the atoms are in the same environment and very small otherwise. This helps in the identification of ordered atoms in the embryo. A threshold above which two atoms are regarded as being in the same environment is the threshold dot product, s_{min}. The value of s_{min} was determined for gold nanoclusters by considering the distribution of s_{ij} in the liquid and solid phases of a 3892-atom gold cluster[143]. Low values of s_{ij} had higher frequencies within the liquid phase, while in the solid phase, high values of s_{ij} had higher frequencies. $s_{min} = 0.65$ was chosen as the point within the solid phase close enough to the point where the two distributions cross each other. Two particles i and j are then said to be correlated if the $s_{ij} \geq s_{min}$ and the bond between them is termed a solid bond. An atom is considered to be a solid atom if it is connected to more than 50% of it neighbors with a solid bond. Finally, two solid atoms are considered to be part of the same embryo if they are connected by a solid bond. The largest embryo containing solid atoms is regarded as the largest embryo size, n.

The second embryo criteria uses the local crystallinity defined by the CNA. CNA identifies the local environment of the atoms and labels them as fcc, Hcp, Ih, $< 111 >$, $< 100 >$, $fcc-edge$, $Ih-edge$, $Ih-join$, $Ih-vertex$ or amorphous. For the purpose of this embryo definition, all local environments except the amorphous are regarded as solid-like. If two solid-like atoms i and j are nearest neighbors, then they are regarded as being connected by a solid bond. The largest connected cluster is termed the CNA embryo with size, n_{CNA}. For both embryo criteria, two atoms are regarded as neighbors if the distance between them is less the or equal to $r_b = 3.5$ $\mathring{A}$, which is the radius corresponding to the first minimum of the radial distribution function for gold.

Another set of order parameters tested include the Steinhardt bond order parameters, such as Q_6, W_4 and W_6, which are calculated globally for the entire cluster. Others are the different variants of Q_6, such as Q_b where the bulk atoms are used to calculate the Q_6, and, Q_s, which is the Q_6 of all atoms on the surface of the cluster. The calculations of Q_6, Q_b, and Q_s are described in subsection 4.2.2. Another variant of Q_6 used as a test order parameter is the Q_e, which is the Q_6 calculated by using atoms in the largest solid embryo[16] alone,

$$Q_e = \sqrt{\frac{4\pi}{13}\sum_{m=-6}^{6}|\frac{1}{n}\sum_{i=1}^{n}Q_{6m}|^2}, \tag{5.7}$$

where

$$Q_{6m}(i) = \frac{1}{N_{nb}}\sum_{j=1}^{N_{nb}(i)}Y_{6m}(\mathbf{r}_{ij}), \tag{5.8}$$

with the restriction that i and j must be in the largest embryo and connected by a solid bond.

The order parameter, W_l, which was first used by Desgranges and Delhommelle[144] to distinguish between different crystal structures, is defined as follows: For a given particle, i,

$$w_l(i) = \frac{\sum_{m_1+m_2+m_3=0}\begin{pmatrix} l & l & l \\ m_1 & m_2 & m_3 \end{pmatrix} q_{lm_1}(i)\times q_{lm_2}(i)\times q_{lm_3}(i)}{(\sum_{m=-l}^{l}|q_{lm}(i)|^2)^{3/2}}, \tag{5.9}$$

where the integers m_1, m_2 and m_3 run from $-l$ to $+l$, but only the combinations with $m_1 + m_2 + m_3 = 0$ are allowed. The matrix $\begin{pmatrix} l & l & l \\ m_1 & m_2 & m_3 \end{pmatrix}$ is the Wigner-3j coefficients. w_l determines the local crystallinity around each individual particle. To identify the crystal

structure of the entire cluster the average value of w_l is taken as,

$$W_l = \sqrt{\frac{4\pi}{2l+1}\sum_{m=-l}^{l}|\frac{1}{N}\sum_{i=1}^{N}w_{lm}(i)|^2}. \tag{5.10}$$

The values, $l = 4$ and $l = 6$ are chosen due to their sensitivity to cubic and hexagonal symmetries, respectively. Steinhardt *et al* [14] showed that the W_l's are very sensitive to different symmetries and can be used to identify different cluster types base on their values. The average values for W_6 and W_4 were calculated for gold nanoclusters [15] and are given in Table5.3

Structure	W_4	W_6
Liquid	0.00	0.00
Ih	-0.15932	-0.16975
FCC	-0.15732	-0.01316

Table 5.3: Average bond order parameters for liquid, Ih and FCC structures.

The local environments of the atoms are often organized into larger scale features in the non-crystallographic clusters. For example, the lines of Ih atoms surrounded by planes of Hcp atoms appearing in both the Ih and Dh clusters. To capture and understand the role these structures play in the nucleation process, a structural correlation parameter, $S_{a-b}(i)$, is defined as the number of nearest neighbors of an atom, i, in local environment a, which have environment b. For example, if a bulk Ih atom is surround by five *hcp* atoms, $S_{Ih-hcp} = 5$. $\hat{S}_{a-b}$ is the average over all the particles with local environment a in the largest embryo. A similar parameter has been used to study the evolution of a solid phase from its metastable liquid phase[145, 146, 147], but the atoms were not identified based on their local CNA environment. The present work focuses on understanding the correlation between the different structural environments of the particles as identified by CNA. Fig. 5.3 shows a representation of how the parameter $S_{a-b}(i)$ is defined. The cut-off radius beyond which particles are no longer regarded as nearest neighbors is $r_b = 3.5$ $\mathring{A}$. The green particles all have the same local environment which is different from that of the red particles. For particle i, all the particles within the orange circle are the neighbors, but only the green ones are counted. From the example shown in fig. 5.3, i has 5 neighbors, but $S_{i-i} = 4$. This parameter provides

a molecular view of how the local structure of an atom is correlated with the neighboring atoms in the largest embryo. The choice of a and b local environments is such that the value of $\hat{S}_{a-b}$ is close to zero in the liquid phase, but increases to a unique value in the solid phase. For example, the bulk fcc atoms with the nearest neighborhood of another bulk fcc, $\hat{S}_{fcc-fcc}$, is 3 and 12 for a perfect Ih and FCC structures, respectively. The values of these parameters are cluster size dependent. For example, $\hat{S}_{fcc-fcc} = 3$ for a perfect Ih for the system size, $N = 561$ only. For the non-crystalline structures with characteristic five-fold symmetry, five planes of Hcp atoms surround a single line of bulk Ih atoms. Hence for such structures, $\hat{S}_{Ih-Hcp} = 5$, while it is zero for a perfect FCC cluster.

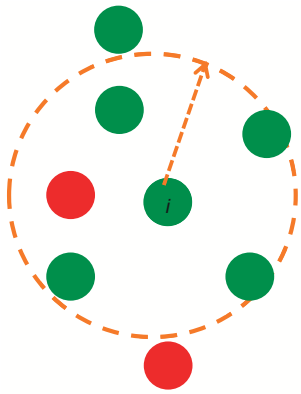

Figure 5.3: A diagram showing how $S(i)$ is constructed using the local environment of the nearest neighbors of particle i. All the atoms within the orange circle are the nearest neighbors. All the green atoms have the same local environment as identified using CNA, while the red atoms are in a different environment from the green ones.

5.3 Results and Discussions

First, the liquid to solid transition in gold nanoclusters is studied without any separation into the different structural phases. The different structures are regarded as one solid phase, thereby giving a two state system. The two state maximum likelihood analyses using both the committor model

$$p_{sol}(r) = \frac{1}{2}(1 + tanh(r)) \tag{5.11}$$

and the transition path probability model,

$$P_{liq \rightarrow sol}(TP|r) = p_0(1 - tanh^2(r)), \tag{5.12}$$

are performed independently. For each of the parameters used, or their combination, the critical condition is obtained by solving the expression,

$$p_{sol}(r) = 1/2. \tag{5.13}$$

Table 5.4 is a summary of the likelihood analysis using eqn. 5.11 for the *liquid* $\rightarrow$ *solid* transition, showing the likelihood estimate and the critical conditions for the different test order parameters. The maximum embryo size which is often used as the reaction coordinate in the studies of *liquid* $\rightarrow$ *solid* nucleation is better than every single parameter. It gives a critical size, $n^* = 153$ for the system size studied. Fig. 5.4 shows the committor probability and transition path probability as a function of n. It also shows the models used. When a combination of the order parameters was made, the results show that the sum of the embryo size, n, and Q_e is the best reaction coordinate. Moroni *et al*[17] showed, using MLA, that the product of n and Q_e is the best reaction coordinate to study the freezing of Lennard-Jones particles. Fig. 5.5 shows the committor probability and transition path probability as a function of $r = n \times Q_e$ for our system and their models. The models do not fit well to the data especially for $r < 25$. The manner of the combination of these two parameters are different from that of Moroni *et al*[17], but they appear to offer the best understanding of the liquid-solid transition in nanoclusters. This result is only valid for a liquid-solid transition that does not recognize the different structures.

Order Parameters	Reaction Coordinates (r)	$LE_{\alpha max}$	r^*
n_{CNA}	$0.0118n_{CNA} - 1.011$	-49945	$n^* = 98$
n	$0.0095n - 1.568$	-45776	$n^* = 153$
Q_6	$15.0476Q_6 - 1.6927$	-48906	$Q_6^* = 0.1125$
Q_b	$10.8839Q_b - 1.6697$	-47718	$Q_b^* = 0.1534$
Q_s	$14.6694Q_s - 1.6549$	-56103	$Q_s^* = 0.1128$
Q_e	$1.2961Q_e - 0.1279$	-47650	$Q_e^* = 0.099$
$n + Q_e$	$0.0101n + 3.0781Q_e - 2.533$	-44488	$Q_e = 0.8231 - 0.0032n$
$n \times Q_e$	$0.0299nQ_e - 1.3114$	-44504.5	$nQ_e^* = 43.76$

Table 5.4: Test order parameters and their performance as reaction coordinate for liquid$\rightarrow$solid transition in gold nanoclusters. $BIC = (1/2)lnN_R = 5.499$.

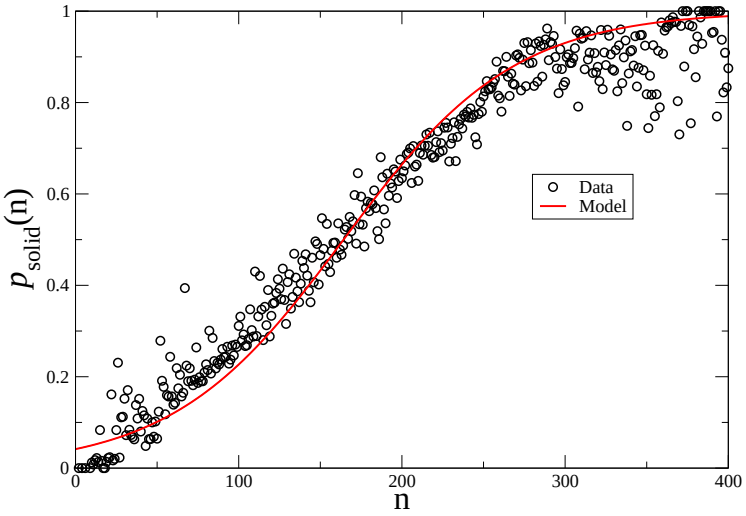

(a) Committor probability

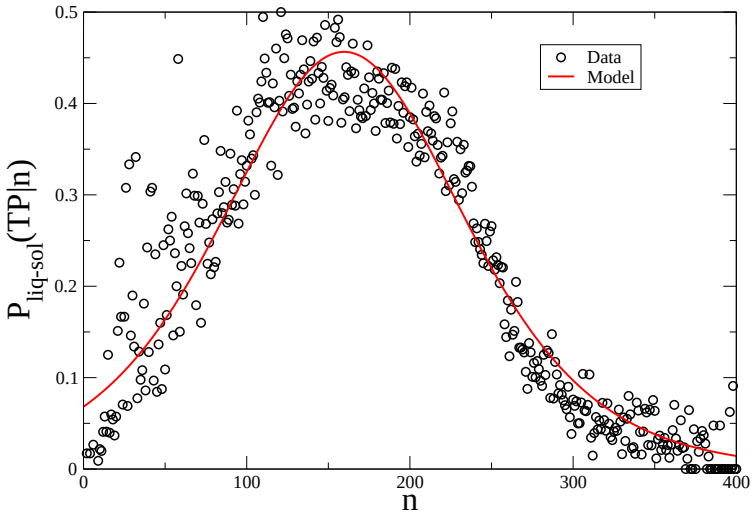

(b) Transition path probability

Figure 5.4: Aimless shooting data for liquid → solid transitions compared to (a) $P_{sol}(r(n))$ and (a) $P(TP|r(n))$.

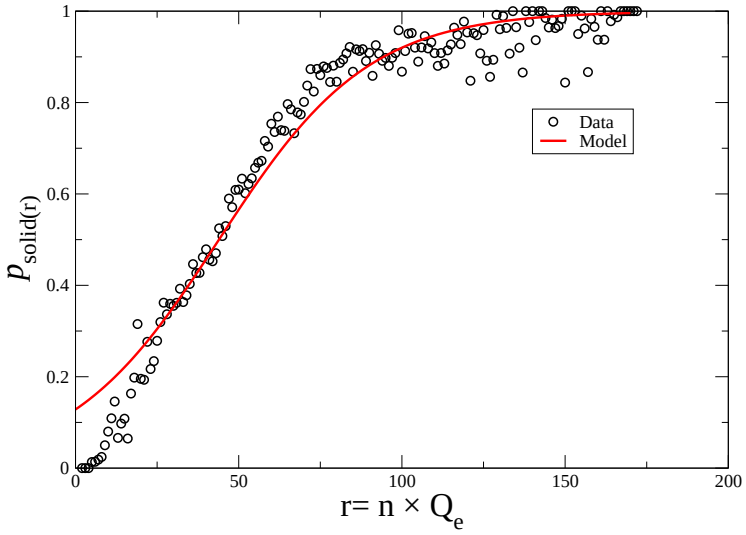

(a) Committor probability

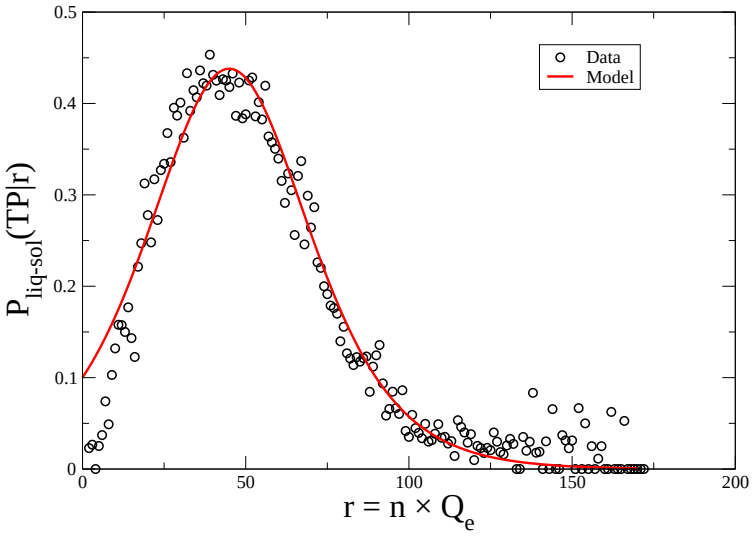

(b) Transition path probability

Figure 5.5: Aimless shooting data for liquid → solid transitions compared to (a) $P_{sol}(r)$ and (b) $P(TP|r)$, where $r = n \times Q_e$

The extent to which the maximum likelihood analysis provides an accurate reaction coordinate can be determined by evaluating the probability that configurations on the transitions state, r^*, have equal chance of growing or shrinking. If the given reaction coordinate is a good reaction coordinate, the committor probability distribution would have a maximum at 0.5. Fig. 5.6 shows the p_{solid} distributions for configurations lying on transition states based on two reaction coordinates, where p_{solid} denotes the probability of a configuration ending in the solid phase. For the distributions in fig. 5.6(a), 120 configurations are selected on or close to the region $nQ_e^* = 43.76$. For each configuration, 100 trajectories are run and the committor probability is evaluated as the ratio of trajectories ending in the solid phase. As seen from the histogram, the peak is at $p_{solid} = 0.6$, though not very different from that of $p_{solid} = 0.5$. For fig. 5.6(b), 270 configurations are drawn from configurations lying on or close to the line $Q_e = 0.8231 - 0.0032n$. This distribution clearly shows a peak at $p_{solid} = 0.5$ confirming that $r = 0.0101n + 3.0781Q_e - 2.533$ is an accurate estimate of the reaction coordinate for liquid-solid transition for gold nanoclusters.

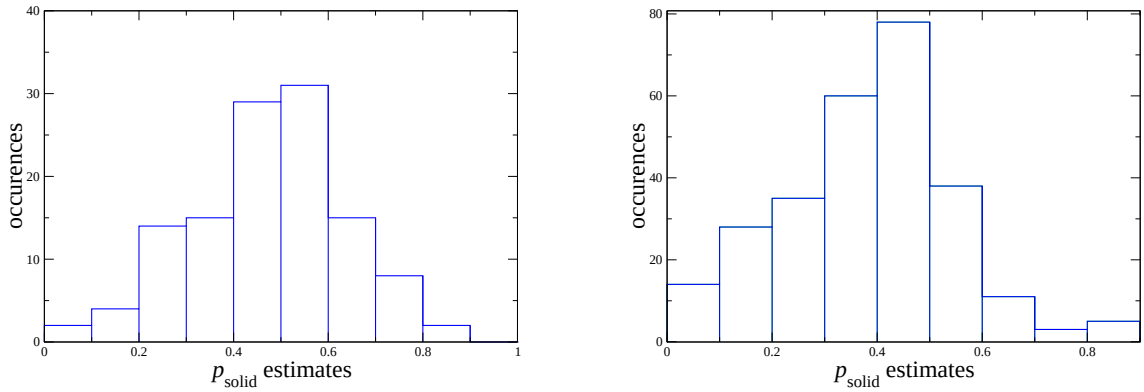

(a) $r = 0.0299nQ_e - 1.3114$ (b) $r = 0.0101n + 3.0781Q_e - 2.533$

Figure 5.6: Committor probability distributions for two reaction coordinates obtained from the maximum likelihood analysis.

The transition path probabilities were calculated using different order parameters for the transitions to the different structural phases. Fig. 5.7(a) shows that the probability of a configuration to be on the Liq→Ih transition path as a function of size is an order of magnitude higher than that of other transition paths. This result is consistent with previous

calculations[3, 1], where the probability of seeing an icosahedral structure during the simulation of gold nanoclusters was higher than others . In fig. 5.7(b), we see that the probabilities of solid → solid rearrangement increase after the critical size. Using High Resolution Electron Microscopy to study the formation of gold nanoclusters, Koga *et al*[31] observed that there is a solid→solid transition below the melting point for the gold nanoclusters they studied. The increase in the transition path probabilities beyond the critical size supports this experimental observation of solid→solid transitions. The committor probabilities for the different liquid to solid transitions as a function of different order parameters is also calculated. Fig. 5.8 shows the committor probability to the different phases as a function of (a) Q_e and (b) $\hat{S}_{fcc-fcc}$. All the committors except P_{FCC} do not possess the basic feature of a committor, that is, having a value of zero in the liquid phase and a value of one in the solid phase. As stated earlier, it is only a committor with this feature that can describe a transition accurately. With many phases, as seen in the system studied, as the probability of committing to a particular phase increases, the probability of committing to other phases reduces. For example, the committor probability for Ih increases as the configuration $\mathbf{x}$ approaches the Ih basin. It becomes maximum when it is in Ih product basin, but as it moves away the probability reduces while the probability of committing to another structure increases. This causes the bell shape of the committor probabilities, except the committor to the FCC. For most of the tested order parameters, FCC has the highest or the least value. No other structure is seen beyond after FCC, such that there is no decline in P_{FCC} when its maximum value is attained. For a complex system with many products, one method that can aid the understanding of the transitions is the transition path sampling with the maximum likelihood analysis of the transition path probabilities. Next, the multi-phase maximum likelihood analysis is performed for the different transitions in order to understand the mechanism for the formation of the different structures.

5.3.1 Icosahedral Structure

All the order parameters are tested as reaction coordinates for the nucleation of the icosahedral structure from metastable liquid. A summary of some of the single order parameters and their likelihood estimate is contained in Table 5.5. For all the single order parameters, $\hat{S}_{fcc-fcc}$ describes the liquid →Ih transition better than others, based on the likelihood esti-

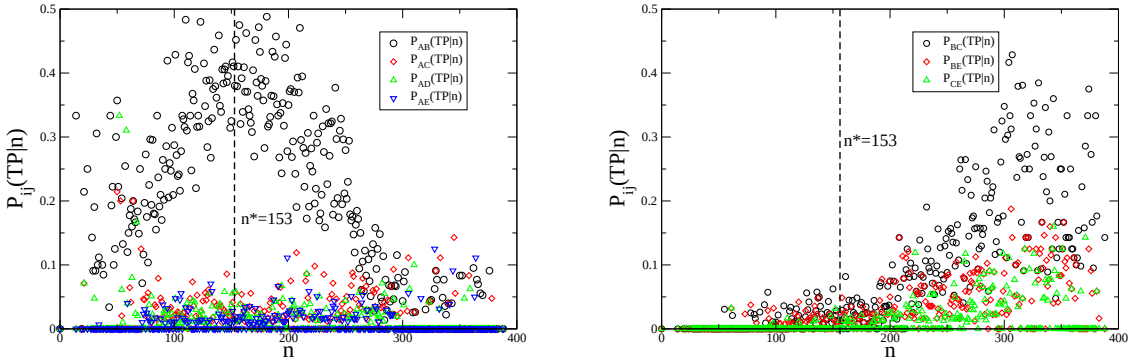

(a) liquid → solid transitions

(b) solid → solid transitions

Figure 5.7: The transition path probabilities for (a) liquid - solid and (b) solid-solid transitions. In the plots, A=Liquid, B=Icosahedral,C=Decahedral,D=Off-centered Decahedral, E=FCC.

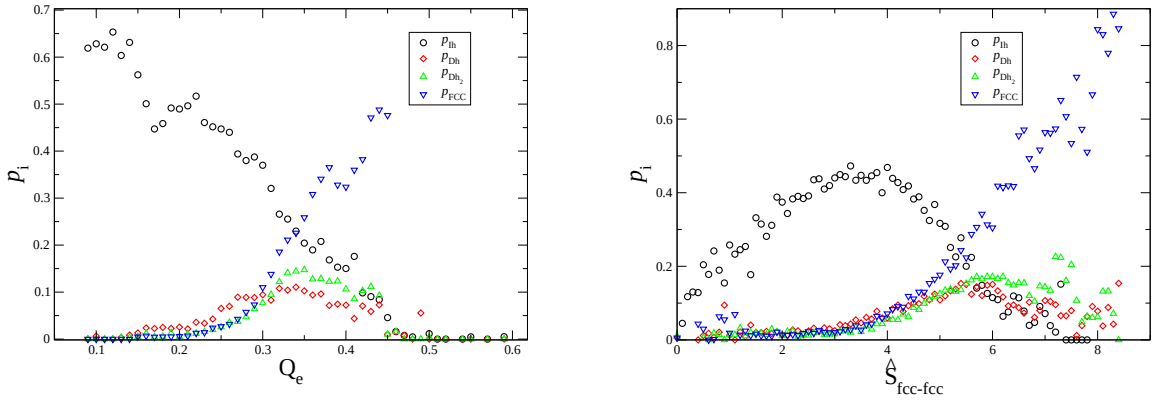

(a)

(b)

Figure 5.8: The committor probabilities to the different phases as a function (a) Q_e, (b) $\hat{S}_{fcc-fcc}$.

mates. Since the major feature of the icosahedron is the five-fold symmetry, intuition would suggest that parameters ($\hat{S}_{Ih-Ih}$ and $\hat{S}_{Ih-hcp}$) that measure the formation of these five-fold symmetries will be more important. Fig. 5.9(a) shows the transition path probability as a function of $\hat{S}_{fcc-fcc}$, while fig. 5.9(b) shows $P_{AB}(TP|\hat{S}_{Ih-Ih})$ and $P_{AB}(TP|S_{Ih-hcp})$ with the models describing them. The model describing $P_{AB}(TP|\hat{S}_{fcc-fcc})$ fits well with the data. An icosahedron is made of 20 tetrahedral subunits that all share one vertex atom at the center of the cluster. Each tetrahedron has a core made from fcc ordered particles and shares three interfaces with its neighboring tetrahedra. The interface shared by the tetrahedra is constructed from a plane of hexagonally close packed (Hcp) particles connected to the bulk icosahedral (Ih) particles. The maximum in $P_{AB}(TP|\hat{S}_{fcc-fcc})$ occurs when $\hat{S}_{fcc-fcc} \sim 3.0$, (see fig. 5.9a), which corresponds to the formation of a tetrahedron for the $N = 561$ icosahedron. $\hat{S}_{Ih-Ih}$ measure how the bulk Ih atoms align themselves with each other, while, $\hat{S}_{Ih-hcp}$ measure how the bulk Hcp atoms are arranged around the bulk Ih atoms giving the five-fold symmetry. The models describing $P_{AB}(TP|\hat{S}_{Ih-Ih})$ and $P_{AB}(TP|\hat{S}_{Ih-hcp})$ do not fit the data well. Although the model for $\hat{S}_{Ih-Ih}$ peaks near 2 which is expected of a linear chain of bulk Ih atom, the scatter in the data could be due the presence of some bulk Ih atoms in the amorphous section of the cluster.

Order Parameters	Reaction Coordinates (r)	$LE_{\alpha max}$	r^*
n	$0.0111n - 1.7322$	-44479.1	$n^* = 156.17$
Q_e	$6.1701Q_e - 0.8124$	-45567.1	$Q_e^* = 0.1317$
$\hat{S}_{Ih-hcp}$	$0.3915\hat{S}_{Ih-hcp} - 0.9217$	-48766.1	$\hat{S}^*_{Ih-hcp} = 2.354$
$\hat{S}_{fcc-fcc}$	$0.5320\hat{S}_{fcc-fcc} - 1.4562$	-44190.6	$\hat{S}^*_{fcc-fcc} = 2.737$
$S_{vert-edge}$	$0.3732\hat{S}_{vert-edge} - 1.1614$	-48097.7	$\hat{S}^*_{vert-edge} = 3.112$
$\hat{S}_{edge-<111>}$	$0.2674\hat{S}_{edge-<111>} - 0.6923$	-49008.3	$\hat{S}^*_{edge-<111>} = 2.588$
$\hat{S}_{Ih-Ih}$	$0.3235\hat{S}_{Ih-Ih} - 0.9319$	-48906.6	$S^*_{Ih-Ih} = 2.880$

Table 5.5: Different single order parameters tested for liquid→Ih transitions in gold nanocluster. $BIC = (1/2)\ln N_R = 4.942$.

The order parameters are also examined along a number of freezing trajectories that begin in the liquid phase and end in the Ih structure. Fig. 5.10 shows that $\hat{S}_{fcc-fcc}$ increases more

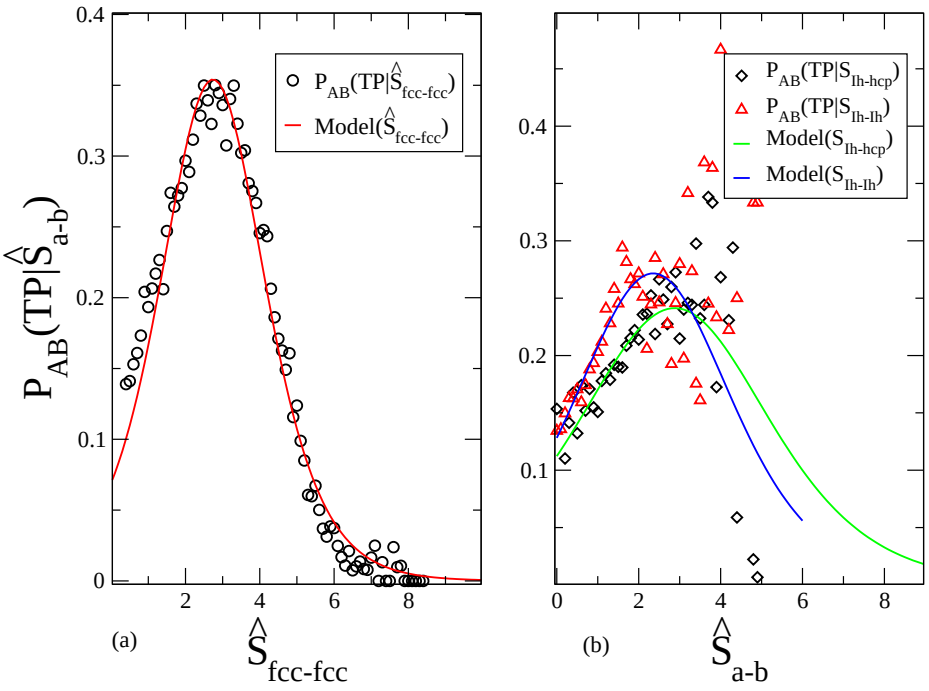

Figure 5.9: The transition path probabilities for *liquid* $\rightarrow$ *Ih* transition as a function of (a) $\hat{S}_{fcc-fcc}$, (b) $\hat{S}_{Ih}$ and S_{Ih-hcp}, with their respective models

rapidly than the $\hat{S}_{Ih-hcp}$. During the formation of Ih cluster, the tetrahedra cannot be packed in a way that completely fills space and the system must be strained in order to form a uniform structure. This strain seems to slow down the formation of the five-fold facets which gives Ih its character.

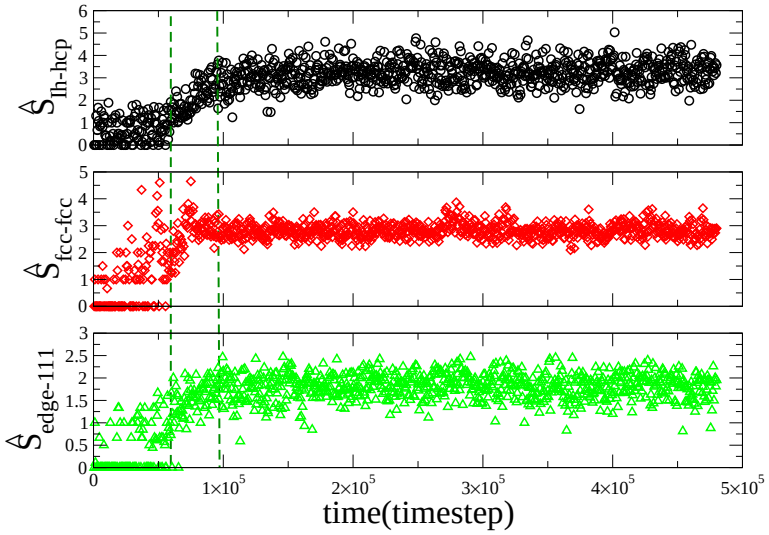

Figure 5.10: A Plot showing $\hat{S}_{Ih-hcp}$, $\hat{S}_{fcc-fcc}$ and $\hat{S}_{edge-<111>}$ for Ih trajectory.

The best single order parameter is compared to the best reaction coordinate from all pairs of order parameters, which is in turn compared to the best coordinate from all combinations of three order parameters, etc. The likelihood will always increase each time a parameter is added to the model, but a new parameter is significant to the reaction coordinate if the increase in likelihood is equal or greater than $(1/2)\ln N_R$, where N_R is the number of realizations in the likelihood function. The results for the combinations of the order parameters are summarized in Table 5.6. From the likelihood estimate, it shows that a linear combination of n, $\hat{S}_{fcc-fcc}$, and the Q_e, is the best reaction coordinate describing the formation of icosahedral structure. The full reaction coordinate is given as

$$r = 0.00880n + 0.2261\hat{S}_{fcc-fcc} + 3.1582Q_e - 2.9533, \tag{5.14}$$

with a critical condition being

$$\hat{S}^*_{fcc-fcc} = 13.0617 - 0.03893n - 13.9735Q_e. \tag{5.15}$$

It should be noted that the transition path probabilities is not guarantied to be equal to 0.5 at the critical point, but, always a maximum. To solve for the critical conditions, $\partial P_{liq-Ih}(r)/\partial r = 0$ is evaluated, where P_{liq-Ih} is the transition path probability as a function of the reaction coordinate, r. Fig. 5.11 is a 3-dimensional plot of the shooting points using $n, \hat{S}_{fcc-fcc}$ and Q_e. The red points are points for a typical trajectory leading to Ih structure. Points on the plane $S^*_{fcc-fcc} = 13.0617 - 0.03893n - 13.9735Q_e$ indicate the critical point, which is a saddle point. Fig. 5.12 shows the density plot of the shooting points that lie on the $liquid \rightarrow Ih$ transition path using the order parameters, n and $\hat{S}_{fcc-fcc}$. Also shown are two lines representing the critical conditions when $Q_e = 0.18$ and $Q_e = 0.31$. The green and blue dots are points from two different trajectories leading to Ih structure. They pass through the region of highest density between the lines representing the critical conditions. From both plots it can be seen that at a fixed embryo size, increasing $\hat{S}_{fcc-fcc}$ increases the probability of the formation of Ih structures. But as seen in fig. 5.12, as $\hat{S}_{fcc-fcc}$ increase well beyond 3, the probability starts to decline. All shooting points lying on the plane $\hat{S}^*_{fcc-fcc} = 13.0617 - 0.03893n - 13.9735Q_e$ belong to the transition state ensemble. It includes small embryos with some well formed tetrahedra (values of $\hat{S}_{fcc-fcc} \sim 3.0$) and large embryos with small values of $\hat{S}_{fcc-fcc}$.

Order Parameters	Reaction Coordinates (r)	$LE_{\alpha max}$	r^*
$\hat{S}_{fcc-fcc}, Q_e$	$0.1976\hat{S}_{fcc-fcc} + 5.3449Q_e - 1.4428$	-44529.6	$\hat{S}^*_{fcc-fcc} = 7.298 - 27.0366Q_e$
$\hat{S}_{fcc-fcc}, \hat{S}_{Ih-hcp}$	$0.5403\hat{S}_{fcc-fcc} + 0.09242\hat{S}_{Ih-hcp} - 1.5917$	-44148.3	$\hat{S}^*_{fcc-fcc} = 2.9454 - 0.1710\hat{S}_{Ih-hcp}$
$\hat{S}_{fcc-fcc}, \hat{S}_{vert-edge}$	$0.5218\hat{S}_{fcc-fcc} - 0.1311\hat{S}_{vert-edge} - 1.326$	-44111.2	$\hat{S}^*_{fcc-fcc} = 2.5411 + 0.2513\hat{S}_{vert-edge}$
$\hat{S}_{fcc-fcc}, \hat{S}_{edge-<111>}$	$0.5309\hat{S}_{fcc-fcc} + 0.0229\hat{S}_{edge-<111>} - 1.4894$	-44187.7	$\hat{S}^*_{fcc-fcc} = 2.8048 - 0.04330\hat{S}_{edge-<111>}$
$\hat{S}_{fcc-fcc}, \hat{S}_{Ih-Ih}$	$0.5270\hat{S}_{fcc-fcc} - 0.0732\hat{S}_{Ih-Ih} - 1.3131$	-44164.7	$\hat{S}^*_{fcc-fcc} = 2.4914 + 0.1389\hat{S}_{Ih-Ih}$
$\hat{S}_{fcc-fcc}, n$	$0.3345\hat{S}_{fcc-fcc} + 0.006762n - 2.07468$	-42901.0	$\hat{S}^*_{fcc-fcc} = 6.198 - 0.02020n$
$\hat{S}_{fcc-fcc}, n, \hat{S}_{vert-edge}$	$0.00713n + 0.3115\hat{S}_{fcc-fcc} - 0.18940\hat{S}_{vert-edge} - 1.9329$	-42722.8	$\hat{S}^*_{fcc-fcc} = 6.0596 - 0.02187n + 0.2865\hat{S}_{vert-edge}$
$\hat{S}_{fcc-fcc}, n, \hat{S}_{edge-<111>}$	$0.00717n + 0.3277\hat{S}_{fcc-fcc} - 0.09386\hat{S}_{edge-<111>} - 1.986$	-42852.7	$\hat{S}^*_{fcc-fcc} = 6.2049 - 0.02289n + 0.6080\hat{S}_{edge-<111>}$
$\hat{S}_{fcc-fcc}, n, Q_e$	$0.00880n + 0.2261\hat{S}_{fcc-fcc} + 3.1582Q_e - 2.9533$	-42467.0	$\hat{S}^*_{fcc-fcc} = 13.0617 - 0.03893n - 13.9735Q_e$

Table 5.6: Different single order parameters tested for $liquid \rightarrow Ih$ transitions in gold nanocluster. $BIC = (1/2)lnN_R = 4.942$.

To understand the nature of the critical embryo, configurations from the trajectories heading to Ih lying within the transition state ensemble are chosen for visualization. A conjugate gradient quench is performed on these configurations which takes the configurations to their

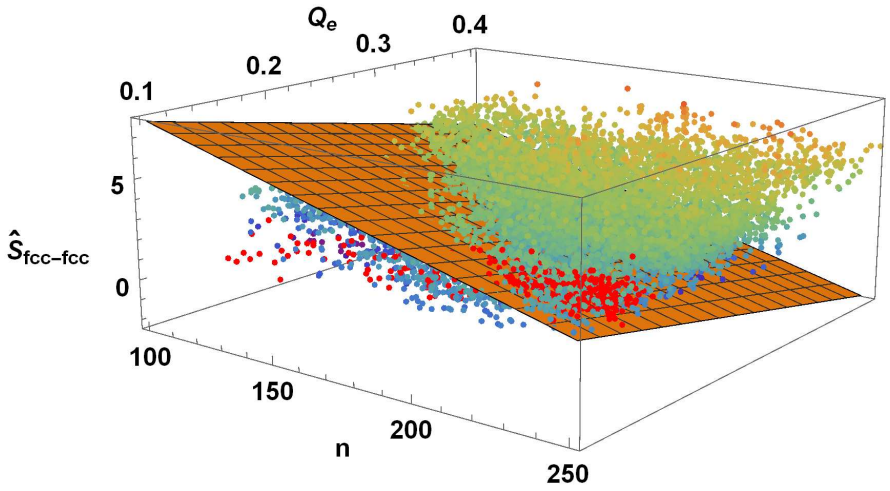

Figure 5.11: Shooting points that lie on the *liquid* $\rightarrow$ *Ih* transition path plotted with $n, \hat{S}_{fcc-fcc}$ and Q_e. The red points are points for a typical trajectory leading to *Ih* structure.

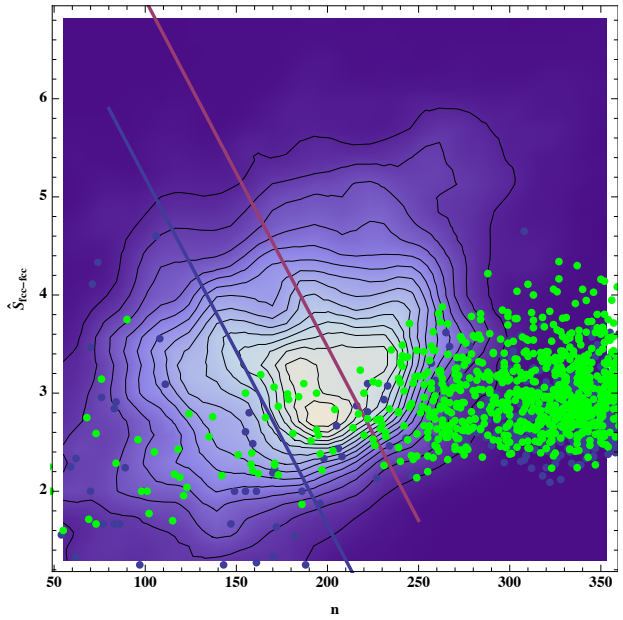

Figure 5.12: Shooting points that lie on the *liquid* $\rightarrow$ *Ih* transition path projected into order parameters, n and $\hat{S}_{fcc-fcc}$. The purple and pink lines are critical lines for $Q_e = 0.18$ and $Q_e = 0.31$

local potential energy minima, or inherent structures [137], to remove the thermal noise from the structure. A 2D visualization of the maximum embryo is produced by projecting the CNA order parameters for each atom in the embryo onto a unit sphere that surrounds the cluster and is centered on the center of mass of the embryo [148]. This projection is then flattened into a two dimensional plot of the inclination, θ, and azimuth, ϕ, angles of the atoms that are periodic at the boundaries. Fig. 5.13 shows the projections for bulk and surface atoms, respectively, from a configuration taken from the transition state ensemble. It shows that one side of the cluster is mostly ordered while a section is still amorphous. Within the ordered region, the bulk fcc atoms are mostly aligned to form tetrahedra (black circles within dashed green boxes), which is bounded on the surface by the $< 111 >$ (black triangles within magenta boxes) planes. The formation of five-fold symmetric cap (red squares in dashed blue circles) occurs in the same region. This shows that at the critical point, the facets leading to an icosahedral structures are already in place. The results from MPMLA and the analysis of the trajectory point to the fact that the icosahedral structure forms through the gradual joining together of the tetrahedra rather than a shell-by-shell growth process[31].

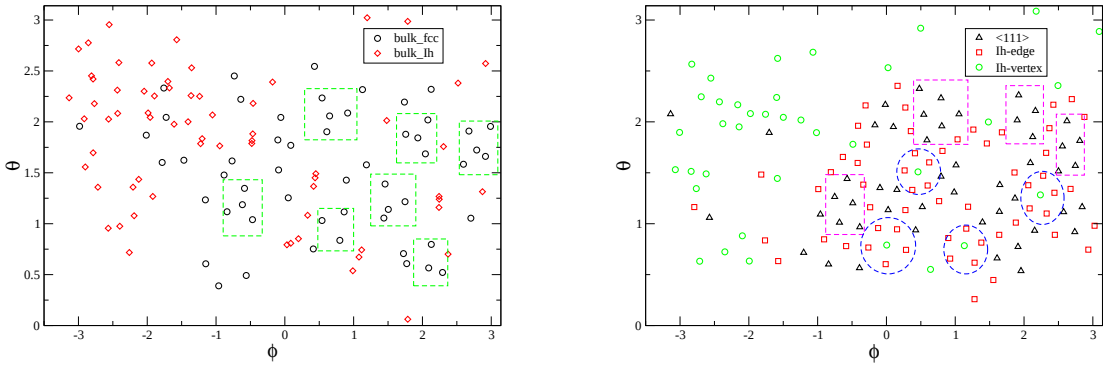

(a) Bulk order

(b) Surface order

Figure 5.13: A 2D visualization of a configuration on the transition state leading to the icosahedral structure.(a)The black circles enclosed within the green boxes are the bulk Fcc atoms arranged to form tetrahedra structures. (b) The black triangles enclosed within magenta boxes are the surface $< 111 >$ facets while the red squares within the blue circles are the atoms forming the five fold cap.

Fig. 5.14 shows the distribution of p_{Ih} estimates for the best reaction coordinate obtained from the MPMLA. 300 initial configurations are selected from the TSE, between the two

lines in fig. 5.12. For each configuration, 100 trajectories are run, and the trajectories are terminated when the product basins is reached. p_{Ih} is the fraction of trajectories that ended in the Ih structure. Fig. 5.14 shows that the distribution peaks at $p_{Ih} = 0.5$, implying that at the transition state described by the reaction coordinate, the configurations have a 50% chance of going to the Ih structure. This confirms that the linear combination of $n, \hat{S}_{fcc-fcc}$ and Q_e describes the $liquid \rightarrow Ih$ transition.

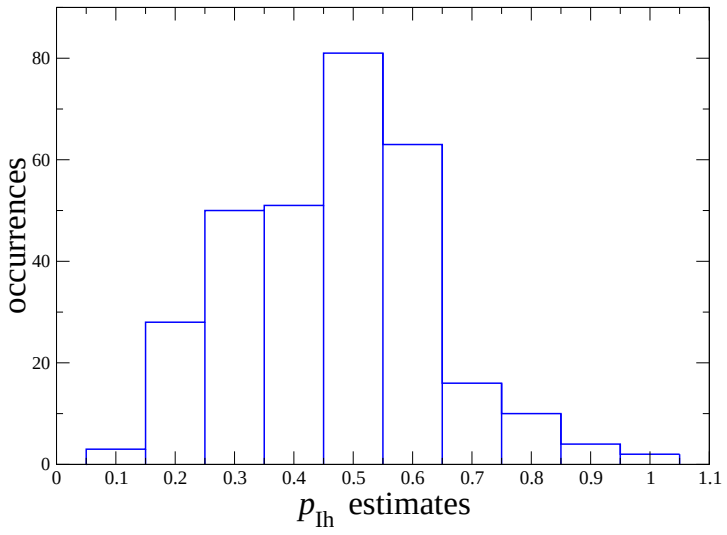

Figure 5.14: A p_{Ih} distribution histogram for the critical condition, $\hat{S}^*_{fcc-fcc} = 13.0617 - 0.03893n - 13.9735Q_e$.

5.3.2 Decahedral Structure

Table 5.7 contains a summary of the results for the maximum likelihood analysis for the TPE along the $liquid \rightarrow Dh$ transition path using single order parameters. Based on the likelihood score, embryo size, n, is better than the rest of the parameters. But, n does not say anything about the hierarchical order that appears in the structures found during the freezing of gold nanoclusters. In terms of the structural order parameters, $\hat{S}_{fcc-fcc}$ has the highest likelihood, second only to n. A Dh has a single line of bulk Ih atoms in the core, surrounded by five planes of bulk Hcp atoms. Fig. 5.15 shows a plot of $\hat{S}_{Ih-hcp}$, $\hat{S}_{fcc-fcc}$ and $\hat{S}_{edge-<111>}$ for a trajectory ending in the Dh structure. It shows that although $\hat{S}_{Ih-hcp}$ gives

Dh its unique characteristics, it is built at a later time than the grouping together of bulk fcc atoms and the formation of the surface facets.

Order Parameters	Reaction Coordinates (r)	$LE_{\alpha max}$	r^*
n_{CNA}	$0.01155 * n_{CNA} - 0.9847$	-10187.9	$n^*_{CNA} = 85.2$
n	$0.00883n - 1.4538$	-10132.9	$n^* = 164.6$
Q_e	$8.0096Q_e - 2.2393$	-10264.9	$Q^*_e = 0.2795$
$\hat{S}_{Ih-hcp}$	$0.6756\hat{S}_{Ih-hcp} - 0.6938$	-10312.8	$\hat{S}^*_{Ih-hcp} = 1.027$
$\hat{S}_{fcc-fcc}$	$0.3702\hat{S}_{fcc-fcc} - 1.2374$	-10224.3	$\hat{S}^*_{fcc-fcc} = 3.342$
$\hat{S}_{vert-edge}$	$0.1603\hat{S}_{vert-edge} - 0.02783$	-10352.9	$\hat{S}^*_{vert-edge} = 0.1736$
$\hat{S}_{edge-<111>}$	$0.4018\hat{S}_{edge-<111>} - 0.3023$	-10328.4	$\hat{S}^*_{edge-<111>} = 0.7522$
$\hat{S}_{Ih-Ih}$	$0.37906\hat{S}_{Ih-Ih} - 0.7285$	-10342.7	$\hat{S}^*_{Ih-Ih} = 1.9220$

Table 5.7: Different single order parameters tested for $liquid \rightarrow Dh$ transitions in gold nanoclusters. $BIC = (1/2)\ln N_R = 3.837$.

The results for the combinations of the order parameters is summarized in Table 5.8. It shows that the best reaction coordinate describing the formation of the decahedral structure is the linear combination of n, Q_e, and $\hat{S}_{edge-<111>}$, and it is given as,

$$r = 0.00904n + 5.4419Q_e - 0.2714\hat{S}_{edge-<111>} - 3.1467. \tag{5.16}$$

The equation defining the critical surface is

$$Q^*_e = 0.578236 - 0.00166118n + 0.0498723\hat{S}_{edge-<111>}. \tag{5.17}$$

Q_e in the reaction coordinate is sensitive to hexagonal symmetries and captures the overall quality of the embryo, while $\hat{S}_{edge-<111>}$ captures the formation of the five-fold cap. Fig. 5.16 shows the shooting point that lies on the liquid→ Dh transition path and the surface defining the critical conditions for this transition. Also shown is a typical trajectory leading to a Dh structure. The same data is presented in fig. 5.17 but with only n and Q_e. Also shown in fig. 5.17 is the critical condition given by eq. 5.17, for $\hat{S}_{edge-<111>} = 1$ and $\hat{S}_{edge-<111>} = 4$. It can be seen that for a fixed n, increasing Q_e and $\hat{S}_{edge-<111>}$ increases the chances of Dh nucleating from the system.

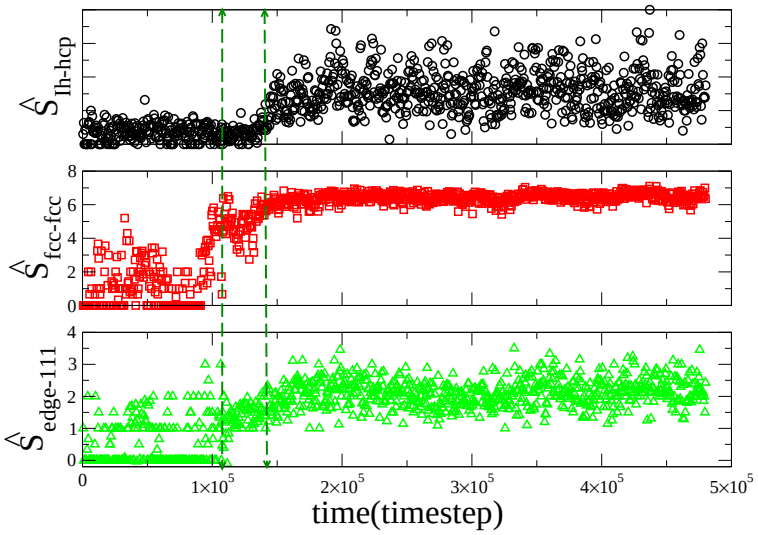

Figure 5.15: A Plot showing $\hat{S}_{Ih-hcp}$, $\hat{S}_{fcc-fcc}$ and $\hat{S}_{edge-<111>}$ for Dh trajectory.

Order Parameters	Reaction Coordinates (r)	$LE_{\alpha max}$	r^*
n, Q_e	$0.00839n + 6.9244Q_e - 3.5919$	-10096.4	$Q_e^* = 0.5187 - 0.00121n$
$n, \hat{S}_{Ih-hcp}$	$0.00883n + 0.5152\hat{S}_{Ih-hcp} - 1.9106$	-10130.9	$S^*_{Ih-hcp} = 3.7084 - 0.017139n$
$n, \hat{S}_{fcc-fcc}$	$0.00708n + 0.1298\hat{S}_{fcc-fcc} - 1.6340$	-10113.4	$\hat{S}^*_{fcc-fcc} = 12.5814 - 0.05456n$
$n, \hat{S}_{vert-edge}$	$0.00893n - 0.29272\hat{S}_{vert-edge} - 1.3691$	-10123.3	$\hat{S}^*_{vert-edge} = 0.03050n - 4.6770$
$n, \hat{S}_{edge-<111>}$	$0.00872n + 0.0250\hat{S}_{edge-<111>} - 1.4624$	-10132.7	$\hat{S}^*_{edge-<111>} e = 58.3345 - 0.34816n$
$n, Q_e, \hat{S}_{Ih-hcp}$	$0.00872n - 0.28732\hat{S}_{Ih-hcp} + 6.3657Q_e - 3.2319$	-10077	$\hat{S}^*_{Ih-hcp} = 0.03036n + 22.1549Q_e - 11.248$
$n, Q_e, \hat{S}_{fcc-fcc}$	$0.00753n + 0.1136\hat{S}_{fcc-fcc} +$ $4.6722Q_e - 3.19494$	-10084.7	$\hat{S}^*_{fcc-fcc} =$ $\hat{S} = 28.119 - 0.06633n - 41.121Q_e$
$n, Q_e, \hat{S}_{vert-edge}$	$0.00891n + 7.3105Q_e -$ $0.1811\hat{S}_{vert-edge} - 3.57832$	-10079.8	$\hat{S}^*_{vert-edge} =$ $0.04922n - 40.3603Q_e - 19.7552$
$n, Q_e, \hat{S}_{edge-<111>}$	$0.00904n + 5.4419Q_e -$ $0.2714\hat{S}_{edge-<111>} - 3.1467$	-10073.1	$\hat{S}^*_{edge-<111>} =$ $0.0333n + 20.0494Q_e - 11.593$

Table 5.8: Linear combination of order parameters tested for liquid→Dh transitions in gold nanoclusters. $BIC = (1/2)\ln N_R = 3.837$.

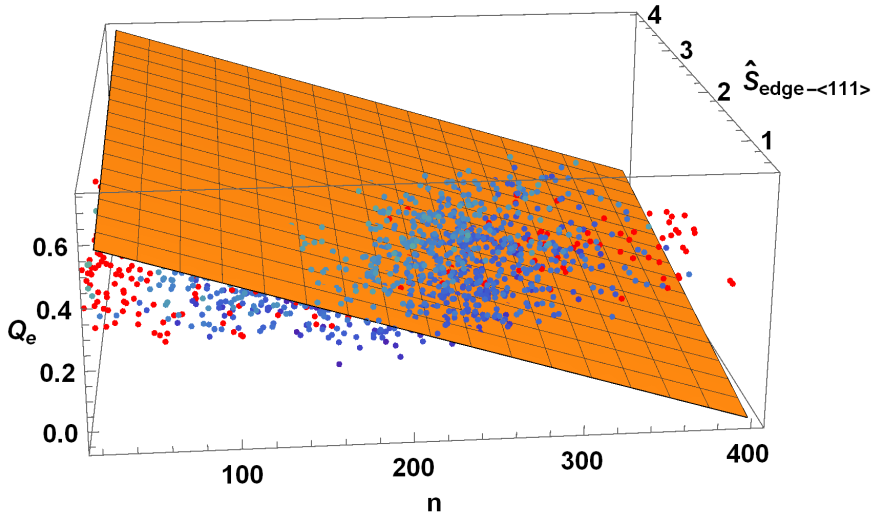

Figure 5.16: Shooting points that on the $liquid \rightarrow Dh$ transition path plotted with order parameters making the reaction coordinate (n, Q_e and $\hat{S}_{edge-<111>}$). The red points are on a typical trajectory leading to Dh structure.

Configuration along the trajectories in fig. 5.16 that lie on the critical surface are chosen and visualized in detail to understand the nature of the critical embryo. Fig. 5.18 shows the projections for bulk and surface atoms, respectively, from the embryo of a configuration at the transition state leading to a Dh structure. It shows that within one side of the embryo, the bulk fcc atoms are mostly aligned to form large tetrahedra (black circles within dashed green boxes) which are bounded on the surface by the $< 111 >$ (black triangles within magenta boxes) planes. The number of bulk fcc atoms here is greater than that observed in the case of the Ih. But the number of $< 111 >$ planes is less than observed for Ih. In fig. 5.18 there are two five-fold symmetric caps (red squares in dashed blue circles) appearing, but they are not linked together. One of these caps later dissolves and appears at the opposite end of the other cap to give the structure its unique characteristic. This shows that at the critical point, the bulk Fcc atoms are grouped to form a block and at least one five-fold symmetric cap appears, which is similar to Ih, but the formation of the line of bulk Ih surrounded by Hcp atoms gives it the final structure. This latter formation of the line of bulk Ih surrounded by Hcp atoms as seen in fig. 5.15 may be one of the factors causing a higher free energy barrier to the Dh structure, in addition to the appearance of high energy $< 100 >$ facets.

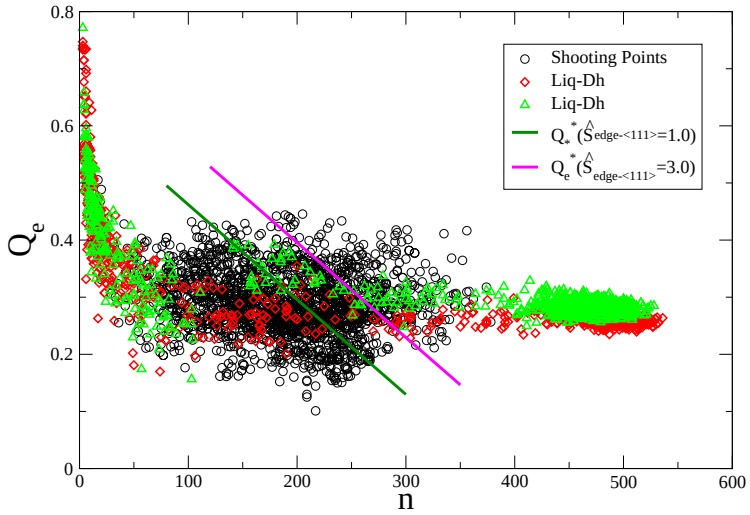

Figure 5.17: Shooting points that are on the $liq \rightarrow Dh$ transition path projected into order parameters, n and Q_e.

5.3.3 FCC Structure

For the formation of the FCC structure, the Q_e has the highest likelihood score among the single order parameters (see Table 5.9). Q_e is the Q_6 calculated using the atoms in the largest embryo, and it is sensitive to the hexagonal nature of a single fcc or Hcp atom. This correlation may be the reason why Q_e is better than $\hat{S}_{fcc-fcc}$ as most FCC structures contain fcc and Hcp atoms. Another order parameter that performs well is $\hat{S}_{Ih-hcp}$. A metastable liquid contains a large number of bulk Ih atoms, while a perfect FCC structure has no bulk Ih atoms. The elimination of these bulk Ih appears to be important for the evolution of FCC structure. Fig. 5.19 shows the transition path probabilities along the liquid$\rightarrow$ FCC transition path as a function of $\hat{S}_{Ih-hcp}$ and $\hat{S}_{fcc-fcc}$, and the models which describe them. It shows that the model $P(TP|\hat{S}_{Ih-hcp})$ fits better to the data. The scatter in the $P(TP|\hat{S}_{fcc-fcc})$ maybe due to the presence of Hcp atoms in the FCC clusters. A configuration that lies on the liquid$\rightarrow$ FCC transition path can contain a high ratio of bulk Hcp atoms compared to bulk fcc atoms. Table 5.9 contains a summary of the maximum likelihood analysis. It shows that a linear combination of Q_e, $\hat{S}_{Ih-hcp}$ and $\hat{S}_{edge-<111>}$ is the

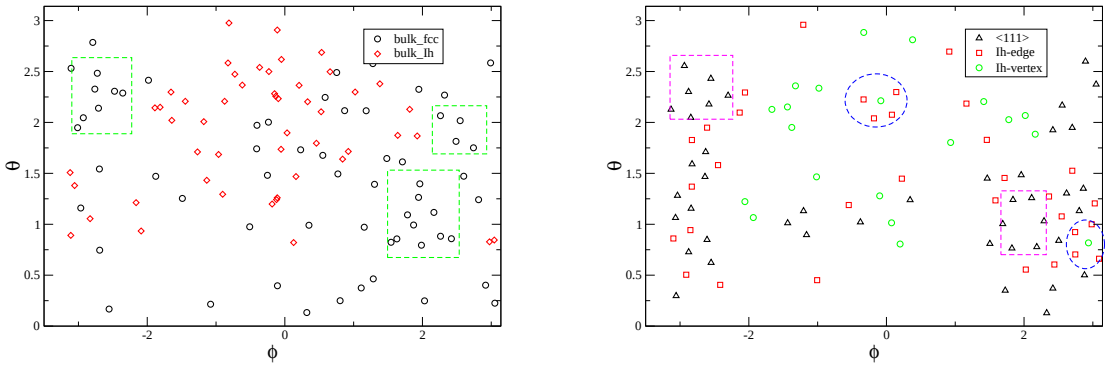

(a) Bulk order

(b) Surface order

Figure 5.18: A 2D visualization of the critical embryo leading to the *Dh* structure. Black circles with green boxes are the bulk fcc atoms, black triangles within magenta boxes are the surface $< 111 >$, while red squares in blue dashed circle indicate the five-fold cap.

best reaction coordinate. The growth of bulk fcc atoms and the elimination of five-fold local structures ($\hat{S}_{Ih-hcp}$ and $\hat{S}_{edge-<111>}$) are the major drivers to the nucleation of an FCC phase.

Order Parameters	Reaction Coordinates (r)	$LE_{\alpha max}$	r^*
n	$0.00796n - 1.4814$	-10566.7	$n^* = 185.9$
Q_e	$9.1935Q_e - 3.3292$	-10264.9	$Q_e^* = 0.3621$
$\hat{S}_{Ih-hcp}$	$0.9362\hat{S}_{Ih-hcp} - 0.4621$	-10524	$\hat{S}^*_{Ih-hcp} = 0.49353$
$\hat{S}_{fcc-fcc}$	$0.2708\hat{S}_{fcc-fcc} - 1.4750$	-10612.8	$\hat{S}^*_{fcc-fcc} = 5.4455$
n, Q_e	$0.005814 + 9.794Q_e - 4.53058$	-10388.7	$Q_e^* = 0.4626 - 0.0005936n$
$Q_e, \hat{S}_{Ih-hcp}$	$7.7331Q_e - 0.4512\hat{S}_{Ih-hcp} - 2.5252$	-10359.9	$\hat{S}^*_{Ih-hcp} = 17.138Q_e - 5.5964$
$Q_e, \hat{S}_{fcc-fcc}$	$9.7686Q_e - 0.09838\hat{S}_{fcc-fcc} - 3.13996$	-10407.9	$\hat{S}^*_{fcc-fcc} = 99.2899Q_e - 31.9151$
$Q_e, \hat{S}_{Ih-hcp}, \hat{S}_{edge-<111>}$	$7.0602Q_e - 0.2529\hat{S}_{Ih-hcp}$ $-0.41233\hat{S}_{edge-<111>} - 2.0240$	-10292.0	$Q_e^* = 0.2866 + 0.0358\hat{S}_{Ih-hcp}$ $+0.0584013\hat{S}_{edge-<111>}$

Table 5.9: Different single order parameters tested for $liq \rightarrow FCC$ transitions in gold nanoclusters. $BIC = (1/2)\ln N_R = 3.858$.

The p_{FCC} estimate distribution is calculated to determine the accuracy of $r = 7.0602Q_e - 0.2529\hat{S}_{Ih-hcp} - 0.41233\hat{S}_{edge-<111>} - 2.0240$ as reaction coordinate for the liquid→ FCC transition. 96 initial configurations are selected from the TSE and 100 trajectories are made from each configuration. p_{FCC} is the fraction of trajectories that ended in the FCC structure for each configuration. Fig. 5.20 shows that the distribution peaks at $p_{FCC} = 0.5$, implying

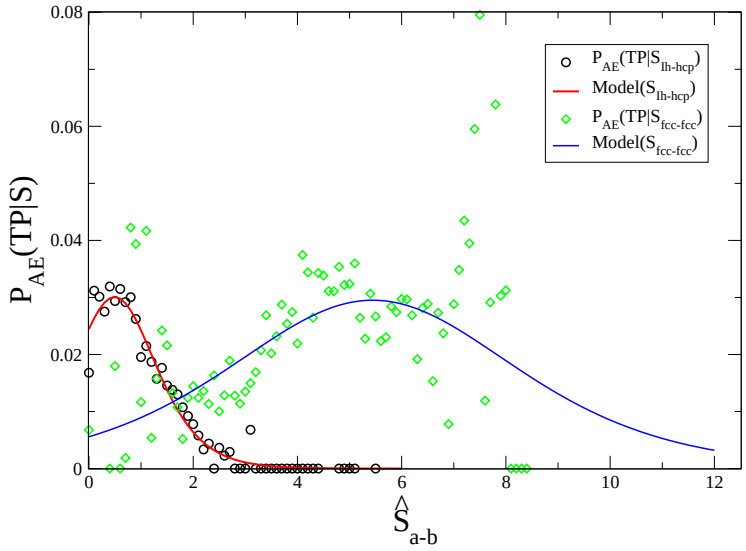

Figure 5.19: Plot of the transition path probabilities for Liq $\rightarrow FCC$ transition as a function of $\hat{S}_{fcc}$ and $\hat{S}_{Ih-hcp}$.

that within the transition state described by the reaction coordinate, the configurations have a 50% chance of growing into the FCC structure. This confirms that the anti-correlation of all the five-fold local environment and the Q_e best describe the $liquid \rightarrow FCC$ transition.

5.3.4 Icosahedral - Decahedral Transition

In fig. 5.7(b), we see the transition path probabilities for the various solid→solid transformations. Of particular interest is the $Ih \rightarrow Dh$ transition which has been observed experimentally[31]. From the MLA performed on the collective variable on this transition path, the best reaction coordinate for this transition is the linear combination of n and Q_e. This is the same pair of order parameters that describe the formation of the Dh structure, which may cause confusion. Fig. 5.21 shows points along liquid→ Ih path projected into n and Q_e, and two trajectories passing through Ih to Dh. It also shows a single trajectory that nucleates directly to Dh. The first critical line (green) is the transition point to Ih using the TPE for the $liquid \rightarrow Ih$. Visualization of the configurations lying on this TSE shows the features of a critical embryo on its way to the Ih structure (see fig. 5.22(a)). Fig. 5.22(a) shows the bulk fcc atoms positioned to form the tetrahedra that join to form the Ih structure. At the second transition state (maroon), there has been some rearrangement of the bulk Fcc atoms to form larger blocks as shown in fig. 5.22(b) .

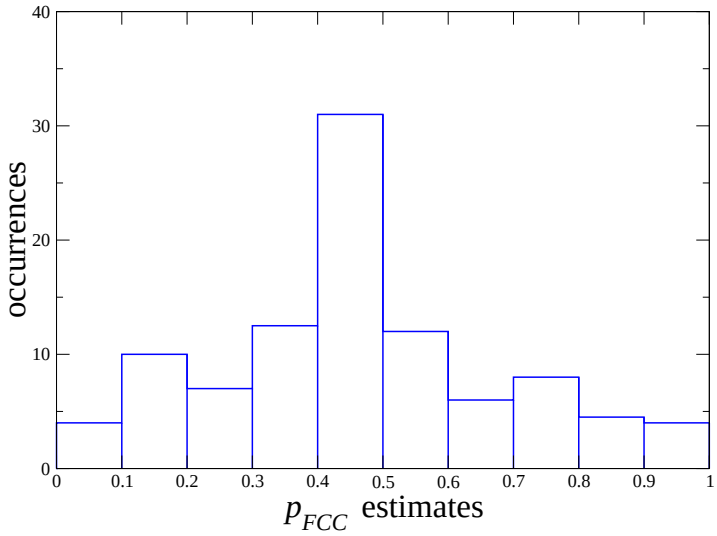

Figure 5.20: A p_{FCC} distribution histogram for the critical condition, $Q_e^* = 0.2866 + 0.0358\hat{S}_{Ih-hcp} + 0.0584013\hat{S}_{edge-<111>}$.

5.3.5 Discussion

The probabilities for a configuration to lie on the liquid→Ih transition path is an order of magnitude higher than others. This is in agreement with results from direct calculations of the probability of observing Ih structure in an ensemble of nucleation events[3]. This shows that our scheme is able to identify the stable basin and that the multiple states shooting is properly executed. The results from the MPMLA show that while embryo size and Q_e can accurately describe transitions from liquid to solid states, the structural parameters are very important in understanding the formation of the different structures found during freezing of gold nanoclusters. Although these structural parameters are present in all the structures, their responses are unique to each of the transition paths. The $\hat{S}_{fcc-fcc}$ parameter indicates the coming together of bulk fcc atoms. For the Ih structure, this parameter measures the formation of tetrahedral units, and it is a very good component of the reaction coordinate for the formation of Ih cluster from the metastable liquid. A further look at the trajectories producing Ih shows that the Ih structure grows by the sequential addition of tetrahedral subunits. A few tetrahedral subunits can pack together without introducing significant strain

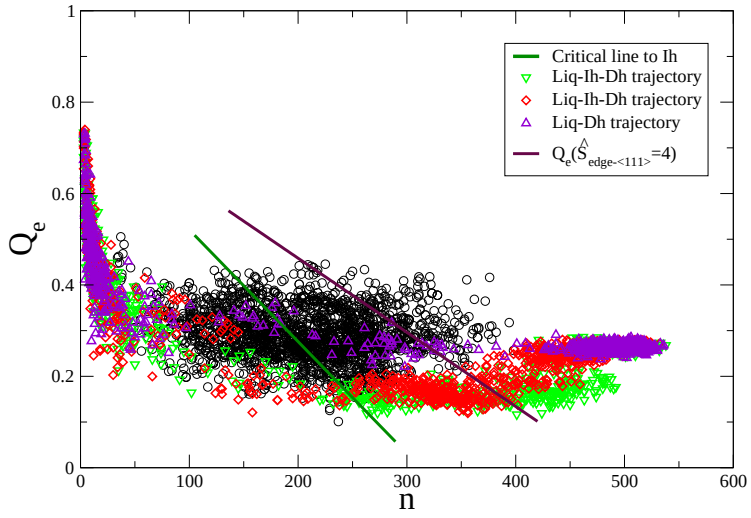

Figure 5.21: Shooting points that on the $Ih \rightarrow Dh$ transition path projected into order parameters, n and Q_e, showing trajectories ending in Ih and Dh

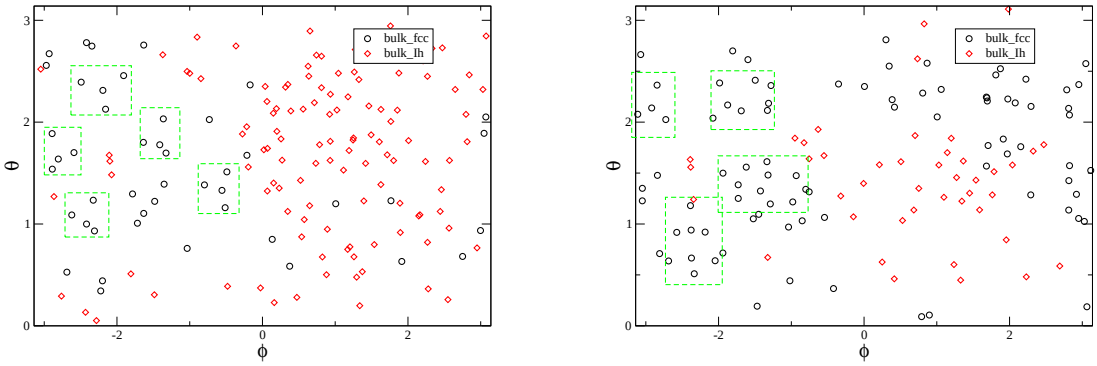

(a) $Liq \rightarrow Ih$ (b) $Ih \rightarrow Dh$

Figure 5.22: A 2D visualization of the critical embryo leading to the decahedral structure from the icosahedral structure. Black circles within green boxes show the position of the bulk fcc atom.

into the system, allowing the Ih to grow. However, since they cannot fill space, the last few subunits cannot be completed without redistributing the stress throughout the structure, giving rise to the partially formed Ih structures found in the simulations. The Dh structures are formed through the initial formation of surface $< 111 >$ facets, with a corresponding growth of blocks of bulk *fcc* atoms. Although the formation of Ih and Dh structures share the formation of a five-fold symmetric cap, the clustering of the bulk *fcc* atoms underneath the cap is made in a different manner. While regular tetrahedral units are formed in Ih, a large block in the form of a triangular prism is the shape of the bulk *fcc* atoms in the case of Dh structure. This highlights how the delicate balance between surface and bulk growth play an important role in the competitive nucleation in nanoclusters.

Despite the large grouping of bulk fcc atoms in Dh and FCC structures, $\hat{S}_{fcc-fcc}$ is not part of the reaction coordinates for the formation of these structures from the liquid. Q_e is sensitive to to hexagonal environments present due to bulk fcc, bulk Hcp, $< 111 >$ and $< 100 >$ atoms. Hence, Q_e becomes a stronger order parameter for Dh and FCC structures since they contain high ratios of the hexagonal environment. Table 5.10 contains the coefficients of the major test order parameters when used as reaction coordinate for the different structures. As these coefficients increase, the order parameter becomes more important for a given transition. Hence, while Q_e is the least important for the $liquid \rightarrow Ih$ transition, it is most important for the $liquid \rightarrow FCC$ transition. The order parameters measuring the growth of five-fold symmetry environments ($\hat{S}_{Ih-hcp}$ and $\hat{S}_{edge-<111>}$) are significant in the formation of FCC. This is a form of anti-correlation, as elimination of five-fold symmetry enhances the growth of the FCC structure.

Structure	n	$\hat{S}_{fcc-fcc}$	$\hat{S}_{Ih-hcp}$	Q_e	$\hat{S}_{edge-<111>}$
Ih	0.0111	0.532	0.3915	6.170	0.2674
Dh	0.0088	0.370	0.6756	8.009	0.4018
FCC	0.0079	0.270	0.9362	9.193	0.6774

Table 5.10: Coefficients of the different order parameters for the different structures formed from the metastable liquid.

5.4 Conclusions

The evolution of the solid phase is best described by size and the orientational order parameter of the embryo, but to follow the formation of each of the structures, a structural order parameter is required. The formation of Ih is through the tetrahedral structures having one of its sides as a $< 111 >$ plane. This shows that both surface and bulk grow at the same time, as Ih forms via a gradual coming together of the tetrahedral units and not shell by shell growth. Both Ih and Dh begin with a gathering of the bulk fcc atoms to form a tetrahedron in the Ih structure while oblong triangular pyramids form in the Dh. The alignment of the bulk Ih atoms surrounded by Hcp planes which gives it the characteristic five-fold symmetry, delays the formation of Dh structures. The maximum likelihood analysis shows that the Dh structure can nucleate directly from the metastable liquid as well as by solid-solid transition.

Chapter 6

Discussions and Conclusions

6.1 Discussions

The major theme in this thesis is to develop a molecular understanding of competition in phase transitions. Competitive nucleation is a phenomenon where a metastable phase can undergo nucleation to any of the many stable structures or phases. For example, molecular dynamic simulations and experiments have shown that nanoclusters at the same initial conditions nucleate to different structures, such as icosahedral, decahedral and face-centered cubic structures [1, 2, 3, 20, 31]. Competitive nucleation has been observed during the crystallization of proteins [77] and optically active sodium chlorate crystals [79]. Competitive nucleation often appears in systems that exhibit polymorphism. Therefore, understanding the dynamics of competitive nucleation is very essential in the production of materials whose desired properties, such as electrical [71], magnetic [73], optical and catalytic properties, are structure dependent.

In order to understand the dynamics of the nucleation process, a good knowledge of the reaction coordinate is required. The embryo size, which is often used as reaction coordinate in nucleation studies lacks information on the effects of surface areas, embryo geometry and structural order [11, 12], which are important in understanding how different structures are formed. Numerous studies [13, 14, 15] have been carried out with the aim of understanding how surface areas and structural order affect the different structures formed during competitive nucleation. However, these studies focused on identifying the nature of the global structures, rather than identifying the structure of the critical embryo. Therefore, this thesis sought to answer the question "**What are the most suitable reaction coordinates that can be followed to properly understand the formation of different structures during the nucleation of nanoclusters?**" To answer this question, the aimless shooting

algorithm was extended to sample multiple product basin, and a multiple path maximum likelihood analysis was developed and used to determine the appropriate reaction coordinate.

The research work covered in this thesis began by focusing on competitive heterogeneous nucleation in the Potts model because the system can be easily simulated, which allows the nucleation rates and free energy surfaces to be accurately calculated using a variety of different methods. The simplicity of the model also allows the nucleation conditions to be changed by adjusting a few parameters such as the external field and the interaction between the spins representing the different phases. This provides an opportunity to test the effectiveness of the rate calculations under different conditions. The Potts model also provides an ideal system for testing the new methodology associated with the multiple state aimless shooting and maximum likelihood analysis because the nucleation behaviour of the system can be fully characterized using the traditional methods.

The survival probability rate J_{SP} was selected as our reference rate because the method has been used extensively, is robust to the selection of cut off parameters [141], and is easily performed. However, it only provides information about the total rate at which materials leave the metastable basin, and provides no information regarding the nucleation of the competing phases. The transition state theory calculations do provide direct information about the nucleation of the different phases, but requires the calculation of the complete free energy surface and the calculation of the kinetic pre-factor. These can be time consuming and difficult calculations, particularly in cases where the system involves a more complicated molecular model.

The correct normalization of $\Delta G(n_B, n_C)$, with respect to the metastable region, was essential for correctly predicting the rates on the basis of eqs. 2.8 and 2.9 for the heterogeneous nucleation in the Potts model. This is consistent with earlier studies of heterogeneous nucleation in the Ising model [81]. Without the correct normalization of the free energy surface, the rates from the TST method overestimate the rates.These heterogeneous nucleation studies benefit from the fact that there is only a single nucleating embryo possible in the system, *i.e.*, the one located at the impurity, so that the cluster size is an accurate order parameter describing the state of the system. The question of the correct normalization remains a problem in homogeneous nucleation, where the normalization has only been shown in cases where the barriers are expected to be high and the nucleation embryo rare. The free

energy surfaces calculated in Chapter 2 are three dimensional in nature, involving two order parameters. Usually the saddle point approximation is used so that only the free energy of the lowest crossing point enters TST. Here, it was necessary to account for fact that the transition state becomes a boundary rather than a point, which involves introducing additional contributions. This also complicates the calculations of f^+ and the Zeldovich factor which serve as the pre-factors for eqs. 2.8 and 2.9. It was necessary to simplify the process. In future, it may be helpful to develop a more rigorous set of approximations for dealing with these features on two dimensional free energy surfaces.

The MFPT has been used to calculate nucleation rates in many systems, and to reconstruct the free energy surface for single component systems[110]. It is also useful in obtaining the critical size and the Zeldovich factor. But for the Potts model studied here, the critical size obtained from the fit to the MFPT does not define the transition state as it has no information regarding which phase it is going to. Also, the parameter c is not a representation of the curvature and therefore cannot be used to estimate the Zeldovich factor. These two kinetic parameters are important and given the type of model used here, the two dimensional Fokker-Planck equation should be appropriately related to a two dimensional MFPT, $\tau(n_B, n_C)$ where n_B^* and n_C^* can be obtained directly as fit parameters.

The sampling of any configuration with the aim of obtaining an accurate reaction coordinate for any transition must be achieved without reference to a pre defined reaction coordinate. To do this, the aimless shooting method of TPS was extended to sample configurations where multiple transitions may occur. The multiple path maximum likelihood expression was developed and used to maximize the probabilities of any configuration being on a certain transition path. While the two-state MLA can be tested using the committor probabilities or the transition path probabilities [11, 12], MPMLA used only the transition path probabilities. The results show that when there is absolutely no mixing between the two components, a linear combination of the size and surface area of the component was the most accurate reaction coordinate. The p_B distribution histogram confirms these results, which strongly suggest that for a competitive process, the method of decoupling the transition path is rigorous and accurate, provided the order parameter is unique to each phase. This shows the importance of local order parameters, unique to the competing phases, in understanding how each phase is formed through the process of competitive nucleation. The size of the

cluster is often regarded as a global parameter. While this is correct if the system is made of a single component, in the Potts model used in this work, the size of the different components could be regarded as a local order parameter. The surface area that is part of the reaction coordinate is the interfacial area between the evolving phase and the metastable phase and therefore a local order parameter. Unlike the homogeneous Ising model [11, 12], the shape of the cluster in this model does not vary much, but rather aligns with the shape of the heterogeneity. Therefore, for the critical clusters, both small and large sizes are compact unlike the fractal small critical sizes observed by Peters *et al*[12]. With partial mixing, the two components like sitting next to each other. Eliminating the opposite components increases the probability of the other phase being formed. This shows the negative effect of some order parameters, which means that certain local ordering must be removed or suppressed before a desired structure can nucleate from the metastable phase.

The second system studied in this thesis is competitive nucleation in gold nanoclusters. For this system, the probabilities of seeing a given structure in an ensemble of freezing events are temperature and size dependent. The results show that P_{Ih} increases with temperature while P_{Dh} and P_{Fcc} decrease with increase in temperature. The increase of P_{Ih} with respect to temperature is due to two factors; ((a) the low value of $\sigma_{<111>}$ which Ih surfaces are made of, compared to $\sigma_{<100>}$ that surrounds Dh and FCC structures, (b) the ratio of bulk Ih atoms in the metastable phase increases with temperature, making the metastable liquid more like the Ih phase. These reasons may explain why the Ih structure is the predominant structure, even in size range where energetic predictions favours the FCC structures. As size increases, P_{Ih} decreases at a fixed temperature. This means the smallest size ($N = 309$) form mostly Ih structures, while, the number of Ih formed decreases as the cluster becomes larger. On the other hand, P_{Dh} and P_{Fcc} increase with an increase in the cluster size, but their values are an order magnitude lower than P_{Ih}. The rates per particle decrease with increasing in temperature for all the cluster sizes.

In Chapter 5, the multiple path transition path sampling was used to sample gold nanoclusters. The multiple path maximum likelihood analyses was performed for the different transition paths. The probabilities of a configuration to lie on the $liquid \rightarrow Ih$ transition path is an order of magnitude higher than the others despite the fact that only 7% of the initial shooting points were from initial $liquid \rightarrow Ih$ trajectories. This confirms the initial

probabilities observed by the direct calculations in Chapter 4. The ability to reproduce the probabilities shows that the multi path aimless shooting scheme is able to identify the stable basin and the shooting is properly executed. The results for the multi-path maximum likelihood analyses in gold nanoclusters, show that while the embryo size as well as some global parameters such as Q_l's can accurately describe transitions from liquid to solid states, the structural parameters are very important in understanding the formation of the different structures found during freezing. Though these structural parameters are present in all the structures, their responses are unique to each of the transition paths. The $\hat{S}_{fcc-fcc}$ signal indicates the formation of tetrahedral units in the Ih, and is found to be a very good component of the reaction coordinate for the formation of the Ih structure. A further look at the trajectories producing Ih structure shows that the Ih structure grows by the sequential addition of tetrahedral subunits. A few tetrahedral subunits can be packed together without introducing significant strain into the system, allowing the Ih to grow. However, since they cannot fill space, the last few subunits cannot be completed without redistributing the stress throughout the structure, giving rise to the partially formed Ih structures found in the simulations. Presumably, the perfect Ih, in the case of the appropriate magic sized nanocluster, would be formed over a long period of time as the structure anneals. The Dh structures are nucleated through the initial formation of surface $< 111 >$ facets, with a corresponding growth of blocks of bulk *fcc* particles. Though the formation of the Ih and Dh structures share the formation of a five-fold symmetric cap, the clustering of the bulk *fcc* atoms underneath the cap is made in a different manner. While regular tetrahedral units are formed in the Ih, a triangular prism is the shape of the bulk *fcc* atoms in the case of the Dh structure. The formation of a five-fold symmetric cap and $< 111 >$ facets give credence to surface initiated freezing suggested by many authors[149, 150, 151], but the clustering of the bulk *fcc* atoms underneath shows that both surface and bulk growth start at the same time. Hence, this work highlights how the same delicate balance between surface and bulk that leads to the size dependent equilibrium phase diagram of nanoclusters also plays an important role in their competitive nucleation behavior.

Following the resulting reaction coordinate leads to the understanding of how local structures arrange themselves to form large scale non-crystalline structures such the Ih and Dh structures. Unfortunately, an explicit reason why the Ih structure is dominant even in size

ranges where the FCC is expected to have a global stability is not known. An in-depth look into the potential energy landscape may be necessary to understand the predominance of Ih structures. Although relative free energy barriers, $\beta\Delta G^*_{m,i}$ (see eq. 4.7), to the structures can be estimated from the probabilities of seeing the structures in simulation, a free energy calculation as a function of the obtained reaction coordinates is desirable. This could be used to further confirm the suitability of these reaction coordinates, though a three dimensional free energy calculation will be challenging. Another way of confirming the suitability of these reaction coordinates would be measuring the MFPT as a function of the different order parameters making up the reaction coordinate. This will measure the rates of crossing the barriers using the appropriate reaction coordinate in multiple dimension. In this work, the Bayesian information criterion and the committor probability estimates are the quantitative way of checking when additional parameter is significant to the reaction coordinate or otherwise. Also, the critical nuclei of each of the major transitions qualitatively indicate a high accuracy of our method. Despite the level of accuracy obtained in this work, an independent test of our methods could use the transition path ensemble to perform the Genetic Neural Network analysis.

6.2 Conclusions

In this thesis, a molecular understanding of competitive nucleation was investigated using the Potts model and gold nanoclusters. The free energy surface of the Potts model, with $q = 3$, nucleating on an impurity shows that the competition between the components reduces the level of wetting of the impurity. This competition also delays the nucleation thereby reducing the rates at which the system leaves the metastable phase when compared to single component system. The rate to each of the phases is a function of the free energy barrier which depends on the external field strength for each of the spins. The results show that the normalizing the free energy surfaces with respect to the phase space of the metastable state is important in calculating an accurate rate that compares to the rates obtained from other methods.

A multiple path maximum likelihood analysis was developed and used to explore the accurate reaction coordinates for the different transitions to stable phases. The linear combination of the size and surface area is the best reaction coordinate for each transition on the Potts model. The implication is that for competitive processes, the local order parameters explain

the transitions. For the transitions in gold nanoclusters, the correlations between the local geometric environment appear to explain the evolution of the different structures. The combination of these structural order parameters with the embryo size or the Q_e gives the best reaction coordinate for the different transitions. The formation of the five-fold symmetric cap at the same time when bulk tetrahedral structures are formed during the evolution of Ih and Dh geometries give credence to surface initiated nucleation as well as bulk nucleation.

References

[1] Y. G. Chushak and L. S. Bartell, "Melting and freezing of gold nanoclusters", *J. Phys. Chem. B* **105**, pp. 11605–11614 (2001).

[2] Ivan Saika-Voivod, Louis Poon, and Richard K. Bowles, "The role of fcc tetrahedral subunits in the phase behavior of medium sized lennard-jones clusters", *J. Chem. Phys.* **133**(7), pp. 074503 (2010).

[3] Cletus C. Asuquo and Richard K. Bowles, "Molecular dynamics simulations of competitive freezing in gold nanoclusters", *J. Phys. Chem. C* **116**, pp. 14619–14626 (2012).

[4] Niels Gregersen, Peter Bross, Søren Vang, and Jane H Christensen, "Protein misfolding and human disease", *Annu. Rev. Genomics Hum. Genet.* **7**, pp. 103–24 (2006).

[5] Kenneth R. Morris, Ulrich J. Griesser, Craig J. Eckhardt, and Joseph G Stowell, "Theoretical approaches to physical transformations of active pharmaceutical ingredients during manufacturing processes", *Adv. Drug Deliv. Rev.* , pp. 1–24 (2001).

[6] Mohamed Eddaoudi, Jaheon Kim, Nathaniel Rosi, David Vodak, Joseph Wachter, Michael O'Keeffe, and Omar M. Yaghi, "Systematic design of pore size and functionality in isoreticular mofs and their application in methane storage", *Science* **295**, pp. 469 (2002).

[7] David P. Sanders, Hernán Larralde, and François Leyvraz, "Competitive nucleation and the ostwald rule in a generalized potts model with multiple metastable phases", *Phys. Rev. B* **75**, pp. 132101 (2007).

[8] Pablo G. Debenedetti, *Metastable liquids: concepts and principles*, Princeton University Press, Princeton, New Jersey (1996).

[9] A. W. Castleman and R. G. Keesee, "Nucleation and growth of stratospheric aerosols", *Annu. Rev. Earth Planet Sci* **9**, pp. 227 (2008).

[10] Yurii G. Kuznetsov, Alexander J. Malkin, and Alexander McPherson, "The liquid protein phase in crystallization: a case studyintact immunoglobulins", *J. Cryst.Growth* **232**(1-4), pp. 30 – 39 (2001), Proceedings of the Eighth International Conference on Crystalliza tion of Biological Macromolecules.

[11] Albert C. Pan and David Chandler, "Dynamics of nucleation in the ising model", *J. Phys. Chem. B* **108**, pp. 19681–19686 (2004).

[12] Baron Peters and Bernhardt L. Trout, "Obtaining reaction coordinates by likelihood maximization", *J. Chem. Phys.* **125**(5), pp. 054108 (2006).

[13] W. Polak and A. Patrykiejew, "Local structures in medium-sized lennard-jones clusters:monte carlo simulations", *Phys. Rev. B* **67**(11), pp. 115402 (2003).

[14] Paul J. Steinhardt, David R. Nelson, and Marco Ronchetti, "Bond-orientational order in liquids and glasses", *Phys. Rev. B (Condensed Matter)* **28**, pp. 784 (1983).

[15] Yanting Wang, S. Teitel, and Christoph Dellago, "Surface-driven bulk reorganization of gold nanorods", *Nano Lett.* **5**(11), pp. 2174–2178 (2005).

[16] Gregg T. Beckham and Peters Baron, "Optimizing nucleus size metrics for liquid–solid nucleation from transition paths of near-nanosecond duration", *J. Phys. Chem. Lett.* **2**, pp. 1133–1138 (2011).

[17] Daniele Moroni, Pieter Rein Ten Wolde, and Peter G. Bolhuis, "Interplay between structure and size in a critical crystal nucleus", *Phys. Rev. Lett.* **94**, pp. 235703 (2005).

[18] Baron Peters, Gregg T. Beckham, and Bernhardt L. Trout, "Extensions to the likelihood maximization approach for finding reaction coordinates", *J. Chem. Phys.* **127**, pp. 4109 (2007).

[19] Ao Ma and Aaron R. Dinner, "Automatic method for identifying reaction coordinates in complex systems", *J. Phys. Chem. B* **109**(14), pp. 6769–79 (2005).

[20] Wolfgang Lechner, Jutta Rogal, Jarek Juraszek, Bernd Ensing, and Peter G. Bolhuis, "Nonlinear reaction coordinate analysis in the reweighted path ensemble", *J. Chem. Phys.* **133**, pp. 4110 (2010).

[21] Jutta Rogal and Peter G. Bolhuis, "Multiple state transition path sampling", *J. Chem. Phys.* **129**, pp. 4107 (2008).

[22] M. Kulmala, L. Pirjola, and J. Makela, "Stable sulphate clusters as a source of new atmospheric particles", *Nature* **404**(6773), pp. 66–9 (2000).

[23] Stephen R. Byrn, *Solid State Chemistry of Drugs*, Academic Press, New York (1982).

[24] Richard E. Lee, Gareth J. Warren, and Lawrence V. Gusta, *Biological Ice Nucleation and Its Applications*, APS Press (1995).

[25] Stephen Mann and Geoffrey A. Ozin, "Synthesis of inorganic materials with complex form", *Nature* **382**, pp. 313 (1996).

[26] C. Flageollet-Daniel, P. Ehrhard, and P. Mirabel, "Variation of the rate of nucleation with supersaturation in a thermal diffusion cloud chamber", *J. Chem. Phys.* **75**, pp. 4615 (1981).

[27] J. L. Schmitt, G. W. Adams, and R. A. Zalabsky, "Homogeneous nucleation of ethanol", *J. Chem. Phys.* **77**, pp. 2089 (1982).

[28] Atul Kacker and Richard H. Heist, "Homogeneous nucleation rate measurements. i. ethanol, n-propanol, and i-propanol", *J. Chem. Phys.* **82**, pp. 2734 (1985).

[29] M. P. Anisimov and A. G. Cherevko, "Gas-flow diffusion chamber for vapour nucleation studies. relations between nucleation rate, critical nucleus size and entropy of transition from a metastable into a stable state", *J. Aeros. Sc.* **16**(2), pp. 97–107 (1985).

[30] B. E. Wyslouzil, G. Wilemski, M. G. Beals, and M. B. Frish, "Effect of carrier gas pressure on condensation in a supersonic nozzle", *Phys. Fluids* **6**, pp. 2845 (1994).

[31] Kenji Koga, Tamio Ikeshoji, and Ko-Ichi Sugawara, "Size- and temperature-dependent structural transitions in gold nanoparticles", *Phys. Rev. Lett.* **92**, pp. 115507 (2004).

[32] Glenn M. Torrie and John P. Valleau, "Monte carlo free energy estimates using non-boltzmann sampling: Application to the sub-critical lennard-jones fluid", *Chem. Phys. Lett.* **28**, pp. 578–581 (1974).

[33] Pieter Rein Ten Wolde, David W. Oxtoby, and Daan Frenkel, "Chain formation in homogeneous gas-liquid nucleation of polar fluids", *J. Chem. Phys.* **111**, pp. 4762 (1999).

[34] M. Volmer and A. Weber, "Germ-formation in oversaturated figures", *Z. Phys. Chem.* **119**, pp. 277–301 (1926).

[35] R. Becker and W. Döring, "Kinetic treatment of germ formation in supersaturated vapour", *Ann. Phys.* **24**, pp. 719–752 (1935).

[36] Jacov I. Frenkel, *Kinetic Theory of Liquids*, Dover, New York (1959).

[37] Lev D. Landau and Eugenii D. Lifshitz, *Statistical Physics, Part 1*, Pergamon (1994).

[38] David W. Oxtoby, "Nucleation of first-order phase transitions", *Acc. Chem. Res.* **31**, pp. 91–97 (1998).

[39] G. Wulff, "On the question of speed of growth and dissolution of crystal surfaces", *ZEITSCHRIFT FUR KRYSTALLOGRAPHIE UND MINERALOGIE* **34**, pp. 449–530 (1901).

[40] David Reguera López, *Mesoscopic Nonequilibrium Kinetics of Nucleation Processes*, PhD thesis Universitat de Barcelona. (2001).

[41] Jun Wan, Y. L. Fan, D. W. Gong, S. G. Shen, and X. Q. Fan, "Surface relaxation and stress of fcc metals: Cu, ag, au, ni, pd, pt, al and pb", *Modelling Simul. Mater. Sci. Eng.* **7**, pp. 189 (1999).

[42] G. Shi, J. H. Seinfeld, and K. Okuyama, "Transient kinetics of nucleation", *Phys. Rev. A (Atomic* **41**, pp. 2101 (1990).

[43] Vitaly A. Shneidman, "Comment on "transient kinetics of nucleation"", *Phys. Rev. A (Atomic* **44**, pp. 8441 (1991).

[44] Pieter Rein Ten Wolde, Maria J. Ruiz-Montero, and Daan Frenkel, "Numerical calculation of the rate of crystal nucleation in a lennard-jones system at moderate undercooling", *J. Chem. Phys.* **104**, pp. 9932 (1996).

[45] Eduardo Mendez-Villuendas and Richard Bowles, "Surface nucleation in the freezing of gold nanoparticles", *Phys. Rev. Lett.* **98**(18), pp. 185503 (2007).

[46] Ronald Lovett, "The rate of nucleation in a vapor-liquid transition determined from hydrodynamic fluctuation theory", *J. Chem. Phys.* **81**, pp. 6191 (1984).

[47] S. H. Bauer and D. J. Frurip, "Homogeneous nucleation in metal vapors. 5. a self-consistent kinetic model", *J. Phys. Chem.* **81**(10), pp. 1015–1024 (1977).

[48] S. H. Bauer, Yi-Xue Zhang, and C. F. Wilcox, "Kinetic mechanism for condensation from supersaturated vapors that incorporate high levels of dimers", *J. Chem. Phys.* **110**, pp. 7926 (1999).

[49] Gregory K. Schenter, Shawn M. Kathmann, and Bruce C. Garrett, "Dynamical nucleation theory: A new molecular approach to vapor-liquid nucleation", *Phys. Rev. Lett.* **82**, pp. 3484 (1999).

[50] D. Reguera, "Mesoscopic nonequilibrium kinetics of nucleation processes", *J. Non-Equilib. Thermodyn.* **29**(4), pp. 327–344 (2004).

[51] John W. Cahn and John E. Hilliard, "Free energy of a nonuniform system. i. interfacial free energy", *J. Chem. Phys.* **28**, pp. 258 (1958).

[52] John W. Cahn and John E. Hilliard, "Free energy of a nonuniform system. iii. nucleation in a two-component incompressible fluid", *J. Chem. Phys.* **31**, pp. 688 (1959).

[53] R. Evans, "The nature of the liquid-vapour interface and other topics in the statistical mechanics of non-uniform, classical fluids", *Adv. Phys* **28**(2), pp. 143–200 (1979).

[54] David W. Oxtoby and R. Evans, "Nonclassical nucleation theory for the gas-liquid transition", *J. Chem. Phys.* **89**, pp. 7521 (1988).

[55] V. Talanquer and David W. Oxtoby, "Dynamical density functional theory of gas-liquid nucleation", *J. Chem. Phys.* **100**, pp. 5190 (1994).

[56] X. C. Zeng, D. W. Oxtoby, and E. Cheng, "Thermal nucleation and cavitation in helium-3 fluids", *J. Chem. Phys.* **104**, pp. 3726 (1996).

[57] V. Talanquer and David W. Oxtoby, "Nucleation in the presence of an amphiphile: A density functional approach", *J. Chem. Phys.* **106**, pp. 3673 (1997).

[58] V. Talanquer and David W. Oxtoby, "Crystal nucleation in the presence of a metastable critical point", *J. Chem. Phys.* **109**, pp. 223 (1998).

[59] J. S. Langer, "Theory of the condensation point", *Annals of Physics* **281**, pp. 941–990 (2000).

[60] H. Reiss, A. Tabazadeh, and J. Talbot, "Molecular theory of vapor phase nucleation: The physically consistent cluster", *J. Chem. Phys.* **92**(2), pp. 1266 (1990).

[61] H. Michael Ellerby, Cheryl Li Weakliem, and Howard Reiss, "Toward a molecular theory of vapor-phase nucleation. i. identification of the average embryo", *J. Chem. Phys.* **95**(12), pp. 9209 (1991).

[62] D. Reguera, R. K. Bowles, Y. Djikaev, and H. Reiss, "Phase transitions in systems small enough to be clusters", *J. Chem. Phys.* **118**(1), pp. 340 (2003).

[63] David Reguera and Howard Reiss, "Fusion of the extended modified liquid drop model for nucleation and dynamical nucleation theory", *Phys. Rev. Lett.* **93**(16), pp. 165701–165704 (2004).

[64] Cheryl Li Weakliem and Howard Reiss, "Toward a molecular theory of vapor-phase nucleation. iii. thermodynamic properties of argon clusters from monte carlo simulations and a modified liquid drop theory", *J. Chem. Phys.* **99**(7), pp. 5374 (1993).

[65] Jens Lothe and G. M. Pound, "Reconsiderations of nucleation theory", *J. Chem. Phys.* **36**, pp. 2080 (1962).

[66] Howard Reiss, Willem K. Kegel, and Joseph Katz, "Role of the model dependent translational volume scale in the classical theory of nucleation", *J. Phys. Chem. A* **102**(44), pp. 8548–8555 (1998).

[67] Howard Reiss, Willem K. Kegel, and Joseph L. Katz, "Resolution of the problems of replacement free energy, 1/s, and internal consistency in nucleation theory by consideration of the length scale for mixing entropy", *Phys. Rev. Lett.* **78**(23), pp. 4506–4509 (1997).

[68] Robert McGraw and Ari Laaksonen, "Scaling properties of the critical nucleus in classical and molecular-based theories of vapor-liquid nucleation", *Phys. Rev. Lett.* **76**(15), pp. 2754–2757 (1996).

[69] László Gránásy, "Diffuse interface approach to vapour condensation", *Europhys. Lett.* **24**, pp. 121–126 (1993).

[70] Sanjeeb K Sahoo and Vinod Labhasetwar, "Nanotech approaches to drug delivery and imaging", *Drug Delivery Today* **8**(24), pp. 1112–1120 (2003).

[71] P. Paulus, A. Goossens, R. Thiel, A. Van Der Kraan, G. Schmid, and L. De Jongh, "Surface and quantum-size effects in pt and au nanoparticles probed by 197au mössbauer spectroscopy", *Phys. Rev. B* **64**(20), pp. 205418 (2001).

[72] Umair Manzoor, Mohammad Islam, Lubna Tabassam, and Shams Ur Rahman, "Quantum confinement effect in zno nanoparticles synthesized by co-precipitate method", *Physica E: Low-dimensional Systems and Nanostructures* **41**(9), pp. 1669–1672 (2009).

[73] Armin Kleibert, Wolfgang Rosellen, Mathias Getzlaff, and Joachim Bansmann, "Structure, morphology, and magnetic properties of fe nanoparticles deposited onto single-crystalline surfaces", *Beilstein J. Nanotechnol.* **2**, pp. 47–56 (2011).

[74] K. P. Su, Z. W. Liu, D. C. Zeng, D. X. Huo, L. W. Li, and G. Q. Zhang, "Structure and size-dependent properties of ndfeb nanoparticles and textured nano-flakes prepared from nanocrystalline ribbons", *J. Phys D: Applied Physics* **46**, pp. 5003 (2013).

[75] Sihai Chen, Zhong Lin Wang, John Ballato, Stephen H. Foulger, and David L. Carroll, "Monopod, bipod, tripod, and tetrapod gold nanocrystals", *J. Am. Chem. Soc.* **125**(52), pp. 16186–7 (2003).

[76] Liu Feng, Wang Hai-Feng, Song Shao-Jie, Zhang Ke, Yang Gen-Cang, and Zhou Yao-He, "Competitions correlated with nucleation and growth in non-equilibrium solidicafcation and solid-state transformation", *Progress In Physics* **32**(2), pp. 57–96 (2012).

[77] P. R. T. Wolde and D. Frenkel, "Enhancement of protein crystal nucleation by critical density fluctuations", *Science* **277**(5334), pp. 1975–1978 (1997).

[78] G. Biroli and J. Kurchan, "Metastable states in glassy systems", *Phys. Rev. E: Stat. Nonlin. Soft Matter Phys.* **64**(1 Pt 2), pp. 016101 (2001).

[79] D. K. Kondepudi, R. J. Kaufman, and N. Singh, "Chiral symmetry breaking in sodium chlorate crystallizaton", *Science* **250**(4983), pp. 975–6 (1990).

[80] J. A. D. Wattis, "A becker–doring model of competitive nucleation", *J. Phys. A* , pp. 8755–8784 (1999).

[81] Benjamin Scheifele, Ivan Saika-Voivod, Richard K. Bowles, and Peter H. Poole, "Heterogeneous nucleation in the low-barrier regime", *Phys. Rev. E* **87**, pp. 42407 (2013).

[82] V. A. Shneidman, K. A. Jackson, and K. M. Beatty, "On the applicability of the classical nucleation theory in an ising system", *J. Chem. Phys.* **111**, pp. 6932 (1999).

[83] F. Y Wu, "The potts model", *Rev. Mod. Phys.* **54**, pp. 235 (1982).

[84] H. Arkin and T. Celik, "Study of phase conversion in three-dimensional q= 3 potts model", *Inter. J. Mod. Phys. C* **11**, pp. 1313–1320 (2000).

[85] Richard P. Sear, "Formation of a metastable phase due to the presence of impurities", *J. Phys. Condens. Matter* **17**(25), pp. 3997–4004 (2005).

[86] Christoph Dellago, Peter G. Bolhuis, and David Chandler, "Efficient transition path sampling: Application to lennard-jones cluster rearrangements", *J. Chem. Phys.* **108**, pp. 9236 (1998).

[87] Peter G. Bolhuis, Christoph Dellago, Phillip L. Geissler, and David Chandler, "Transition path sampling: throwing ropes over mountains in the dark", *J. Phys.: Condens. Matter* **12**, pp. 147 (2000).

[88] Michael Grünwald, Christoph Dellago, and Phillip L Geissler, "Precision shooting: Sampling long transition pathways", *J. Chem. Phys.* **129**(19), pp. 194101 (2008).

[89] Ravi Radhakrishnan and Bernhardt L. Trout, "Nucleation of hexagonal ice (ih) in liquid water", *J. Am. Chem. Soc.* **125**(25), pp. 7743–7 (2003).

[90] Ravi Radhakrishnan and Bernhardt L. Trout, "A new approach for studying nucleation phenomena using molecular simulations: Application to co2 hydrate clathrates", *J. Chem. Phys.* **117**, pp. 1786 (2002).

[91] Peter G. Bolhuis, "Transition-path sampling of beta-hairpin folding", *Proceedings of the National Academy of Sciences of the United States of America* **100**(21), pp. 12129–34 (2003).

[92] P. L. Geissler, C. Dellago, D. Chandler, J. Hutter, and M. Parrinello, "Autoionization in liquid water", *Science* **291**(5511), pp. 2121–2124 (2001).

[93] Michael Grünwald and Christoph Dellago, "Transition state analysis of solid-solid transformations in nanocrystals", *J. Chem. Phys.* **131**, pp. 4116 (2009).

[94] C. Dellago, P. G. Bolhuis, and P. L. Geissler, "Transition path sampling", *Adv. Chem. Phys.* **123**, pp. 1–14 (2002).

[95] Daan Frenkel and Berend Smit, *Understanding Molecular Simulation*, Academic, San Diego (2002).

[96] Gregg T. Beckham, Baron Peters, and Bernhardt L. Trout, "Evidence for a size dependent nucleation mechanism in solid state polymorph transformations", *J. Phys. Chem. B* **112**(25), pp. 7460–6 (2008).

[97] Dirk Zahn, "Atomistic mechanisms of phase separation and formation of solid solutions: model studies of nacl, nacl-naf, and na(cl1-xbrx) crystallization from the melt", *J. Phys. Chem. B* **111**(19), pp. 5249–53 (2007).

[98] Tyler J. F. Day, Udo W. Schmitt, and Gregory A. Voth, "The mechanism of hydrated proton transfer in water", *J. Am. Chem. Soc.* **122**, pp. 12027–12028 (2000).

[99] Daniel Laria, Javier Rodriguez, Christopher Dellago, and David Chandler, "Dynamical aspects of isomerization and melting transitions in [h2o]8", *Journal of Physical Chemistry A* **102**, pp. 2646–2651 (2001).

[100] Ravi Radhakrishnan and Tamar Schlick, "Orchestration of cooperative events in dna synthesis and repair mechanism unraveled by transition path sampling of dna polymerase 's closing", *Proceedings of the National Academy of Science* **101**, pp. 5970 (2004).

[101] Christoph Dellago and Peter G. Bolhuis, "Transition path sampling and other advanced simulation techniques for rare events", *Advanced Computer Simulation Approaches for Soft Matter Sciences III* , p. 167 (2009).

[102] Gideon Schwarz, "Estimating the dimension of a model", *Ann. Statist.* **6**(2), pp. 461–464 (1978).

[103] Gregg T. Beckham, Baron Peters, Cindy Starbuck, Narayan Variankaval, and Bernhardt L. Trout, "Surface-mediated nucleation in the solid-state polymorph transformation of terephthalic acid", *J. Am. Chem. Soc.* **129**(15), pp. 4714–23 (2007).

[104] R. P. Sear, "Nucleation at contact lines where fluid–fluid interfaces meet solid surfaces", *J. Phys.: Condens. Matter* **19**, pp. 033101 (2007).

[105] K. W. Mess, E. Lagendijk, D. A. Curtis, and W. J. Huiskamp, "Magnetic properties and spin-lattice relaxation of cocs3cl5 and CoCs3Br5", *Physica* **34**(1), pp. 126–148 (1967).

[106] R. F. Wielinga, H. W. J. Blöte, J. A. Roest, and W. J. Huiskamp, "Specific heat singularities of the ising antiferromagnets cocs3cl5 and cocs3br5", *Physica* **34**(2), pp. 223–240 (1967).

[107] J. C. Wright, H. W. Moos, J. H. Colwell, B. W. Mangum, and D. D. Thornton, "Dypo4: A three-dimensional ising antiferromagnet", *Phys. Rev. B* **3**, pp. 843 (1971).

[108] Nathan Duff and Baron Peters, "Nucleation in a potts lattice gas model of crystallization from solution", *J. Chem. Phys.* **131**(18), pp. 184101 (2009).

[109] J. B. Zeldovich, "On the theory of new phase formation, cavitation", *Acta Physiochimica U.S.S.R.* **18**, pp. 1 (1943).

[110] Jan Wedekind, Reinhard Strey, and David Reguera, "New method to analyze simulations of activated processes", *J. Chem. Phys.* **126**, pp. 4103 (2007).

[111] Michael R. Shirts and John D. Chodera, "Statistically optimal analysis of samples from multiple equilibrium states", *J. Chem. Phys.* **129**, pp. 4105 (2008).

[112] Seunghwa Ryu and Wei Cai, "Numerical tests of nucleation theories for the ising models", *Phys. Rev. E* **82**, pp. 11603 (2010).

[113] Rosalind J. Allen, Daan Frenkel, and Pieter Rein Ten Wolde, "Forward flux sampling-type schemes for simulating rare events: Efficiency analysis", *J. Chem. Phys.* **124**, pp. 4111 (2006).

[114] D. Reguera, J. M. Rubi, and J. M. G. Vilar, "The mesoscopic dynamics of thermodynamic systems", *J. Phys. Chem. B* **109**, pp. 21502–21515 (2005).

[115] Christoph Dellago, Peter G. Bolhuis, and David Chandler, "Efficient transition path sampling: Application to lennard-jones cluster rearrangements", *J. Chem. Phys.* **108**, pp. 9236 (1998).

[116] Michael Grünwald, Christoph Dellago, and Phillip L. Geissler, "Precision shooting: Sampling long transition pathways", *J. Chem. Phys.* **129**, pp. 4101 (2008).

[117] Jutta Rogal and Peter G. Bolhuis, "On the efficiency of biased sampling of the multiple state path ensemble", *J. Chem. Phys.* **133**, pp. 4101 (2010).

[118] Robert B. Best and Gerhard Hummer, "Reaction coordinates and rates from transition paths", *Proceedings of the National Academy of Sciences of the United States of America* **102**(19), pp. 6732–7 (2005).

[119] Rose Du, Vijay S. Pande, Alexander Yu Grosberg, Toyoichi Tanaka, and Eugene S Shakhnovich, "On the transition coordinate for protein folding", *J. Chem. Phys.* **108**, pp. 334 (1998).

[120] Gerhard Hummer, "From transition paths to transition states and rate coefficients", *J. Chem. Phys.* **120**, pp. 516 (2004).

[121] P. H. Garthwaite, I. T. Jolliffe, and B. Jones, *Statistical Inference*, Oxford, New York (2002).

[122] A. N. Patil, D. Y. Paithankar, N. Otsuka, and R. P. Andres, "The minimum-energy structure of nanometer-scale gold clusters", *Zeitschrift für Physik D Atoms* **26**, pp. 135 (1993).

[123] Charles L Cleveland, Uzi Landman, Thomas G Schaaff, Marat N Shafigullin, Peter W. Stephens, and Robert L. Whetten, "Structural evolution of smaller gold nanocrystals: The truncated decahedral motif", *Phys. Rev. Lett.* **79**, pp. 1873 (1997).

[124] F. Baletto, R. Ferrando, A. Fortunelli, F. Montalenti, and C. Mottet, "Crossover among structural motifs in transition and noble-metal clusters", *J. Chem. Phys.* **116**, pp. 3856 (2002).

[125] S. Foiles, M. Baskes, and M. Daw, "Embedded-atom-method functions for the fcc metals cu, ag, au, ni, pd, pt, and their alloys", *Phys. Rev. B: Condens Matter* **33**(12), pp. 7983–7991 (1986).

[126] Gregory Grochola, Salvy P. Russo, and Ian K. Snook, "On fitting a gold embedded atom method potential using the force matching method", *J. Chem. Phys.* **123**, pp. 4719 (2005).

[127] R. A. Johnson, "Analytic nearest-neighbor motlel for fcc metals", *Phys. Rev. B* **39**(8), pp. 1–8 (1988).

[128] F. Ercolessi, M. Parrinello, and E. Tosatti, "On fitting a gold embedded atom method potential using the force matching method", *Philosophical Magazine A-Physics of Condensed Matter Structured Defects and Mechanical Properties* **58**, pp. 213 –226 (1988).

[129] Shuichi Nosé, "A unified formulation of the constant temperature molecular dynamics methods", *J. Chem. Phys.* **81**, pp. 511 (1984).

[130] Philippe H. Hünenberger, "Thermostat algorithms for molecular dynamics simulations", *Adv. Polymer Sc.* **173**, pp. 105–149 (2005).

[131] Yanting Wang, S. Teitel, and Christoph Dellago, "Melting of icosahedral gold nanoclusters from molecular dynamics simulations", *J. Chem. Phys.* **122**(21), pp. 214722 (2005).

[132] Sarah E. M. Lundrigan and Ivan Saika-Voivod, "Test of classical nucleation theory and mean first-passage time formalism on crystallization in the lennard-jones liquid", *J. Chem. Phys.* **131**(10), pp. 104503 (2009).

[133] Andrew S. Clarke and Hannes Jonsson, "Structural changes accompanying densification of random hard-sphere packings", *Phys. Rev. E* **47**(6), pp. 3975–3984 (1993).

[134] S. Hendy and B. Hall, "Molecular-dynamics simulations of lead clusters", *Phys. Rev. B* **64**(8), pp. 085425 (2001).

[135] Helio Tsuzuki, Paulo S. Branicio, and José P. Rino, "Structural characterization of deformed crystals by analysis of common atomic neighborhood", *Comput. Phys. Comm.* **177**, pp. 518 (2007).

[136] J. Dana Honeycutt and Hans C. Andersen, "Molecular dynamics study of melting and freezing of small lennard-jones clusters", *J. Phys. Chem.* **91**, pp. 4950–4963 (1987).

[137] F. H. Stillinger and T. A. Weber, "Physreva.25.978", *Phys. Rev., A* **112**, pp. 1–12 (1982).

[138] H.-S. Nam, Nong M. Hwang, B. D. Yu, and J.-K. Yoon, "Formation of an icosahedral structure during the freezing of gold nanoclusters: Surface-induced mechanism", *Phys. Rev. Lett.* **89**, pp. –315502 (2002).

[139] Giulia Rossi and Riccardo Ferrando, "Freezing of gold nanoclusters into poly-decahedral structures", *Nanotechnology* **18**, pp. 5706 (2007).

[140] H.-S Nam, Nong M. Hwang, B. D. Yu, D.-Y. Kim, and J.-K. Yoon, "Free energy approach to the formation of an icosahedral structure during the freezing of gold nanoclusters", *Phys. Rev. B* **71**, pp. 233401 (2005).

[141] Ivan Saika-Voivod, Peter H. Poole, and Richard K. Bowles, "Test of classical nucleation theory on deeply supercooled high-pressure simulated silica", *J. Chem. Phys.* **124**(22), pp. 224709 (2006).

[142] Y. S. Djikaev, A. Tabzadeh, P. Hamill, and H. Reiss, "Thermodynamic conditions for the surface-stimulated crystallization of atmospheric droplets", *J. Phys. Chem. A* **106**(43), pp. 10247–10253 (2002).

[143] Eduardo Mendez-Villuendas, "Nucleation in gold nanoclusters", Master's thesis University of Saskatchewan (2007).

[144] Caroline Desgranges and Jerome Delhommelle, "Molecular simulation of cross-nucleation between polymorphs", *J. Phys. Chem. B* **111**(6), pp. 1465–9 (2007).

[145] Federica Trudu, Davide Donadio, and Michele Parrinello, "Freezing of a lennard-jones fluid: From nucleation to spinodal regime", *Phys. Rev. Lett.* **97**, pp. 105701 (2006).

[146] John Russo and Hajime Tanaka, "The microscopic pathway to crystallization in supercooled liquids", *Nature Scientific Reports* **2**, pp. 505 (2012).

[147] Swetlana Jungblut, Andreas Singraber, and Christoph Dellago, "Optimising reaction coordinates for crystallisation by tuning the crystallinity definition", *Mol. Phys.* **111**, pp. 3527 (2013).

[148] Aaron S. Keys, Christopher R. Iacovella, and Sharon C. Glotzer, "Characterizing complex particle morphologies through shape matching: Descriptors, applications, and algorithms", *J. Comput. Phys.* **230**, pp. 6438 (2011).

[149] Eduardo Mendez-Villuendas and Richard K. Bowles, "Surface nucleation in the freezing of gold nanoparticles", *Phys. Rev. Lett.* **98**, pp. 185503 (2007).

[150] A. Tabazadeh, Y. S. Djikaev, P. Hamill, and H Reiss, "Laboratory evidence for surface nucleation of solid polar stratospheric cloud particles", *J. Phys. Chem. A* **106**(43), pp. 10238–10246 (2002).

[151] Y. S. Djikaev, A. Tabazadeh, P. Hamill, and H. Reiss, "Thermodynamic conditions for the surface-stimulated crystallization of atmospheric droplets", *J. Phys. Chem. A* **106**(43), pp. 10247–10253 (2002).